Atmospheric electric fields during thunderstorm conditions measured by LOFAR

Trinh, Thi Ngoc Gia

university of groningen

kvi - center for advanced radiation technology

NWO

Netherlands Organisation for Scientific Research

This work is part of the research programme of the Foundation for Fundamental Research on Matter (FOM), which is part of the Netherlands Organisation for Scientific Research (NWO).

ISBN (printed version): 978-94-034-0815-6
ISBN (electronic version): 978-94-034-0816-3
Cover: An air shower develops through a thundercloud and reaches the LOFAR 'Superterp'. Pictures are taken from Ref. [1] and Ref. [2].

university of groningen

Atmospheric electric fields during thunderstorm conditions measured by LOFAR

PhD thesis

to obtain the degree of PhD at the
University of Groningen
on the authority of the
Rector Magnificus Prof. E. Sterken
and in accordance with
the decision by the College of Deans.

This thesis will be defended in public on

Monday 9 July 2018 at 11.00 hours

by

Thi Ngoc Gia Trinh

born on April 30, 1986
in An Giang, Vietnam

Supervisors

Prof. O. Scholten

Prof. A. M. van den Berg

Prof. U. Ebert

Assessment committee

Prof. J. Dwyer

Prof. T. Huege

Prof. N. Kalantar-Nayestanaki

Table of contents

Chapter 1

Introduction

1.1 Cosmic rays

In the early 1900's, when radioactivity was first discovered by Henri Becquerel, Pierre Curie and Marie Curie [3], it was believed that the ionizing radiation measured in the atmosphere was produced by γ-rays emitted by nuclear processes on the ground. Thus, the ionization level should decrease with increasing altitudes. In 1912, Victor Hess took a balloon flight up to 5 km to measure the amount of ionization as a function of height [4]. He found that at heights above 1.1 km, the ionization level increases with altitude, which meant the radiation had to be coming from outer space. His experiment marked the discovery of cosmic rays and he received a Nobel prize in 1936.

Cosmic rays have an enormous energy range, starting at about 10^7 eV and reaching about 10^{20} eV and they come from different sources. The cosmic rays with energies less than 10^{10} eV are predominantly solar cosmic rays produced in solar flares. The cosmic-ray energy spectrum for higher energies, from 10^{10} eV to about 10^{20} eV is shown in Fig. 1.1. The spectrum follows a power law, scaling approximately as E^{-3}, which shows that the flux of cosmic rays drops dramatically when going to higher energies.

The cosmic-ray spectrum has some interesting features. The first feature in the spectrum is the knee observed at an energy of $5 \cdot 10^6$ GeV where the index of the power law changes from 2.7 to 3.1. The origin of the knee is still being discussed in

the literature [5]. A possible explanation is the leakage of particles from the galaxy. Particles at these energies are not bound by the magnetic fields of the galaxy and thus start to leave the galaxy. There is a second knee-like structure at an energy of $4 \cdot 10^8$ GeV which can be explained by heavy elements leaving the acceleration region or the galaxy. The ankle-like structure at $4 \cdot 10^9$ GeV is thought to be the signature for the transition between galactic and extragalactic cosmic rays [6, 7].

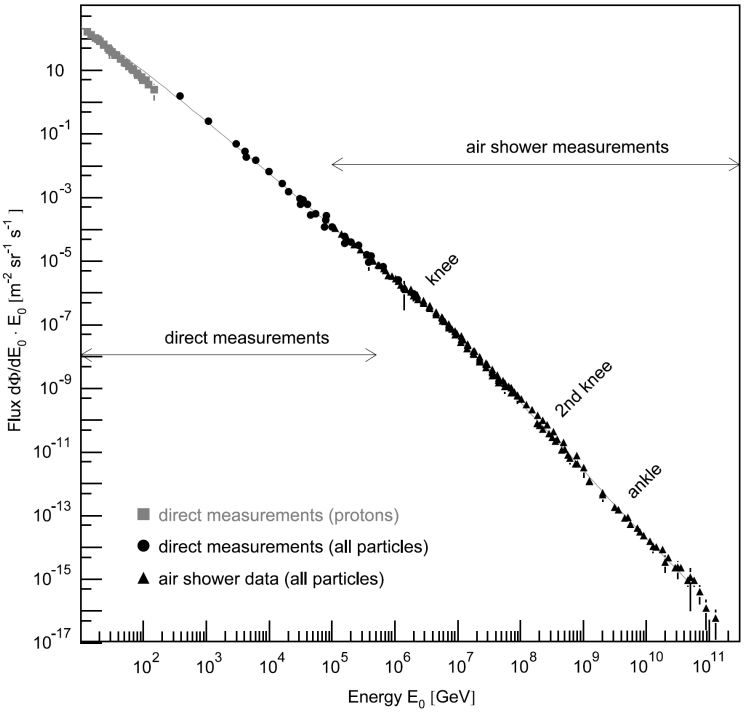

Fig. 1.1 The differential flux of cosmic rays as a function of the primary energy of the cosmic ray. Adapted from Ref. [8].

1.2 Extensive air showers

When a cosmic ray enters the atmosphere, it will interact with an air molecule and generate a particle cascade which is called an extensive air shower [9]. There are two types of air showers: hadron showers and electromagnetic cascades.

As shown in Fig. 1.2, an air shower has three components: an electromagnetic, a hadronic and a muonic component. If the cosmic ray is a proton or a (heavy) nucleus, a hadronic shower is generated. The secondary particles produced are mostly pions. The number of generated kaons is about 10% of the number of pions. Neutral pions decay very quickly into two photons

$$\pi^0 \to \gamma + \gamma. \tag{1.1}$$

The photons create pairs of electrons and positrons

$$\gamma \to e^+ + e^- . \tag{1.2}$$

Subsequently, these leptons undergo bremsstrahlung, producing more photons. These photons then create more leptons through pair production and ionization. They are the electromagnetic component of the shower. Charged pions and kaons can initiate

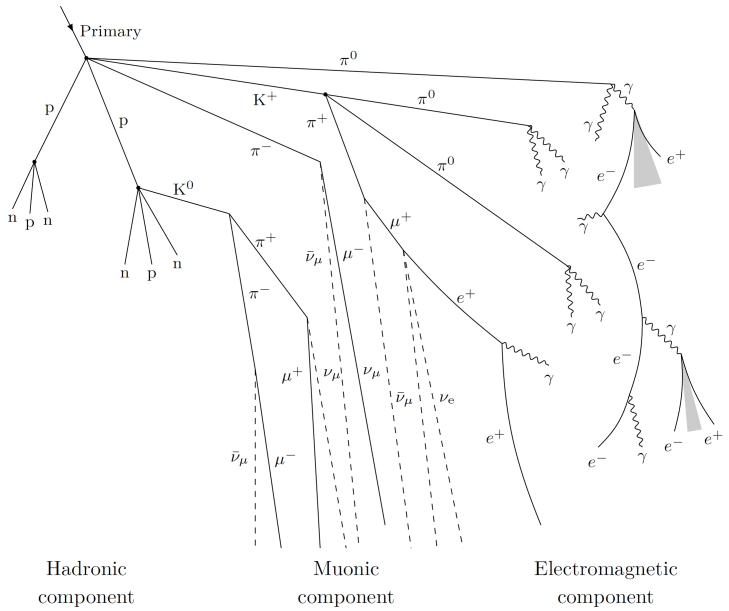

Fig. 1.2 Three components of an extensive air shower: a hadronic, a muonic and an electromagnetic component. Taken from Ref. [10].

further interactions or decays depending on their energies. The decay timescale for these particles is larger than the typical time between encounters and thus the particles may interact and contribute to the hadronic component of the shower before they can decay. When the energy decreases, leptonic decays of pions and kaons can take over, producing muons and neutrinos which form the muonic component of the shower

$$\begin{aligned} \pi^+ &\to \mu^+ + \nu_\mu \\ \pi^- &\to \mu^- + \bar{\nu}_\mu \\ K^+ &\to \mu^+ + \nu_\mu \\ K^- &\to \mu^- + \bar{\nu}_\mu \end{aligned} \tag{1.3}$$

Since the interaction length of the muons and neutrinos are much longer than the typical distance to the observer, they have a large chance to reach the ground. Otherwise, they decay through

$$\begin{aligned} \mu^+ &\to e^+ + \nu_e + \bar{\nu}_\mu \,, \\ \mu^- &\to e^- + \bar{\nu}_e + \nu_\mu \,. \end{aligned} \tag{1.4}$$

If the cosmic ray is a lepton or a photon, only the electromagnetic component develops.

The number of secondary particles in air showers grows roughly exponentially as a function of penetration depth, reaching a maximum at the depth called $X_{\max}$ and diminishing after that. The total number of charged particles at $X_{\max}$ is roughly equal to $E/(1\ \mathrm{GeV})$ where E is the energy of the shower in eV. Fig. 1.3 shows the shower profiles of an iron shower and a proton shower simulated by CORSIKA [11], a Monte Carlo code to simulate extensive air showers. As shown in this figure, iron showers have generally smaller $X_{\max}$, i.e. higher up in the atmosphere, than proton showers. This is due to the fact that the cross section of iron nuclei is large and thus the iron nuclei interact with molecules earlier and higher in the atmosphere. Primary particles with the same energy, mass and direction can generate different air showers. This feature which is called shower-to-shower fluctuations is caused by random fluctuations in the depth, multiplicity and inelasticity of the first interaction and of the secondary interactions [12]. Since most of the shower particles travel with very high velocities, almost the velocity of light, they are concentrated in the relatively thin shower front, which is called the ‘pancake’. The pancake contains extremely large

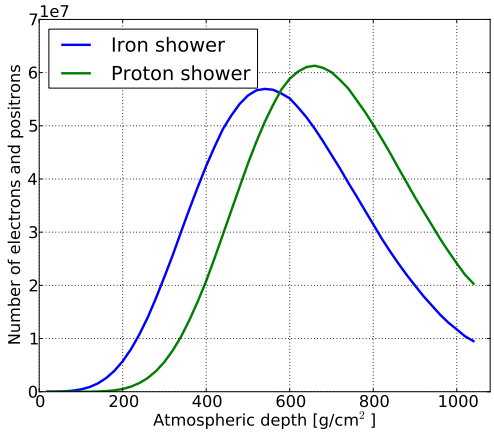

Fig. 1.3 Number of electrons and positrons as a function of atmospheric depth for 10^{17} eV vertical showers simulated by CORSIKA. The atmospheric depth is the integral of density of the overlying air. For a vertical shower, the sea level is at 1028 g/cm^2. $X_{\max}$ = 545 g/cm^2 for this iron shower and 670 g/cm^2 for this proton shower.

numbers of electrons and positrons. The thickness of the pancake is few millimeters near the shower axis and up to a few hundred meters at the edges [13].

1.3 Radio emission from air showers in fair weather

For the first time, radio pulses from extensive air showers were measured by Jelley et al. [14]. Thereafter, many measurements over a wide frequency range were performed [15, 16]. However, due to technical difficulties, the detection of radio emission from air showers was not continued. Later, in the early 21st century, it was developed again. Measurements at LOPES [17, 18] and CODALEMA [19, 20] gave many interesting results. The current generation of detection systems such as Tunka-Rex [21], AERA [22], and LOFAR [23] have also given large contributions to the knowledge of air-shower radio emission.

At the same time, there were many attempts to model radio emission from air showers. The first model was developed by Askaryan in 1962 [24]. He predicted that there is a net negative charge excess in the shower front since electrons are

knocked out of atmospheric molecules. These electrons have enough energy to travel along the shower front. This negative charge excess gives rise to coherent radio emission. In 1966, Kahn and Lerche built a macroscopic model based on the induced transverse current in the shower front [25]. Due to the geomagnetic field, electrons and positrons are accelerated along the direction of the Lorentz force. They form a transverse current pointing in the direction of the Lorentz force which also emits radiation. For this reason, the amplitude of the radio signal depends on the angle α between the shower axis and the geomagnetic field **B**.

The main difference between the two contributions is the polarization direction of the signals. For the geomagnetic component, since the induced current points in the direction of the Lorentz force, the radiation is linearly polarized along the same direction. Charge-excess radiation is also linearly polarized but is polarized in the radial direction with respect to the shower axis.

On the surface of the Earth, the superposition of both components is observed. Since their polarization directions are different, the intensity pattern observed is complicated. Furthermore, this is influenced by Cherenkov effects. Since the emission is propagating in air where the index of refraction is not unity but has a value of about 1.0003 at sea level and decreases with altitude, the emission emitted at different times and locations can reach a given observer at the same time. This creates relative time compression effects that result in Cherenkov rings seen in the intensity pattern on the ground in the GHz frequency range [26–28].

In the last ten years, several new models, which can be separated into two categories, microscopic and macroscopic, have been developed. The microscopic models such as CoREAS [29], ZHAireS [30] follow individual shower particles and calculate their radio emission. The macroscopic models such as MGMR [31], EVA [32], MGMR3D [33] calculate the radio emission from the currents and charge densitites in the shower plasma cloud. The microscopic and macroscopic models agree in the description of radio emission features [34].

1.4 LOFAR, LORA and data analysis

1.4.1 LOFAR - The Low Frequency Array

LOFAR is a distributed radio telescope used to observe the radio frequencies from 10 MHz to 240 MHz. The antennas of LOFAR are distributed over several European countries with a core in the Netherlands. They are group into stations. There are 24 stations distributed within the $\sim$ 2 km wide core and 16 additional Dutch remote stations placed with increasing distance from the core. International stations are located in Germany, France, the United Kingdom and Sweden. Core and remote stations consist of 96 low-band antennas (LBAs, $10-90$ MHz) and 48 high-band antennas (HBAs, $110-240$ MHz) while international stations have 96 LBAs and 96 HBAs. In the center of LOFAR core, there are six stations located in a roughly 320 m diameter area, which is called the 'Superterp' (see Fig. 1.4). The cosmic-ray data are taken with the central 24 stations where data from particle detectors (see Sec. 1.6) are also available. The LBAs are the main tool to detect cosmic rays. An LBA consists of two orthogonal inverted V-shaped dipoles. Each dipole has a length of 1.38 m. The dipoles X and Y are oriented southwest to northeast (SW-NE) and southeast to northwest (SE-NW). A HBA element consists of dual-polarization fat dipole

Fig. 1.4 The 'Superterp' of LOFAR. The picture is taken from Ref. [2]

antennas in which holes were cut to save material. In order to minimize maintaining

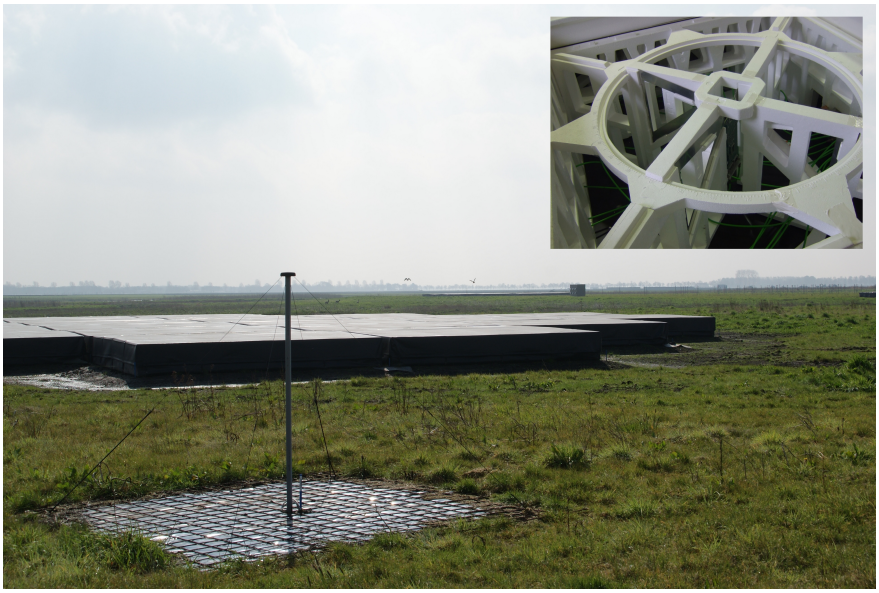

Fig. 1.5 LOFAR antennas at the center core. A LBA is shown in the foreground. Behind the LBA is a cluster of 24 black tiles of HBAs. The inset displays the construction of a HBA in which the bow-tie shaped antennas are mounted before they are covered by weather-proof foil. The picture is taken from Ref. [35].

cost, 16 HBA elements are arranged in a plastic structure called tile. Each tile is packed in black foil to protect the antenna electronics from rain.

1.4.2 LORA - The LOFAR Radbound Air Shower Array

LORA is an array of 20 particle detectors which are distributed on the 'Superterp'. Each detector which is 125 cm$\times$98 cm in size consists of two scintillators and is installed inside a weatherproof box. LORA provides a reconstruction of basic air shower parameters such as the arrival time of the shower, the direction and position of the shower axis, the lateral density distribution of the charged particle. In addition, it can help to estimate the primary energy of the shower.

The arrival time is used to trigger the read-out of the radio antennas. A trigger in a LORA detector is generated when a particle signal of more than 4σ above the noise is registered. In order to only measure air showers, several detectors need to

trigger at the same time. As shown in the right panel of Fig. 1.6, requiring triggers in 12 particles detectors yields a energy threshold of about $2 \cdot 10^{16}$ eV and an average trigger-rate of 1.25 events/hour. This trigger rate has been used for the observations.

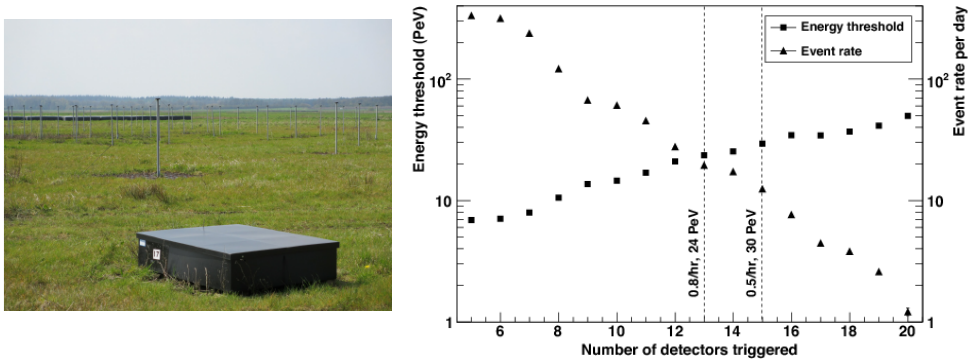

Fig. 1.6 Left: a particle detector. Right: Energy threshold and the event rate per day as a function of the number of particle detectors which have registerd at least one particle. Taken from Ref. [36].

1.4.3 Data analysis

The data used in this thesis is from LBAs. Electromagnetic pulses are sampled every 5 ns and stored for 5 s on ring buffers for each LBA. The data were processed in an off-line analysis. An initial estimate for the arrival direction of the air shower is given by the LORA data. The measured radio signal is Fourier transformed to the frequency domain. Since below 30 MHz and above 80 MHz, radio frequency interference is strong, the data is filtered in the $30 - 80$ MHz range. For each antenna polarization, the signals are first beamformed in this arrival direction. Therefore, the signal-to-noise ratio for a cosmic-ray signal from this direction increases by a factor of about seven [37]. If no significant signal is detected in the beamformed trace, the analysis of the data at that station is aborted. The next step is to reconstruct the arrival direction of the air shower from a plane wave fit to the arrival times of the pulse maxima. Air showers which have four or more stations having a successful reconstruction are included. From the measured voltages, the radiation fields S are calculated by inverting the antenna calibration. The complex radiation fields

$\varepsilon_k = S_k + i\hat{S}_k$ are derived where $\hat{S}_k$ is sample k of the Hilbert transform of S. For each antenna, the real-valued Stokes parameters which expressed as

$$\begin{aligned} I &= \frac{1}{n}\sum_{i=0}^{n-1}\left(\left|\varepsilon_{i,\mathbf{v}\times\mathbf{B}}\right|^2 + \left|\varepsilon_{i,\mathbf{v}\times(\mathbf{v}\times\mathbf{B})}\right|^2\right), \\ Q &= \frac{1}{n}\sum_{i=0}^{n-1}\left(\left|\varepsilon_{i,\mathbf{v}\times\mathbf{B}}\right|^2 - \left|\varepsilon_{i,\mathbf{v}\times(\mathbf{v}\times\mathbf{B})}\right|^2\right), \\ U + iV &= \frac{2}{n}\sum_{i=0}^{n-1}\left(\varepsilon_{i,\mathbf{v}\times\mathbf{B}}\varepsilon^*_{i,\mathbf{v}\times(\mathbf{v}\times\mathbf{B})}\right), \end{aligned} \tag{1.5}$$

are calculated. The summation is perform over n = 11 samples around the peak of the pulse. Stokes I is the intensity of the radio emission. Stokes Q and U are used to derive the linear polarization angle

$$\psi = \frac{1}{2}\tan^{-1}\left(\frac{U}{Q}\right), \tag{1.6}$$

and V/I represents the amount of circular polarization. An event becomes a possible thunderstorm event if its linear polarization is very different from a normal event.

1.5 Thunderstorm charge structure and cloud electrification

1.5.1 Thunderstorm charge structure

The basic charge structure of thunderclouds contains three charge layers: a main positive on top, a main negative and a lower positive charge layer [38] as shown in Fig. 1.7. In addition, there is often an upper screening negative layer generated by the higher conductivity of the air outside the cloud. The main negative charge layer contains both ice and super-cooled water in a temperature range between -10 and -25°C [38, 39]. It is found at different altitudes in different places and seasons. In summer thunderstorms in Florida and New Mexico, the main negative charge layers are found between 6 km and 8 km above sea level, while in winter thunderstorms in Japan, it is at 2 km [40]. The main positive charge layer often spreads more in altitude

than the negative one [41]. It can range between about 8 km to 15 km in the summer and a few kilometers in altitude in the winter. The lower positive layer is located at the bottom of the clouds and lies above 2 km for summer thunderstorms in Florida. This layer may not always be present [38, 42]. In contrast, some inverted charge structures, i.e. lower main positive layer and upper negative layer, are sometimes found in thunderstorms [43].

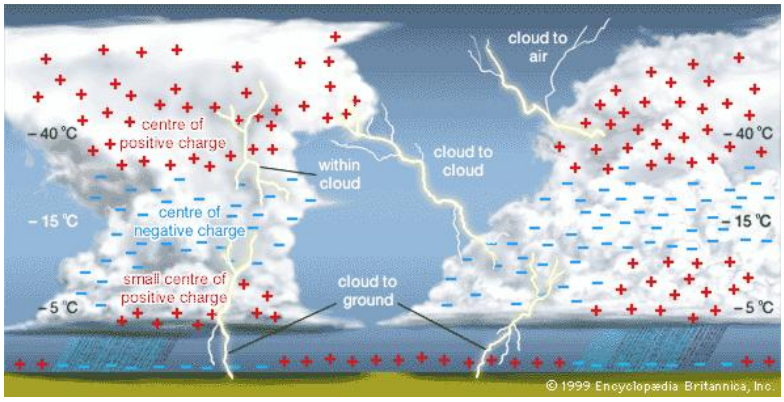

Fig. 1.7 The simple charge structure of thunderclouds and some locations where the lightning can occur. Adapted from Ref. [44]

The charge structures keep changing over the lifetime of the storm, so the charge structures and electric fields inside thunderclouds are complicated, depending on time and place. As a result, it is difficult to have a complete mapping of electric fields which is necessary in understanding lightning initiation and propagation.

1.5.2 Cloud electrification

Although charge transfer in thunderclouds happens very often, the mechanism of charge transfer is not well understood. There are many mechanisms of thundercloud electrification. Two of them, the convection mechanism and the non-inductive mechanism will be discussed in more detail in this section.

The convection mechanism [45, 46] was introduced in the 1950s. As illustrated in Fig. 1.8, there is an updraft of the positive charge found in the air above the ground during fair weather going to the top of thunderclouds and form the positive charge region. Negative charges, produced by cosmic rays above the cloud, are attracted to

the boundary of the cloud by the positive charges and form a negative screening layer. Downdrafts, caused by convections, are assumed to carry the negative charges down to the middle center of the cloud to form the main negative charge region. This region generates additional positive charges under the cloud and thus provides a positive feedback to the whole process. Although cloud edge motions can clearly have an effect on the distribution of charge inside a thunderstorm, the convective mechanism cannot fully explain cloud electrification because negative charge regions formed by this theory would unlikely lie in a similar temperature range for different types of thunderstorms. Therefore, this initial theory is not accepted anymore.

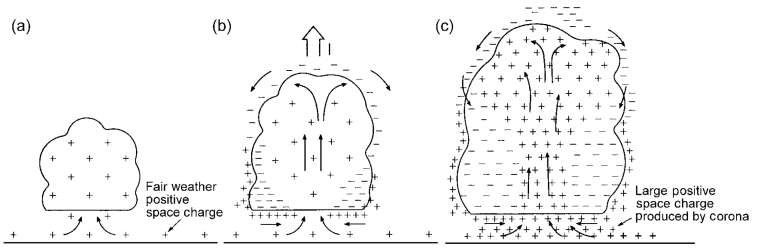

Fig. 1.8 Illustration of the convection mechanism of cloud electrification. Adapted from Ref. [47]

In the non-inductive mechanism, the electric charges are produced by collisions between graupel and small ice crystals in the presence of water droplets which is necessary for significant charge transfer [48–50]. A simplified illustration of this mechanism is shown in Fig. 1.9. The heavy grauple particles fall through a suspended region of ice crystals and supercooled water droplets. It has been shown in laboratory experiments that when the temperature is below a so-called reversal temperature, T_R, the graupel particles get a negative charge in collisions with the ice crystals. Due to the different sizes and fall velocities of the graupel particles and the ice crystals, they tend to separate after the collisions. The negatively charged graupel particles tend to accumulate in the middle of the cloud and the ice crystals are carried up to higher parts of the cloud. In contrast, at low altitudes where the temperature is higher than T_R, the graupel particles get a positive charge and thus the polarities reverse. The reversal temperature, T_R, is thought to be between $-10°$C and $-20°$C which is the temperature range of the main negative charge region. The positively charged graupel

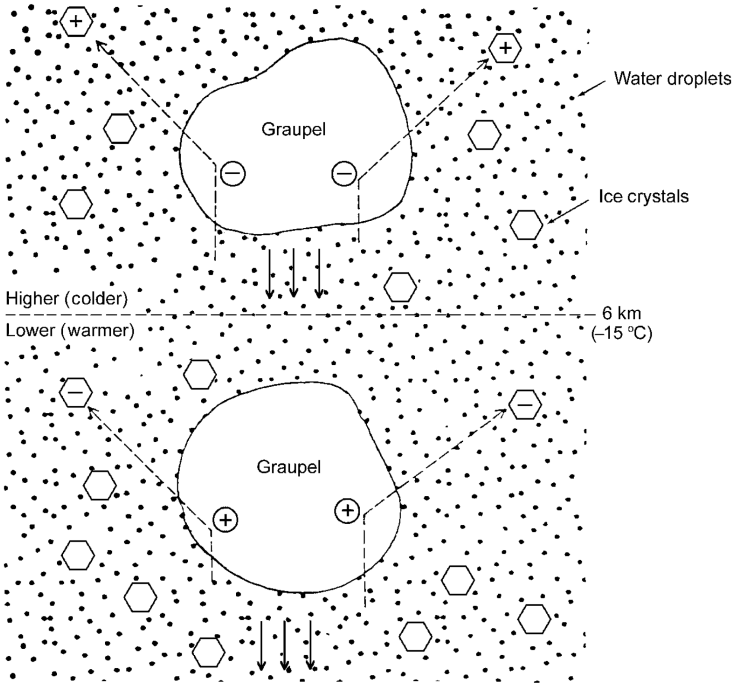

Fig. 1.9 Illustration of the non-inductive mechanism of cloud electrification. Adapted from Ref. [38]. The reversal temperature T_R is assumed to be $-15°$C and to occur at an altitude of 6 km.

particles below the height of T_R are considered to be the source of the lower positive charge region [51]. The relative humidity also affects the charging process. The charging rate and sign depend very strongly on the relative humidity. The greater the relative humidity is, the larger is the magnitude of negative charge transfer [52]. The larger relative humidity also shifts the reversal temperature T_R to higher temperatures. This mechanism is capable to explain the triple cloud charge structure discussed in Section 1.4.1.

1.6 This thesis

Thunderstorm electric fields play an important role in understanding how lightning initiates and propagates but they are difficult to measure. A conventional method to

measure them is launching a balloon-borne electric field meter or a rocket [53, 54] into thunderclouds. However, this method is affected by violent winds and it also disturbs the electric fields in the clouds. In this thesis, we introduce and develop a new technique to probe thunderstorm electric fields non-intrusively. This method is based on the fact that during thunderstorms, strong electric fields cause significant changes in the distribution of charged particles in the shower front and the radio emission patterns of the shower. At the Low Frequency Array (LOFAR), we observe large differences between radio patterns of showers measured under fair weather (fair-weather events) and showers measured under thunderstorm conditions (thunderstorm events). These differences in turn can be used to probe the thunderstorm electric fields. Unlike balloon measurements, this method is independent of winds and the measurement process does not disrupt the field to be measured.

1.6.1 Radio emission from air showers in thunderstorm conditions

During thunderstorm conditions, beside the Lorentz force caused by the geomagnetic field, the atmospheric electric field exerts an electric force which is much stronger than the Lorentz force. The electric field can be decomposed into two components, the component parallel to the shower axis, $E_{\parallel}$, and the component perpendicular to the shower axis, $E_{\perp}$. These two components affect the charged-particle distribution in the shower front in different ways. $E_{\perp}$ accelerates charged particles into the transverse direction and thus increases the transverse current although the total number of charged particles hardly increases. It also changes the direction of the transverse current at the shower front since this electric field, in general, points in a direction different to the Lorentz force. $E_{\parallel}$ can accelerate electrons or positrons in the shower depending on the polarity of the field, depositing the energy and thus their number increases. In this work we consider field strengths up to about 100 kV/m which is below the runaway breakdown limit of 284 kV/m at sea level [55, 56]. Above the runaway breakdown threshold, fast electrons are accelerated by the electric field and they could become runaway electrons. Due to interaction with air, they will produce energetic electrons that can also runaway. The result is an avalanche of relativistic electrons increasing exponentially with distance and time. The radio emission produced by the relativistic runaway electron avalanches can also be used to

determine remotely electrostatic fields [57]. However, this radiation can be observed at the frequency range lower than the frequency of LOFAR low band antennas.

Since $E_\perp$ and $E_\parallel$ change the charged-particle distribution in the shower front differently, the changes seen in the radio pattern of the shower caused by these two electric field components are rather different. With the LOFAR low band antennas, having the frequency range from 30 MHz to 80 MHz, we can observe the influence caused by the perpendicular component. $E_\perp$ not only increases the intensity but also modifies the intensity and polarization patterns. For small values of $E_\perp$, the intensity is proportional to the square of the magnitude of the current. However, when $E_\perp$ is larger than about 50 kV/m, the intensity of the radio emission starts to saturate. Since particles move relativistically and their total velocity cannot exceed the light velocity, an increased transverse velocity will result in a decrease of the longitudinal velocity. Therefore, for strong perpendicular electric fields, the particles will trail further behind the shower front and their radiation does not contribute coherently in the LOFAR frequency band any more and thus the radio intensity is almost constant. Surprisingly, within the LOFAR frequency range, we are not sensitive to the parallel electric field component. The reason for this is that the additional charged particles generated by strong parallel electric fields trail much further behind the shower front. Therefore, their radio emission does not contribute coherently in the frequency range of the LOFAR low band antennas ($30-80$ MHz). In order to increase the sensitivity of the parallel electric field component, one needs to go to the lower frequency range of $2-9$ MHz. These effects are discussed in more detail in Chapter 2. A simplified model based on electron dynamics in air showers is also presented in this chapter for explanation.

Not only the intensity and the linear polarization, but also the circular polarization shows large differences between fair-weather events and thunderstorm events. In the fair-weather events, the circular polarization is caused by a small time shift, about 1 ns, between the radiation from charge-excess and transverse current components [58]. Therefore, it depends on the azimuthal positions of the antennas and it is small near the shower axis. In contrast, the circular polarization in thunderstorm events can be large near the shower axis and it may not depend on the azimuthal position of the observer. Since the electric fields during thunderstorm conditions change in strength and direction with altitude, the transverse current also changes its magnitude and

direction. As a result, the radio signals at different altitudes are linearly polarized but not in the same orientation. They arrive at antennas on the ground with a small time shift, so the linear polarization of the total signal at the antennas changes in time, which gives rise to circular polarization. In Chapter 4, the differences in circular polarization between fair-weather events and thunderstorm events will be discussed in more detail. A simple model to explain the cause of circular polarization in thunderstorm events is also presented in this chapter.

1.6.2 Measurements at LOFAR and the method to probe electric fields during thunderstorm conditions

At LOFAR, we have measured the effects of thunderstorm electric fields on radio patterns from air showers. We see many significant differences between thunderstorm events and fair-weather events as mentioned above. A first and clearly distinguished feature of a thunderstorm event is the polarization pattern. In fair-weather events, radio signals over all antennas are polarized mainly along the Lorentz force, while in thunderstorm events, as discussed above, the signals are often not polarized along this direction anymore. We observe that, in some thunderstorm events, the polarization direction is oriented in a direction completely different from the Lorentz force since the perpendicular electric field component changes the direction of the transverse current. We also observe 'wavy' polarization patterns where the linear polarizations at small and large distances from the shower axis are different. This is caused by the rotation of the electric fields and thus the current as a function of altitude.

Moreover, we observe large differences in the intensity pattern between fair-weather events and thunderstorm events. In fair-weather events, the intensity pattern shows a bean-shape structure due to the interference of transverse-current and charge-excess components at different locations around the shower axis. In thunderstorm events, however, a typical intensity pattern often observed is a ring-like structure. We also measure thunderstorm events showing an intensity pattern which is similar to that of fair-weather events. These events are distinguished from fair-weather events by the polarization patterns.

As discussed above, both fair-weather and thunderstorm events have some amount of circular polarization. Although the amount of circular polarization in fair-weather

events is rather small, we are able to measure it at LOFAR. In addition, we have shown that the measured circular polarization in the fair-weather events is in good agreement with both microscopic and macroscopic models [58]. In many thunderstorm events, we observe a large amount of circular polarization near the shower axis which is not seen in fair-weather events. We also see that the circular polarization in thunderstorm events does not depend on the azimuthal position of the observers as it does in fair-weather events. The fact that we have a good understanding of the circular polarization in fair-weather events and the fact that the circular polarization measured in thunderstorm events is very different from fair-weather events shows that the circular polarization can be used to get additional information on the electric fields.

As a first step, we start to build the technique to determine atmospheric electric fields during thunderstorm conditions by only fitting the intensity pattern. We find that the electric fields need to have at least two layers in order to reconstruct the ring-like structure in the intensity pattern. In this model, the perpendicular electric fields in these two layers are such that the net forces in these layers are opposite to each other and the force in one layer points in the direction of the linear polarization. Since LOFAR is not sensitive to the parallel electric field as mentioned before, this field is set to zero in our analysis. This structure of the electric field introduces a destructive interference between the radio emission from two layers which gives rise to the ring-like structure in the intensity pattern. We also found that the diameter of the ring is strongly correlated to the height where the electric field changes but it does not depend much on X_{max}. The ring is relatively large when the electric field changes at high altitude. For this reason, this altitude is very well defined by our analysis. However, we are, unfortunately, not sensitive to the height above 8 km. The first stage of the method will be discussed in detail in Chapter 3. Later, we realized that the polarization signature gives additional information about the electric fields. Therefore, as a second step, we developed a technique to fit both the intensity and polarization patterns. We find that the large amount of circular polarization measured near the shower axis in thunderstorm events cannot be reproduced by a two-layered electric field since there is no rotation of the transverse current. In order to obtain a good fit for both the intensity and the polarization patterns, we need to expand the two-layered model of the electric field to a three-layered model. A detailed discussion about the second stage of the method can be seen in Chapter 4.

1.6.3 Full analysis

During the period between December 2011 and September 2014, we recorded 31 thunderstorm events. We selected 11 thunderstorm events which pass the criterion of the quality of radio and particle data. We use the technique developed to analyze these events in order to extract the perpendicular electric fields along the shower axis. Since the thunderstorm events came from different directions and at different times, we can determine the electric fields at different places and time. In 11 thunderstorm events analyzed, there are two groups where each group has three events recorded within an hour. The showers in each group probably passed through the same thundercloud. These events can be used for a type of tomography for the thundercloud electric field.

We find some interesting features of charge structure in thunderclouds overhead of LOFAR which can be seen from the electric fields probed by these thunderstorm events. In the selected 11 thunderstorm events, there are events that seem to have typically three charged regions: upper positive, main negative, and lower positive while some events only have a two-layered structure. Moreover, the events show a strong seasonal dependence of the lowest charged region which is likely due to the temperature difference between winter and summer. We also see that in most of these events, the lower positive charged regions occur near the 0° C isotherm which is similar to what is observed for summer thunderstorms in Florida. However, three winter events show that the lower positive charge region is 1 km in altitude lower than the 0° C isotherm. There are three possibilities to explain this. It could be that there are charged regions at the freezing height but we are not sensitive to those. Or it could be that the charge mechanism in these winter thunderstorms is very different from that in the summer thunderstorms. Another possibility is that these events have an inverted-polarity structure: upper negative, main positive and lower negative charge regions. In addition, large horizontal electric fields have been measured. In general, the horizontal field is small at the bottom layer and large in the middle and the top layers. The full analysis of thunderstorm events and the features of charge structure found by our analysis will be discussed more in Chapter 5. The final chapter, Chapter 6, will give the outlook.

Chapter 2

Influence of atmospheric electric fields on the radio emission from extensive air showers

T.N.G. Trinh, O. Scholten, et al.
Physical Review D 93, 023003 (2016)

Abstract

The atmospheric electric fields in thunderclouds have been shown to significantly modify the intensity and polarization patterns of the radio footprint of cosmic-ray-induced extensive air showers. Simulations indicated a very nonlinear dependence of the signal strength in the frequency window of $30-80$ MHz on the magnitude of the atmospheric electric field. In this work we present an explanation of this dependence based on Monte Carlo simulations, supported by arguments based on electron dynamics in air showers and expressed in terms of a simplified model. We show that by extending the frequency window to lower frequencies additional sensitivity to the atmospheric electric field is obtained.

2.1 Introduction

When a high-energy cosmic ray particle enters the upper layer of the atmosphere, it generates many secondary high-energy particles and forms a cosmic-ray-induced air shower. Since these particles move with velocities near the speed of light, they are concentrated in the thin shower front extending over a lateral distance of the order of 100 m, called the pancake. In this pancake the electrons and positrons form a plasma in which electric currents are induced. These induced currents emit electromagnetic radiation that is strong and coherent at radio-wave frequencies due to the length scales that are relevant for this process [59]. Recent observations of radio-wave emission from cosmic-ray-induced extensive air showers [17, 20, 60, 61, 37, 35, 62] have shown that under fair-weather conditions there is a very good understanding of the emission mechanisms [63]. It is understood that there are two mechanisms for radio emission that determine most of the observed features. The most important contribution is due to an electric current, that is induced by the action of the Lorentz force when electrons and positrons move through the magnetic field of the Earth [25, 31]. The Lorentz force induces a transverse drift of the electrons and positrons in opposite directions such that they contribute coherently to a net transverse electric current in the direction of the Lorentz force $\mathbf{v} \times \mathbf{B}$ where $\mathbf{v}$ is the propagation velocity vector of the shower and $\mathbf{B}$ is the Earth's magnetic field. The radiation generated by the transverse current is polarized linearly in the direction of the induced current. A secondary contribution results from the build up of a negative charge excess in the shower front. This charge excess is due to the knock-out of electrons from air molecules by the shower particles, and gives rise to radio emission that is polarized in the radial direction to the shower axis [24, 64]. The total emission observed at ground level is the coherent sum of both components. Because the two components are polarized in different directions, they are added constructively or destructively depending on the positions of the observer relative to the shower axis. Since the particles move with relativistic velocities the emitted radio signal in air, a dielectric medium having a nonunity refractive index, is subject to relativistic time-compression effects. The radio pulse is therefore enhanced at the Cherenkov angle [27, 35]. Another consequence of the relativistic velocities is that the emission is strongly beamed and the radio emission is only visible in the footprint underneath

the shower, limited to an area with a diameter of about 600 meters. As is well understood [31], under fair-weather circumstances we see that the signal amplitude is proportional to the energy of the cosmic ray and thus to the number of electrons and positrons in the extensive air shower [61]. We note that this proportionality of the radio emission to the number of electrons and positrons no longer holds in the presence of strong atmospheric electric fields which is the main subject of this work. The frequency content of the pulse is solely dependent on the geometry of the electric currents in the shower [65]. As is shown in the present work, the presence of strong atmospheric electric fields affects not only the magnitudes of the induced currents but, equally important, their spatial extent and thus the frequencies at which coherent radio waves are emitted.

There are several models proposed to describe radio emission from air showers: the macroscopic models MGMR [31], EVA [66] calculating the emission of the bulk of electrons and positrons described as currents; the microscopic models ZHAires [30], CoREAS [29] based on full Monte Carlo simulation codes; and SELFAS2 [67], a mix of macroscopic and microscopic approaches. All approaches agree in describing the radio emission [34].

First measurements of the radio footprint of extensive air showers, made during periods when there were thunderstorms in the area, so-called thunderstorm conditions, have been reported by the LOPES [68, 69] Collaboration. It was seen that the amplitude of the radiation was strongly affected by the atmospheric electric fields [70]. More recently detailed measurements of the radio footprint, including its polarization were reported by the LOFAR [71] Collaboration. The latter observations make use of the dense array of radio antennas near the core of the LOFAR radio telescope [23], a modern radio observatory designed for both astronomical and cosmic ray observations (see Fig. 2.1). At LOFAR two types of radio antennas are deployed where most cosmic ray observations have been made using the low-band antennas (LBA) operating in the 30 MHz to 80 MHz frequency window which is why we concentrate on this frequency interval in this work. In the observations with LOFAR, made during thunderstorm conditions, strong distortions of the polarization direction as well as the intensity and the structure of the radio footprint were observed [71]. These events are called 'thunderstorm events' in this work. The differences from fair-weather radio footprints of these thunderstorm events can be explained as the

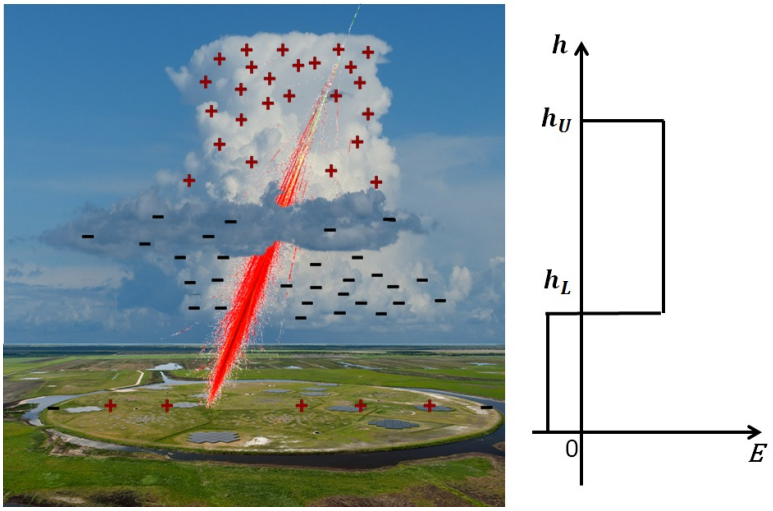

Fig. 2.1 A schematic structure of a thundercloud is given where charge is accumulated at the bottom and the top layers. An air shower (in red) is passing through the thundercloud. The LOFAR core is seen as a circular structure on the ground where a few LOFAR antenna stations can be distinguished. The structure of the induced electric field is given schematically on the right-hand side.

result of atmospheric electric fields and, in turn, can be used to probe the atmospheric electric fields [71].

The effect of the atmospheric electric field on each of the two driving mechanisms of radio emission, transverse current and charge excess, depends on its orientation with respect to the shower axis. As we will show, the component parallel to the shower axis, $\mathbf{E}_{\parallel}$, increases the number of either electrons or positrons, depending on its polarity, and decreases the other. However, there is no evidence that this expected change in the charge excess is reflected in a change in the radio emission as can be measured with the LOFAR LBAs. The component perpendicular to the shower axis, $\mathbf{E}_{\perp}$, does not affect the number of particles but changes the net transverse force acting on the particles. As a result, the magnitude and the direction of the transverse current change, and thus the intensity and the polarization of the emitted radiation do as well. However, simulations show that when increasing the atmospheric electric

field strength up to $E_\perp = 50$ kV/m, the intensity increases, as expected naively, after which the intensity starts to saturate.

In this work, we show that the influence of atmospheric electric fields can be understood from the dynamics of the electrons and positrons in the shower front as determined from Monte Carlo simulations using CORSIKA [11]. The electron dynamics is interpreted in a simplified model to sharpen the physical understanding of these findings.

2.2 Radio emission simulations

The central aim of this work is to develop a qualitative understanding of the dependence of the emitted radio intensity on the strength of the atmospheric electric field. For the simulation we use the code CoREAS [29] which performs a microscopic calculation of the radio signal based on a Monte Carlo simulation of the air shower generated by CORSIKA [11]. The input parameters can be found in the Appendix. The particles in the shower are stored at an atmospheric depth of 500 g/cm^2, corresponding to a height of 5.7 km, near $X_{\max}$, the atmospheric depth where the number of shower particles is largest, for later investigation of the shower properties. The radio signal is calculated at sea level as is appropriate for LOFAR. The pulses are filtered by a 30 MHz to 80 MHz block bandpass filter corresponding to the LOFAR LBA frequency range. The total power is the sum of the amplitude squared over all time bins. The radiation footprints, representing the total power, (see Fig. 2.2 and Fig. 2.3) are plotted in the shower plane, with axes in the directions of $\mathbf{v} \times \mathbf{B}$ and $\mathbf{v} \times [\mathbf{v} \times \mathbf{B}]$.

We have checked that proton induced showers show very similar features to those presented here. We study iron showers to diminish effects from shower-to-shower fluctuations. Since these fluctuations are due to the stochastic nature of the first high-energy interactions, they are larger in proton showers than in iron showers where there are many more nucleons involved in the initial collision. These fluctuations tend to complicate the interpretation of the numerical calculations since the changes observed in the radio emission pattern can be due to these fluctuations or, more interestingly, to the effects of atmospheric electric fields.

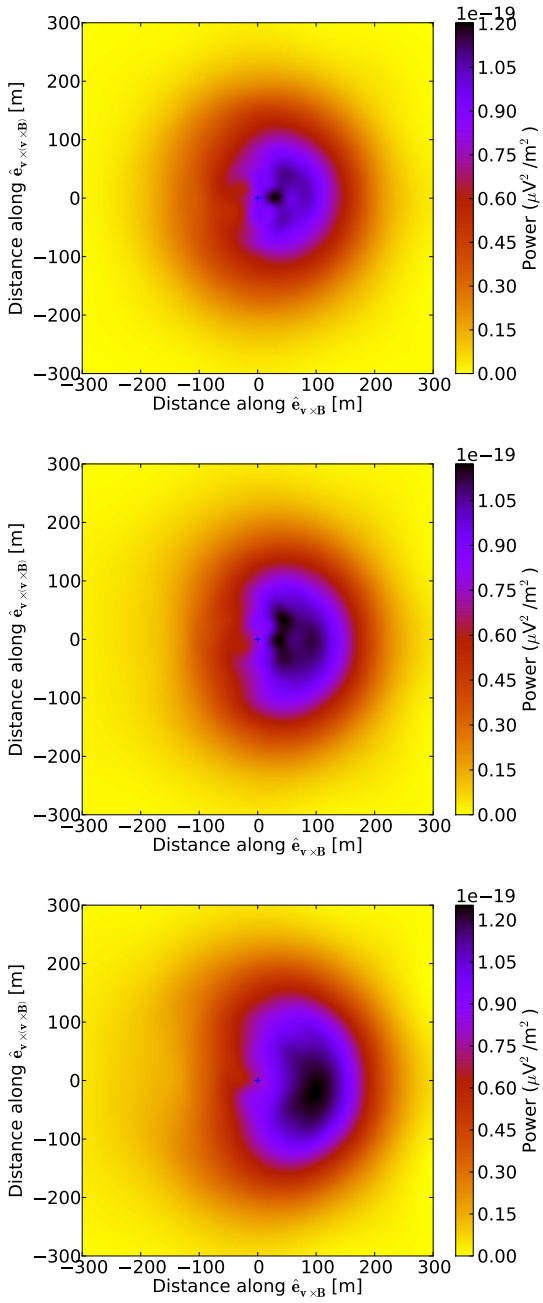

Fig. 2.2 Intensity footprints of 10^{15} eV vertical showers for the $30-80$ MHz band for the case of no electric field (top), $E_{\parallel}$ = 50 kV/m (middle), and $E_{\parallel}$ = 100 kV/m (bottom).

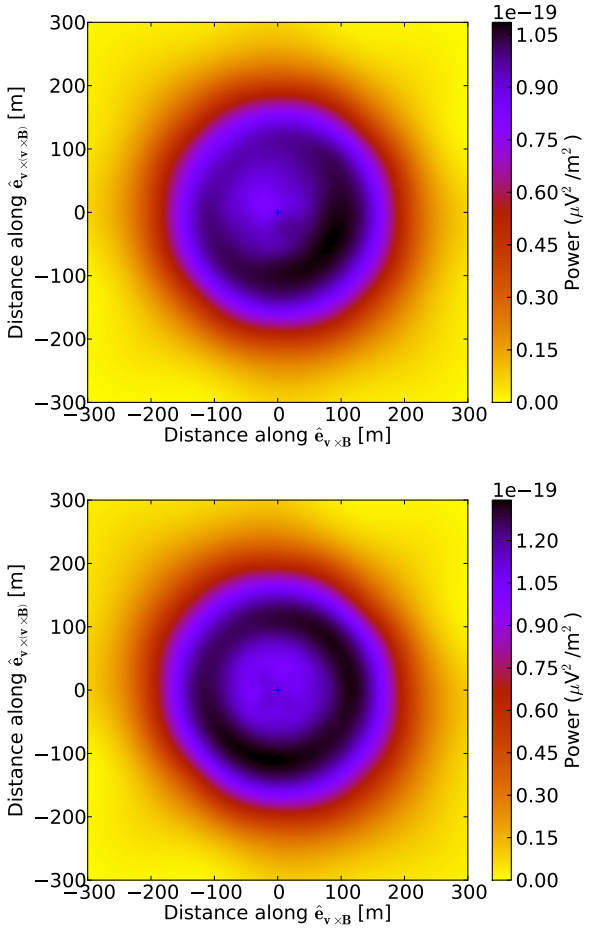

Fig. 2.3 Intensity footprints of 10^{15} eV vertical showers for the $30-80$ MHz band for the case of $F_{\perp} = 50$ keV/m (top) and $F_{\perp} = 100$ keV/m (bottom).

As the aim of this paper is to obtain a deeper insight in the dependence of the radio footprint of an extensive air shower on the strength of the electric fields, we have concentrated on one particular atmospheric field configuration that appears typical for at least half the events that are recorded under thunderstorm conditions. We assume a two-layer electric field configuration much like the one introduced in Ref. [71]. This structure of the fields is schematically shown in Fig. 2.1. Physically, this field configuration can be thought to originate from a charge accumulation at the bottom and the top of a thunderstorm cloud. The boundaries between the layers are set at $h_L = 3$ km and $h_U = 8$ km. The height of 3 km is typical for the lower charge layer in the Netherlands (see Fig. 1 in Ref. [72] showing an ice containing cloud as an example). In thunderclouds, the upper charge layer would typically be above 8 km altitude. In this work, the height of 8 km is chosen since we are not sensitive to even higher altitudes, where there are few air-shower particles [71]. The strength of the field in the lower layer is fixed at a certain fraction of the value of the field in the upper layer, ranging from h_L till h_U, oriented in the opposite direction. The orientation of the electric field is not necessarily vertical, as it depends on the orientation of the charge layers. Finding the orientation of the field is thus an important challenge for the actual measurement. As we will show in the following sections, the sensitivity of the radio footprint is rather different for fields parallel and perpendicular to the direction of cosmic ray. To show this, we study these two cases separately in order to have a discussion of these sensitivities as cleanly as possible. This may give rise to an unphysical field structure in some cases (see Sec. 2.2.2). To obtain a physical field configuration with vanishing curl, one could have added a parallel component where the magnitude depends on the assumed orientation of the charge layer. We have opted not to introduce this arbitrariness, since the sensitivity to the parallel electric field is small. In this work we consider field strengths in the upper layer of up to 100 kV/m which is below the runaway breakdown limit of 284 kV/m at sea level [55, 56] and of 110 kV/m at 8 km. Balloon observations show that the electric fields vary with altitude [73]. The electric fields used in the simulations are homogeneous within each layer and should be considered some average field. In Sec. 2.3.6, we argue that due to intrinsic inertia in the shower development, the field effects are necessarily averaged over distances of the order of 0.5 km. The change of orientation of the electric field at the height h_L introduces a destructive interference between the radio

emission of air showers in the two layers, generating a ring-like structure in the radio footprint. Electric fields in thunderstorm conditions can be more complicated than the simple structure assumed here, which will be reflected in more intricate radio footprints (see Ref. [71] for an example). These more complicated configurations will be the subject of a forthcoming article. It should be noted that the insight in the particle motion at the air-shower front under the influence of electric fields presented in this work is independent of the detailed structure of the field configuration.

2.2.1 Parallel electric field

To study the effects of a parallel electric field, the strength of the field in the upper layer is taken in the direction of the shower and is varied from 0 to 100 kV/m in steps of 10 kV/m. The upper-layer field points upward along the shower axis and accelerates electrons downward. The field in the lower layer is set at $k = 0.3$ times the value in the upper layer, pointing in opposite direction. For simplicity we consider vertical showers. As can be seen from Fig. 2.4 the total number of electrons and positrons at the shower maximum increases with increasing electric field while the square root of the power $\sqrt{I}$ in the radio pulse remains almost constant. The number of electrons increases with increasing electric field while the number of positrons, not shown here, lightly decreases. Since there are fewer positrons than electrons, the total number of electrons and positrons still increases. Thus, for coherent emission, where the amplitude of the signal is proportional to the total number of electrons and positrons, one expects the signal strength to increase proportionally to the total number of particles with the electric field. The simulation results in Fig. 2.4 show clearly that, contrary to this expectation, the square root of the power $\sqrt{I}$ is almost constant. These features will be explained in Sec. 2.3.3. The fluctuations in the $\sqrt{I}$ are due to shower-to-shower fluctuations. The difference in the $\sqrt{I}$ (after scaling) between the 10^{15} eV shower and the 10^{16} eV shower appears due to slight difference in X_{max}.

As explained in Sec. 2.3.3, the observed limited dependence is due to the fact that the additional low-energy electrons in the shower trail behind the shower front at a relatively large distance and thus do not contribute to coherent emission at

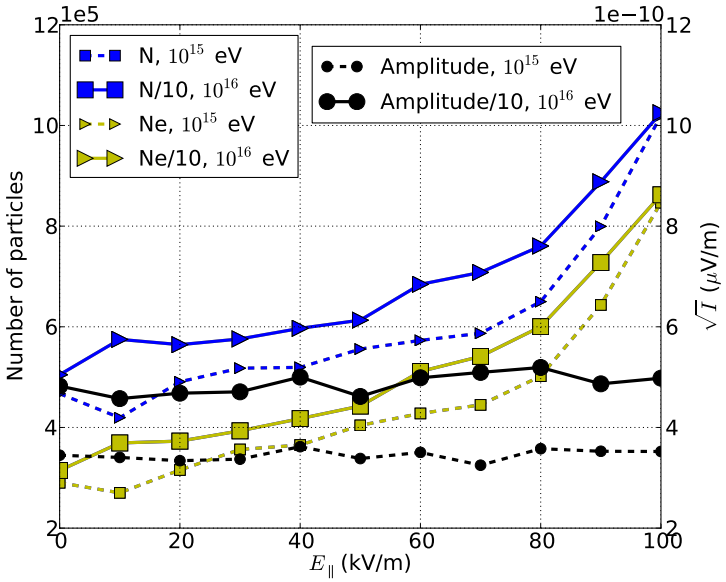

Fig. 2.4 The number of electrons and positrons at the shower maximum (blue left axis), the number of electrons at the shower maximum (yellow left axis), and the maximum $\sqrt{I}$ (black right axis) for vertical 10^{15} eV showers (dashed lines) and for vertical 10^{16} eV showers (right solid lines) as a function of the parallel electric fields. For the 10^{16} eV showers, the number of particles and the pulse amplitude are scaled down by a factor of 10.

the observed frequencies. The trailing behind the shower front of the low-energy electrons was also shown in Ref. [74], but for the breakdown region.

Not only the strength of the signal, but also the structure of the radio footprints for the LOFAR LBA frequency range, as shown in Fig. 2.2, does not really depend on the strength of the parallel electric field. Furthermore, the bean shape (see the top panel of Fig. 2.2), typically observed in air showers in fair-weather condition, is also present in these footprints because the parallel electric fields have small effects on both the transverse-current and the charge-excess components.

2.2.2 Transverse electric field

To investigate the effect of a transverse electric field, we will take a simple geometry with a vertical shower and horizontally oriented electric fields. As mentioned in Sec. 2.2, this does give rise to the situation where at height h_L the horizontal component changes sign, giving rise to a finite value for curl(E) which is not physical. This should, however, be regarded as the limiting result of the case where the cosmic ray is incident at a finite zenith angle crossing an almost horizontal charge layer. At the charge layer the direction of the electric field changes, i.e. the components transverse as well as those longitudinal to the shower direction are changed. Here, we concentrate on the transverse component.

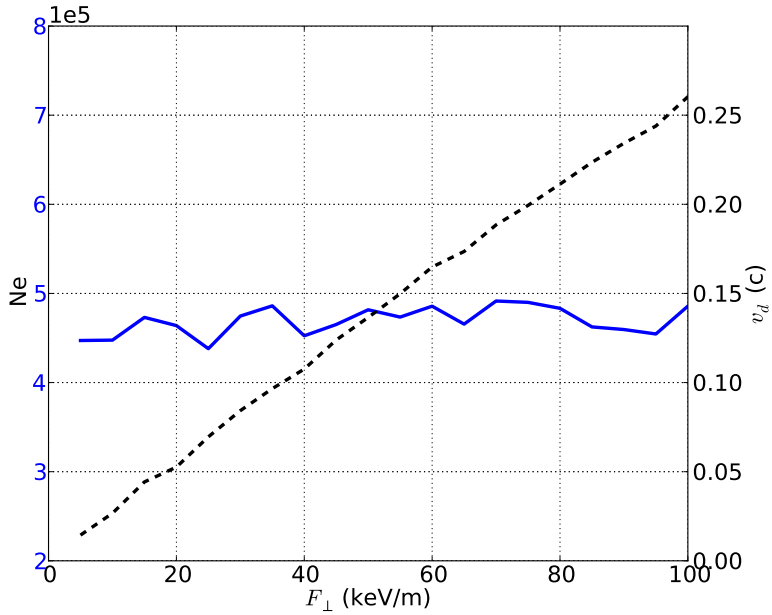

Fig. 2.5 The number of electrons (solid blue line, left axis) and their drift velocity at X_{max} (dashed black line, right axis) of vertical 10^{15} eV showers as a function of the net-transverse forces.

The transverse electric field does not change the number of electrons, but instead increases the magnitude and changes the direction of the drift velocity of the electrons.

This is shown in Fig. 2.5 where the results of simulations are shown for vertical 10^{15} eV showers for the case in which the net force on the electrons (the sum of the Lorentz and the atmospheric electric field) is oriented transversely to the shower at an angle of 45° to the $\mathbf{v} \times \mathbf{B}$ direction. The strength of the net transverse force in the upper layer is varied from 5 keV/m to 100 keV/m in steps of 5 keV/m. For the lower level, the electric field is chosen such that the net force acting on the electrons is a fraction 0.3 of that in the upper layer. One observes that the number of electrons at the shower maximum stays rather constant while the transverse-drift velocity of these electrons increases almost linearly with the strength of the net force. The induced transverse current thus increases linearly with the net force.

Due to a strong increase in the transverse current contribution while the charge excess contribution remains constant, the asymmetry in the pattern diminishes and the radio footprint attains a better circular symmetry around the shower core. The interference between radio emission in two layers introduces a destructive interference near the core which results in a ring-like structure in the intensity footprint, which can clearly be distinguished in Fig. 2.3. At the ring the signal reaches the maximum value. For the case of $F_\perp = 50$ keV/m (top panel of Fig. 2.3), there is an asymmetry along the 45° axis which is the direction of the net force $\mathbf{F}_\perp$ and results from the interference with the charge-excess component. For $F_\perp = 100$ keV/m this asymmetry is even smaller.

Interestingly, Fig. 2.6 shows that the square root of the power $\sqrt{I}$ is proportional to the net force until about 50 keV/m where it starts to saturate. This appears to be a general feature, independent of shower geometry. As we will argue in Sec. 2.3.4, the saturation of the $\sqrt{I}$ is due to loss of coherence, since with increasing transverse electric field the electrons trail at larger distances behind the shower front.

2.3 Interpretation

The radio emission simulation results clearly show that the strength of the radio signal saturates as a function of the applied transverse electric field and seems to be insensitive to the parallel component of the electric field. In this section we explain these observations on the basis of the electron dynamics as can be distilled from Monte Carlo simulations using CORSIKA. To interpret these, we will use a

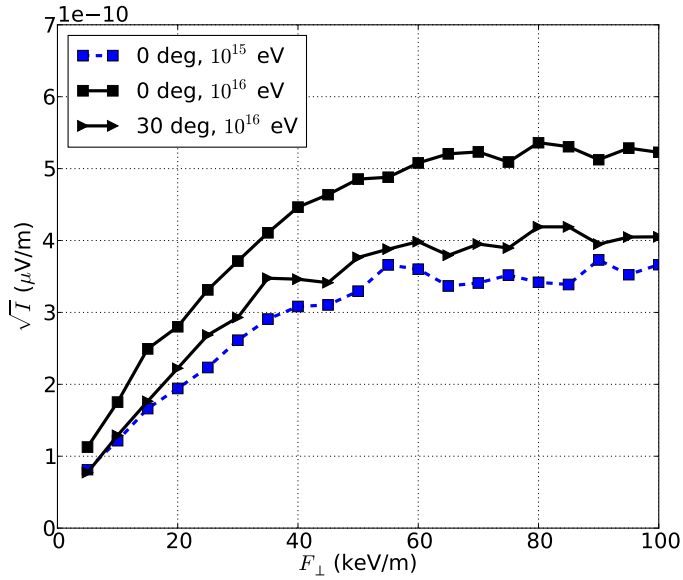

Fig. 2.6 The square root of the power $\sqrt{I}$ at the ring of maximal intensity for vertical 10^{15} eV showers (dashed line) as well as for vertical and inclined 10^{16} eV showers (solid lines) as a function of the net transverse force. For the 10^{16} eV showers the $\sqrt{I}$ is scaled down by a factor of 10.

simplified picture for the motion of the electrons behind the shower front. Since effects of electric fields on electrons and positrons are almost the same but opposite in direction, we will, to simplify the discussion, concentrate on the motion of electrons.

The central point in the arguments presented here is the fact that the emitted radio-frequency radiation is coherent. The intensity of coherent radiation is proportional to the square of the number of particles, while for incoherent radiation it is only linearly proportional. Since the number of particles is large, many tens of thousands, this is an important factor. To reach coherence, the retarded distance between the particles should be small compared to the wavelength of the radiation. For the present cases, most of the emission is in near forward angles from the particle cascade which implies that the important length scale is the distance the electrons trail behind the shower front [59]. When this distance is typically less than half a wavelength, the electrons contribute coherently to the emitted radiation. For the LOFAR frequency

window of $30-80$ MHz, we assume that this coherence length to be 3 m. The challenge is thus to understand the distance the electrons trail behind the shower front.

In the discussion in this paper, we distinguish a transverse force acting on the electrons and a parallel electric field. The transverse force is the (vectorial) sum of the Lorentz force derived from the magnetic field of the Earth and the force due to a transverse electric field. We limit our analysis to the electrons having an energy larger than 3 MeV, since lower-energetic ones contribute very little to radio emission.

2.3.1 Energy-loss time of electrons

In the simplified picture we use for the interpretation of the Monte Carlo results we will assume that the energetic electrons are created at the shower front with a relatively small and randomly oriented transverse momentum component. Like the nomenclature used for the electric field, *transverse* implies transverse to the shower axis, which is in fact parallel to the shower front. After being created, the energetic electron is subject to soft and hard collisions with air molecules, through which it will loose energy. For high-energy electrons the Bremsstrahlung process is important, through which they may loose about half their energy. The radiation length for high-energy electrons in air, mostly due to Bremsstrahlung, is $X_0 \sim 36.7$ g/cm^2 [75], and their fractional energy loss per unit of atmospheric depth is $a = 1/X_0 = 0.0273$ cm^2/g [76]. In the low-energy regime, for energies larger than 3 MeV, soft collisions with air molecules take over which hardly depend on the initial energy of the electrons, and the energy loss per unit of atmospheric depth is almost constant, $b = 1.67$ MeV cm^2/g [76]. The energy loss for low-energy as well as high-energy electrons can thus be parameterized as

$$-\frac{dU}{dX} = aU + b, \tag{2.1}$$

where U is the energy of electrons and X is the atmospheric depth.

The distance L (in [g/cm^2]) over which the electron energy is reduced to a fraction $1/\xi$ of the original energy, i.e. they lose an energy of $\Delta U = (1-1/\xi)U$, is thus

$$L_\xi = \frac{1}{a} \ln \left[\frac{aU_0 + b}{aU_0/\xi + b} \right] . \tag{2.2}$$

Since these particles move with a velocity near the speed of light, where we use natural units $c = 1$, this corresponds to an energy-loss time τ_ξ, given by

$$\tau_\xi(U) = \frac{L}{\rho} = \frac{1}{a\rho} \ln \left[\frac{aU_0 + b}{aU_0/\xi + b} \right] . \tag{2.3}$$

The air density ρ is approximately [53]

$$\rho(z) = 1.208 \times 10^{-3} \exp(z/8.4) \text{ g/cm}^3 , \tag{2.4}$$

where z is the altitude in km.

In our picture, developed to visualize the results from the full-scale Monte Carlo simulations, the energy-loss time plays a central role since it is the amount of time over which we will follow the particles after they are created at the shower front. In our picture this thus plays the role of a lifetime of the electrons after which they are assumed to have disappeared and may have reappeared as a lower-energy electron or have been absorbed by an air molecule. In this energy-loss time, $\tau(U)$, thus several more complicating effects have been combined, such as the following:

1. In reality, electrons of energy U are created by more energetic particles. They are already trailing some distance behind the front. This additional distance is absorbed in the definition of $\tau(U)$.

2. Once an electron is created at a certain energy, we do not take its energy loss into account in calculating the properties of the shower front. Such a formulation can only be applied within a limited range of lost energy.

We will take both effects into account by making an appropriate choice for the parameter ξ. One consequence of the parametrization, which can be tested directly with simulations, is that the median distance from the shower front of electrons (see Eq. (2.13)) does not depend on the primary energy of showers. As shown in

Fig. 2.7, this is obeyed rather accurately, and furthermore, the energy-dependence of the median distance behind the shower front, calculated using the approach discussed in the following section, can be fitted reasonably well by taking $\xi = e$. We thus define

$$\tau(U) = \frac{L}{\rho} = \frac{1}{a\rho} \ln\left[\frac{aU_0 + b}{aU_0/e + b}\right] . \tag{2.5}$$

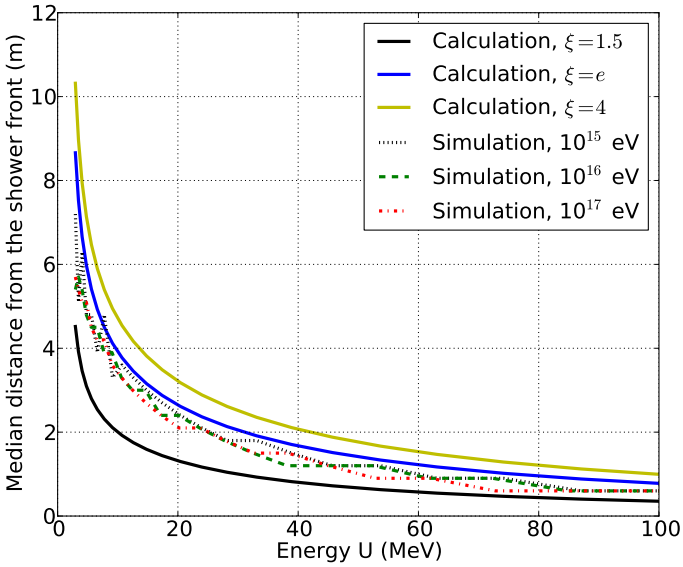

Fig. 2.7 The median distance from the shower front of electrons for vertical 10^{15} eV, 10^{16} eV and 10^{17} eV showers in the absence of electric fields. The simple prediction based on Eq. (2.5) and Eq. (2.13) is also shown.

2.3.2 Trailing distance

As written before, we assume that the electrons are generated at the shower front and from there drift to larger distances. Assuming the electrons disappear from the process after a time τ, the electrons are generated at the shower front at a rate

$$\frac{dP(U)}{dt} = P_0(U)\frac{1}{\tau} , \tag{2.6}$$

where $P_0(U)$ is the energy distribution at the shower maximum, as for example given by [77]

$$P_0(U) = \frac{dN}{d(\ln \frac{U}{1\mathrm{MeV}})} = \frac{U_0 U}{(U+U_1)(U+U_2)}\,, \tag{2.7}$$

where U_0, U_1, U_2 are parameters that are determined from a Monte Carlo simulation. The creation rate, Eq. (2.6), has been chosen such that the energy distribution in the shower pancake agrees with the observations

$$P(U) = \int_0^\tau \frac{dP(U)}{dt}\,dt = P_0(U)\,. \tag{2.8}$$

The parameters in Eq. (2.7) are chosen to reproduce the electron spectrum from the simulation at 10^{15} eV giving $U_0 = 10^6$ MeV, $U_1 = 4.11$ MeV, and $U_2 = 105$ MeV.

To obtain an estimate of the distance the electrons trail behind the shower front, we calculate the difference in forward velocity of the front and the electrons. The air-shower front moves with the speed of light, while the electrons (mass m_0, energy U, random transverse momentum $P_\perp$ and longitudinal momentum $P_\parallel$) travel with a longitudinal velocity $v_\parallel$ which is less than c, given by

$$v_\parallel = \frac{P_\parallel}{U} = \frac{\sqrt{U^2 - m_0^2 - P_\perp^2}}{U} \approx 1 - \frac{m_0^2 + P_\perp^2}{2U^2}\,, \tag{2.9}$$

where $\left(m_0^2 + (P_\perp)^2\right)/U^2$ is assumed to be much smaller than 1. After a time t, due to the velocity difference between the shower front and the electrons, the electrons are trailing behind the shower front by a distance

$$l = \int_0^t (c - v_\parallel)dt\,. \tag{2.10}$$

Using the assumption that the energy of the electrons does not change significantly during the energy-loss time, and taking in addition $P_\perp$ to be time independent, one obtains

$$l = \frac{1}{2}\frac{\left(m_0^2 + P_\perp^2\right)}{U^2}t\,, \tag{2.11}$$

Based on the results of CORSIKA simulations we can introduce an effective mass of the electrons that includes the stochastic component of the transverse momentum,

which is parameterized as

$$m_\perp^2 = \langle m_0^2 + P_\perp^2 \rangle = m_0^2 \left[1 + 10 \left(U/m_0 \right)^{2/3} \right] . \tag{2.12}$$

The median distance by which an electron can trail behind the shower front within its energy-loss time τ, D, can now be written as

$$D = l(\tau/2) = \frac{m_\perp^2 \tau}{4U^2} \tag{2.13}$$

and is shown in Fig. 2.7.

In the Monte Carlo simulation results shown in Fig. 2.7 as well as those discussed in the following sections the trailing distances are calculated with respect to a flat shower front thus ignoring the fact that in reality the shower front is curved. It has been checked that the corrections due to this curvature effect for distances up to 100 m from the shower core do not exceed 30 cm and thus can be ignored. In addition, electrons at very low energies do not contribute significantly to radio emission. Therefore, we have limited the analysis to the electrons having energies larger than 3 MeV and a distance to the shower core of less than 100 m.

2.3.3 Influence of $\mathbf{E}_\parallel$

When a parallel electric field $\mathbf{E}_\parallel$ is applied to accelerate electrons downward, the CORSIKA results show a strong increase in the number of electrons (see Fig. 2.8) as well as in the trailing distance behind the shower front (see Fig. 2.9). To understand these trends in our simple picture, we first investigate the effect of the applied electric field on the energy-loss time.

When a parallel electric field $\mathbf{E}_\parallel$ is applied to accelerate electrons downward, the electrons gain energy from the electric field. Therefore, the energy-loss equation for the electrons is modified to

$$-\frac{dU}{dX} = aU + b - F_E/\rho \,, \tag{2.14}$$

where $F_E = eE$. Since the field strengths we will consider are below the break-even value $E_{be}(z) = 1.67 \times 10^6 \, \rho(z)$ V/cm [53] the electrons always lose energy, and the

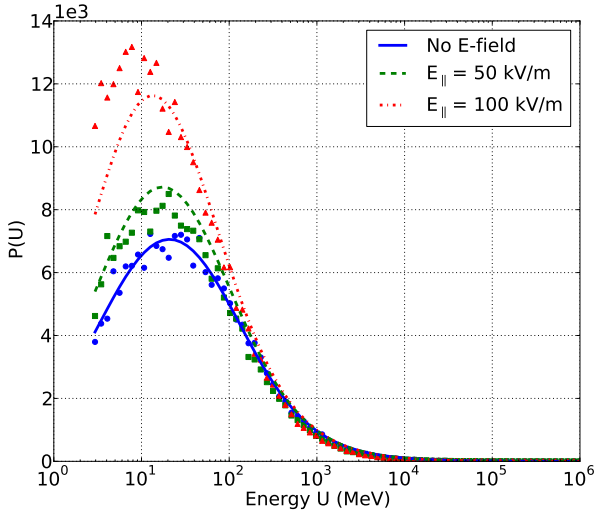

Fig. 2.8 The number of electrons is shown as a function of their energy for electric fields $E = 0$, $E_{\parallel} = 50$ kV/m, and $E_{\parallel} = 100$ kV/m as obtained from the analytical calculations (solid and dashed curves) and from full CORSIKA simulations (markers) at $X = 500$ g/cm^2.

r.h.s. of Eq. (2.14) is always positive. Stated more explicitly, we are not modelling the runaway breakdown process, and we have therefore limited the electric field to strengths below the breakdown value of 100 kV/m at an altitude of 5.7 km.

The energy-loss time of the electrons inside the electric field is now modified to

$$\tau_E = \frac{L_E}{\rho} = \frac{1}{a\rho} \ln \left[\frac{aU_0 + b - F_E/\rho}{aU_0/e + b - F_E/\rho} \right] . \tag{2.15}$$

Fig. 2.10 shows that the energy-loss time of low-energy electrons is larger in the presence of the electric field than in the absence of it. Inside the electric field, the low-energy electrons gain energy from the field; it thus takes longer for their energy to drop below the fraction $1/\xi$ of their original energy, and thus, according to our definition, they live longer. In the high-energy regime, the electrons also gain energy from the electric field, but this gained energy is small compared to their own energy. As a result, the energy-loss time of high-energy electrons is almost unchanged.

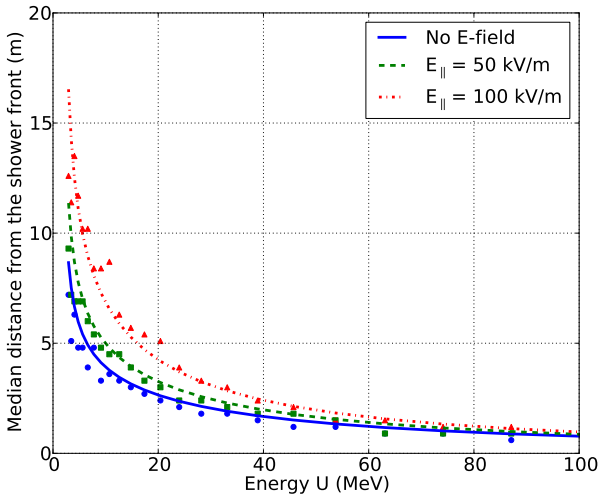

Fig. 2.9 The distance by which the electrons travel in the absence and in the presence of the parallel electric fields from analytical calculations (solid and dashed curves) and from CORSIKA simulations (markers).

The generation rate of electrons at the shower front will remain unchanged and is given by Eq. (2.6). The number of electrons in the shower pancake changes from Eq. (2.8) to

$$P_E(U) = \int_0^{\tau_E} \frac{dP(U)}{dt}\, dt = P_0(U)\frac{\tau_E}{\tau}\,. \tag{2.16}$$

Since in the low-energy regime $\tau_E > \tau$, there is an increase in the number of low-energy electrons. In the high-energy regime, on the other hand, where $\tau_E \approx \tau$, the number of electrons is almost unchanged. Fig. 2.8 shows that this simple calculation can reproduce the main features shown in the CORSIKA simulations rather well, except for a small disagreement at the low-energy region in the presence of the electric field of 100 kV/m. The presently considered field accelerates the electrons and thus decelerates the positrons. As a consequence, the positron energy-loss time decreases, resulting in a rather large decrease of the number of low-energy positrons, while the number of high-energy positrons stays almost constant.

When the electron is subject to an electric field, the energy-loss time is given by Eq. (2.15) instead of by Eq. (2.5), and as a result, the expression for the median

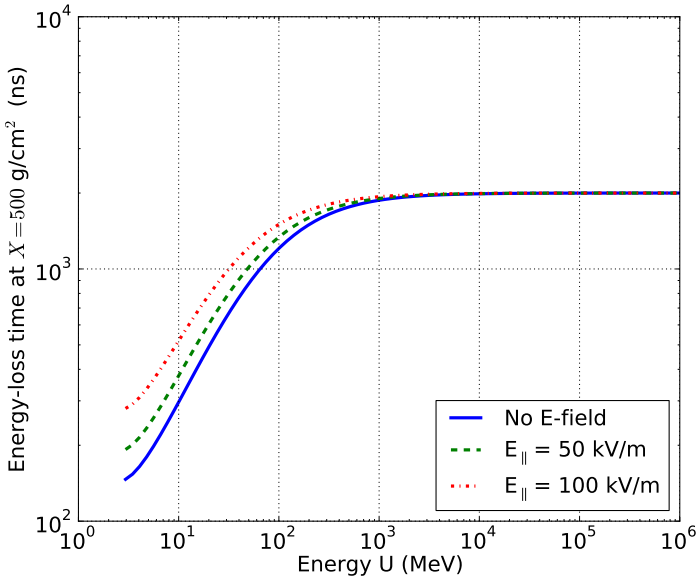

Fig. 2.10 The energy-loss time of electrons at $X = 500$ g/cm^2 (at X_{max}) in the absence and in the presence of parallel electric fields.

trailing distance, Eq. (2.13), changes to

$$D(E_\parallel) = \frac{m_\perp^2 \tau_E}{4U^2} \,, \tag{2.17}$$

where the mean transverse momentum is given by Eq. (2.12). The effect of the electric field on the median trailing distance is shown in Fig. 2.9. Due to the influence of the electric field, the low-energy electrons trail much further behind the shower front. The median trailing distance as calculated from CORSIKA simulations is also displayed in Fig. 2.9. It shows that our simplified picture correctly explains the trends seen in the full Monte Carlo simulations using the CORSIKA simulations. In the absence of an electric field the trailing distance sharply decreases with increasing energy. When applying an electric field that accelerates the electrons the Monte Carlo simulations show a considerable increase in the trailing distance behind the shower front. From the present simple picture this can be understood to be generated by the

increased energy-loss time that generates a considerable trailing of electrons with energies below 50 MeV.

The interesting aspect for radio emission is the number of particles within a distance of typically half a wavelength of the shower front. For the LOFAR LBA frequency range, this corresponds to a distance of about 3 m. Using Eq. (2.11) as well as Eq. (2.6) the distribution of the electrons over distance l behind the shower front is given by

$$\frac{dP(U)}{dl} = \frac{dP(U)}{dt}\frac{dt}{dl} = \frac{P_0(U)}{\tau}\frac{2U^2}{\left(m_0^2 + P_\perp^2\right)}\,. \tag{2.18}$$

Therefore, the number of electrons within the distance Δ is

$$P^\Delta(U) = \begin{cases} P_0(U)\frac{\tau_E}{\tau} & U > U_\Delta \\ P_0(U)\frac{U^2\tau_E}{U_\Delta^2\tau} & U \leqslant U_\Delta \end{cases}, \tag{2.19}$$

where the energy-loss time in the presence of an electric field is given by Eq. (2.15) and

$$U_\Delta = \sqrt{\frac{\left(m_0^2 + P_\perp^2\right)\tau_E}{2\Delta}}\,. \tag{2.20}$$

In the absence of an electric field we have, of course, $\tau_E = \tau$ given by Eq. (2.5).

It should be noted that the factor in Eq. (2.19),

$$\frac{U^2\,\tau_E}{U_\Delta^2\,\tau} = \frac{2U^2\Delta}{(m_0^2 + P_\perp^2)\tau}\,, \tag{2.21}$$

is independent of τ_E. At energies below U_Δ (which itself depends on the magnitude of the electric field), the number of electrons within a certain trailing distance is independent of the electric field. This feature is seen in the estimates of Fig. 2.11a as well as in the full Monte Carlo simulations of Fig. 2.11b. At energies exceeding U_Δ, the number of electrons is proportional to τ_E and thus increases with the strength of the electric field. This increase is, however, very moderate compared to the increase of the number of electrons at larger distance; see Fig. 2.11.

In the distance interval from 3 m to 10 m behind the shower front, the number of electrons with an energy less than 20 MeV are significantly enhanced. As a result,

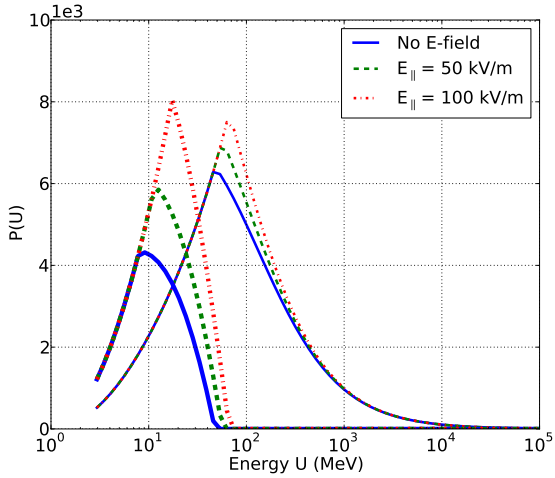

(a) Analytical estimates

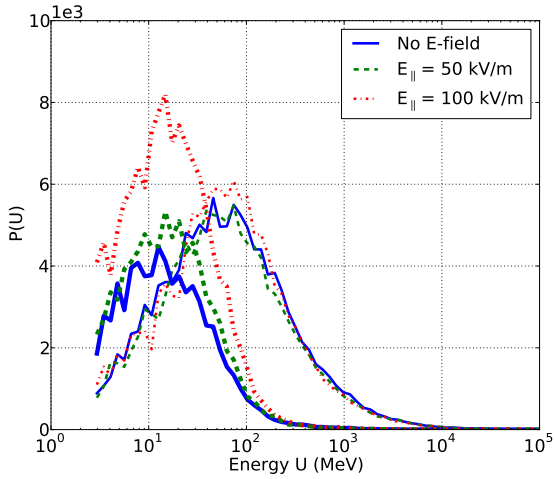

(b) CORSIKA simulations

Fig. 2.11 The energy spectrum of electrons within a distance of 3 m (thin curves) and from 3 m to 10 m (thick curves) behind the shower front for $E = 0$, $E_{\parallel} = 50$ kV/m and $E_{\parallel} = 100$ kV/m at the shower maximum from analytical calculations (top panel) and from full CORSIKA simulations (bottom panel).

there is a strong increase in coherent radiation at larger wavelengths, well below the frequency range of LOFAR LBA, as is shown in Fig. 2.12.

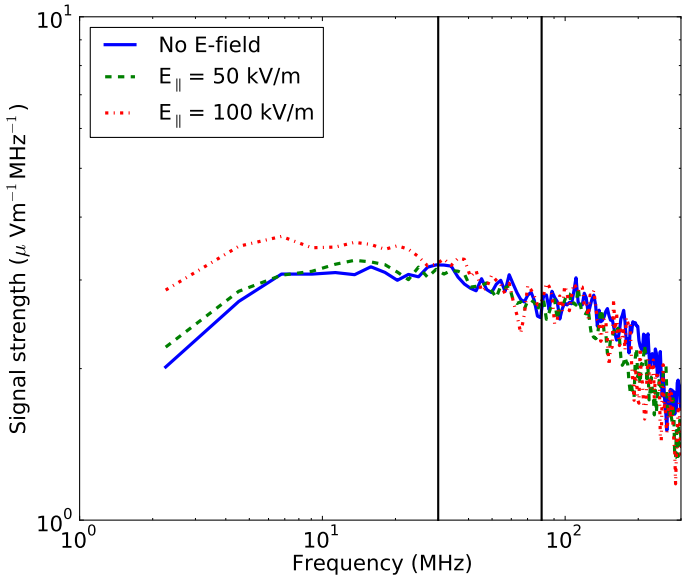

Fig. 2.12 The signal strength, as obtained from CoREAS simulations, as a function of frequency for a vertical shower of 10^{15} eV at 50 m from the core in the absence and in the presence of parallel electric fields. The black vertical lines represent the LOFAR LBA frequency window.

We can thus conclude that an accelerating electric field parallel to the shower axis increases the total number of electrons. The enhancement in the number of electrons occurs mainly at low energy and thus their relative velocity with respect to the shower front is larger than for the high-energy electrons. As a consequence, they are trailing much more than 3 m behind the shower front. Their radiation is thus not added coherently in the LOFAR frequency range but instead in the frequency below 10 MHz. Therefore, the effects of parallel electric fields cannot be observed by LOFAR operating in the frequency of $30-80$ MHz. These effects should be measurable at a lower frequency range.

2.3.4 Influence of $E_\perp$

One important result from the CORSIKA simulations, shown in Fig. 2.13, is that the median trailing distance behind the shower front increases rapidly with increasing transverse force working on the electrons. In order to get some more insight into the dynamics, we try to reproduce this in our simplified picture.

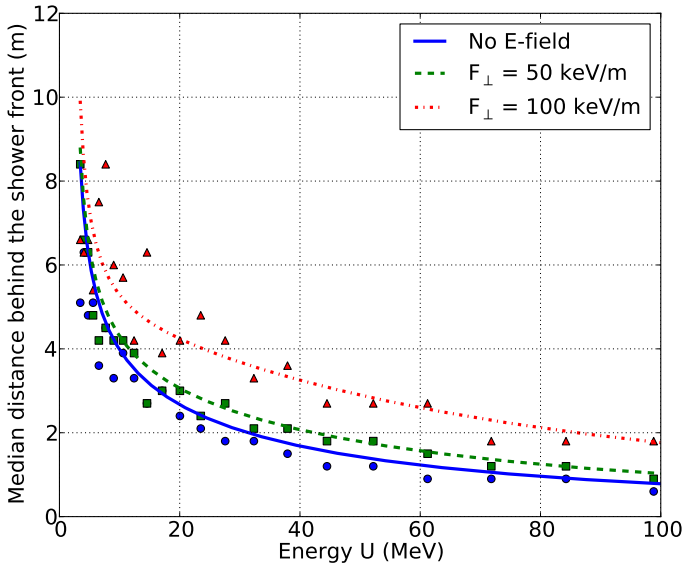

Fig. 2.13 The median distance by which the electrons trail behind the shower front as a function of their energy in the absence and in the presence of a perpendicular electric field as obtained from CORSIKA simulations (markers) in comparison to the model expectation (solid and dashed curves).

When an electric field perpendicular to the shower axis is applied, there is a transverse electric force acting on the electrons and positrons. The transverse net force, which is the vector sum of the transverse electric force and the Lorentz force,

$$\mathbf{F}_\perp = \mathbf{q}\,(\mathbf{E}_\perp + \mathbf{v} \times \mathbf{B}) \ , \tag{2.22}$$

causes the electrons and positrons to move in opposite directions. Since the field is perpendicular to the main component of the velocity, no appreciable amount of work

is done, and the electron energy is not really affected. Thus, the energy-loss time of the electrons remains almost unchanged. As a result, the perpendicular electric field does not change the total number of electrons given by Eq. (2.8), in complete accordance with the results of Monte Carlo simulations.

The electrons are subjected to the transverse force $\mathbf{F}_\perp$, giving rise to a change in transverse momentum

$$F_\perp = \frac{dP_\perp}{dt} \,. \tag{2.23}$$

The average initial transverse momentum in the direction of the force vanishes. The mean transverse momentum is thus

$$\bar{P}_\perp(t) = F_\perp t \;, \tag{2.24}$$

where t is the time lapse after creation. Due to the action of the force, the electrons drift with a velocity

$$\bar{v}_\perp(t) = \frac{\bar{P}_\perp}{U} = \frac{F_\perp t}{U} \;, \tag{2.25}$$

where U is the energy of the electrons. The random component of the transverse momentum is taken into account in the effective transverse mass as introduced in Eq. (2.12). The parallel velocity is thus

$$v_\parallel(t) = \frac{P_\parallel}{U} = \sqrt{1 - \frac{m_\perp^2 + \bar{P}_\perp^2(t)}{U^2}} \approx 1 - \frac{1}{2}\frac{m_\perp^2 + \bar{P}_\perp^2(t)}{U^2} \;. \tag{2.26}$$

The transverse velocity increases when the net force increases, the longitudinal velocity reduces because the total velocity cannot exceed the light velocity. Since the transverse velocity is small, even in strong fields, the electrons trailing within 3 m behind the shower front do not drift more than 100 m sideways. The distance of 100 m we had imposed in order to avoid corrections due to the curved shower front. After a time t, the electrons are trailing behind the shower front by a distance

$$\begin{aligned} l(t) &= \int_0^t \left(c - v_\parallel\right) dt = \int_0^t \frac{m_\perp^2 + \bar{P}_\perp^2(t)}{2U^2} dt \\ &= \frac{m_\perp^2 t}{2U^2} + \frac{F_\perp^2 t^3}{6U^2} \,. \end{aligned} \tag{2.27}$$

The median distance by which an electron can trail behind the shower front within its energy-loss time τ (see Eq. (2.5)) is given by

$$D(E_\perp) = l(\tau/2) = \frac{\tau}{4U^2}\left(m_\perp^2 + \frac{1}{12}F_\perp^2\,\tau^2\right) . \tag{2.28}$$

This equation shows that D quickly decreases with increasing energy, as is seen in Fig. 2.13 as obtained from a CORSIKA simulation. With increasing $F_\perp$, the second term in Eq. (2.28) increases quadratically giving rise to a rapidly increasing trailing distance as is also seen in the simulation. The median distance of low-energy electrons in the presence of the net force of 100 keV/m given by the simulations is larger than the simple prediction because the electron density is small at this energy range and as a sequence there is a fluctuation in the median distance.

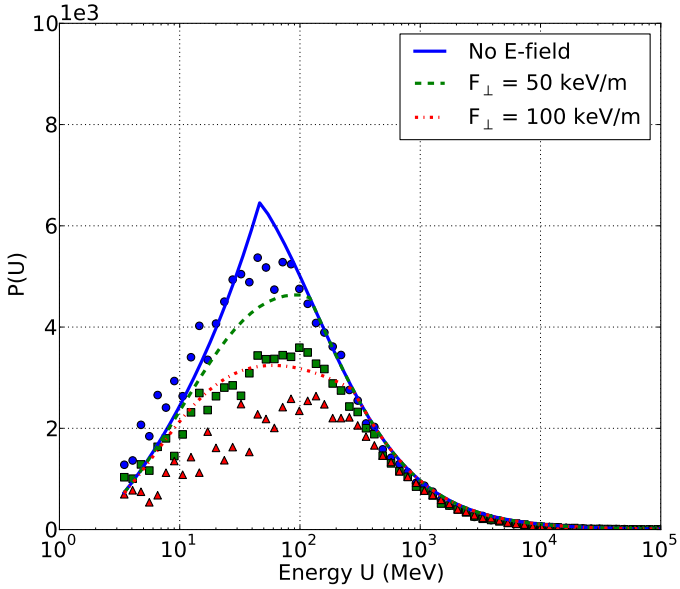

Fig. 2.14 The number of electrons as a function of their energy that are within 3 m behind the shower front with and without perpendicular electric fields at $X = 500$ g/cm^2 as calculated from Eq. (2.29) (solid and dashed curves) and from the full CORSIKA simulations (markers).

Essential for radio emission in the LOFAR LBA frequency band is the total number of the electrons within 3 m behind the shower front. The results of the CORSIKA simulation are displayed in Fig. 2.14. This shows that this number reduces as the transverse net force increases and that this decrease is strongest at those energies where the number of particles is maximal. In our simple picture, the number of electrons within the distance Δ can be calculated by

$$\mathscr{P}^{\Delta}(U) = \int_0^{t_\Delta \leqslant \tau} \frac{P_0(U)}{\tau} dt = \begin{cases} P_0(U) & t_\Delta > \tau \\ P_0(U)\frac{t_\Delta}{\tau} & t_\Delta \leqslant \tau \end{cases}, \tag{2.29}$$

where t_Δ is the root of Eq. (2.28) for $d = \Delta = 3$ m. Note that the equation gives one real root and two complex roots where the real root is taken since t_Δ is a physical quantity. Eq. (2.29) can be simplified by introducing $\tau_\Delta^m = \min(t_\Delta, \tau)$ to $P^\Delta(U) = P_0(U)\tau_\Delta^m/\tau$. In Fig. 2.14, the results from Eq. (2.29) as well as the results from the the simulations are shown for different strengths of electric fields. The number of low-energy electrons reduces in strong fields because of the increase in trailing behind, while the number of higher-energy electrons is stable because they are still close to the front.

An important factor for the current is the drift velocity of the electrons. The results from the CORSIKA simulations are shown in Fig. 2.15. The drift velocity increases with the strength of the net-transverse force and the distance behind the shower front. Within our simple picture, the mean drift velocity of electrons lagging within a distance Δ behind the shower front of the electrons is

$$v_\perp^\Delta(U) = \frac{1}{t_\Delta^m} \int_0^{t_\Delta^m} v_\perp \, dt = \frac{F_\perp \tau_\Delta^m}{2U}, \tag{2.30}$$

where $v_\perp$ is given by Eq. (2.25). From Eq. (2.30) it follows that the drift velocity increases with distance to the shower front as also seen in the Monte Carlo simulations. The main energy region that matters here is that between 50 MeV and 1000 MeV since the particle density in this energy range is largest. Outside of this energy range, the scatter of the simulation results is large, since the electron density is small and one suffers from poor statistics.

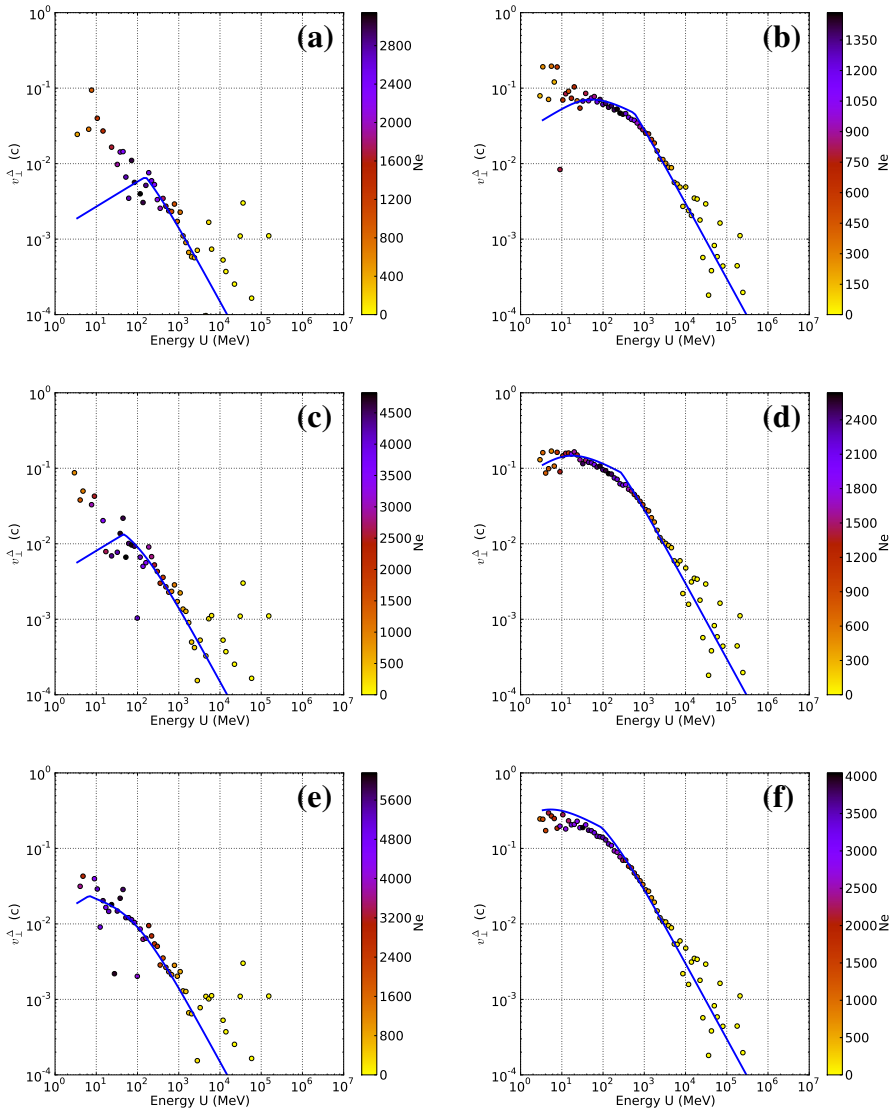

Fig. 2.15 The drift velocity in units of the speed of light at X_{max} of the electrons lagging within a distance Δ = 1 m (a, b), Δ = 3 m (c, d) and Δ = 10 m (e, f) behind the shower front for small ($F_\perp$ = 5 keV/m, (a, c, e)) and large ($F_\perp$ = 100 keV/m, (b, d, f)) transverse net forces from analytical estimates (blue curves) and from CORSIKA simulation results (markers). The colors of the dots represent the number of electrons.

Combining Eq. (2.30) with the expression for the particle density, one obtains the induced current carried by the particles within a distance Δ behind the shower front

$$j_{\perp}^{\Delta}(U) = e\frac{P_0(U)}{\tau}\int_0^{t_{\Delta}^m} v_{\perp}\,dt = \frac{e\,P_0(U)\,F_{\perp}\,(\tau_{\Delta}^m)^2}{2\,\tau\,U}\,. \tag{2.31}$$

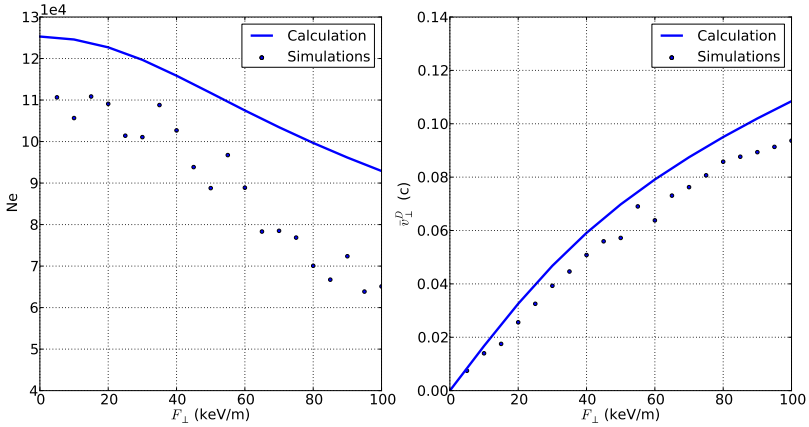

Fig. 2.16 The number of electrons within 3 m behind the shower front (left panel) and their mean drift velocity (right panel) as a function of transverse net forces from analytical calculations and from CORSIKA simulations.

Fig. 2.16 displays the total number of electrons within 3 m behind the shower front and their mean drift velocity as a function of the net-transverse forces. From the simple picture it is understood that in the presence of a perpendicular electric field, the drift velocity of the electrons increases. However, they are lagging further behind the shower front. Therefore, the number of electrons within 3 m behind the shower front reduces, as shown in the left panel of Fig. 2.16. The number in the simple picture is overestimated, and the number does not drop as fast with increasing electric field as follows from the Monte Carlo calculation, but the trends match.

The simulation shows that the mean drift velocity increases with the net-transverse force (right panel of Fig. 2.16); however, there is a change of slope at about 50 keV/m. In the simple picture, this change of slope is due to the fact that the distance behind the front increases quadratically while the drift increases only linearly with increasing transverse force. As a consequence, the induced electric current, which is the product

of the number of electrons and their drift velocity, saturates at 50 keV/m and thus so does the pulse amplitude, since it is proportional to the current.

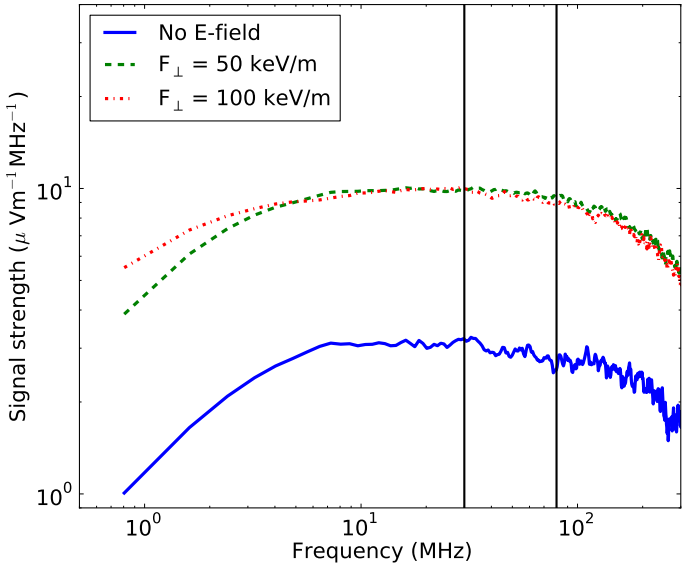

Fig. 2.17 The same as displayed in Fig. 2.12 for different strengths of the net-transverse force.

Since, as just argued, for a large transverse force there is an increased drift velocity at larger distances behind the front one should thus expect an increased emission at longer wavelengths, well below the wavelength measured at LOFAR LBA. The effects of electric fields larger than 50 kV/m can be observed at lower frequency ranges, as shown in Fig. 2.17.

2.3.5 Effects of electric fields in the low-frequency domain

As has been concluded in the previous two sections, the power as can be measured in the LOFAR frequency window of $30-80$ MHz is strongly determined by the strength of the transverse electric field up to values of about 50 kV/m. In addition, parallel electric fields have small effects on the power in the frequency window $30-80$ MHz. It was shown that at lower frequencies, the power keeps growing with

increasing field strength up to at least 100 kV/m. In this section we investigate the usefulness of the $2-9$ MHz window in more detail. This frequency window is of particular interest for several reasons: i) it lies just below a commercial frequency band, ii) the ionosphere shields the Galactic background, and iii) the frequency is high enough to observe a considerable pulse power.

Fig. 2.18 shows that while parallel electric fields have only a minor effect on the emitted power in the frequency range from 30 MHz to 80 MHz, they have much larger effects on the power in the low-frequency windows of $2-9$ MHz. Here an increase of the peak power with the strength of $E_{\parallel}$ is observed. Inside a strong parallel electric field, since the number of low-energy electrons increases and the number of low-energy positrons reduces, the charge-excess component becomes comparable to the transverse-current component. As a result of the interference, the intensity at the highest electric field has not only a strong maximum, but also a clear (local) minimum at 250 m from the shower core in the opposite direction, as seen in the bottom panel of Fig. 2.18. Since these low-energy particles trail far behind the shower front, the change in the intensity pattern is not observed in the LOFAR-LBA frequency range.

Fig. 2.19 displays that in the low-frequency window $2-9$ MHz the maximum intensity increases with the net force to a very similar extent as in the frequency window $30-80$ MHz. The intensity footprint for the net force of 100 keV/m is more symmetric than the one for 50 keV/m because the electrons trail further behind the shower front in a strong transverse electric field and thus the charge-excess contribution becomes smaller. The effects in the two frequency windows, $2-9$ MHz and $30-80$ MHz, are very similar, although somewhat more pronounced at the lower frequencies. To have more leverage on the strength of the perpendicular component of the electric field, one would need to go to even lower frequencies, as is apparent from Fig. 2.17, which may be unrealistic for actual measurements.

The effects of parallel electric fields and large transverse electric fields are measurable at low frequencies from 2 MHz to 9 MHz. Since the intensity footprints become wider in the low-frequency domain (see Fig. 2.18 and Fig. 2.19), measuring signals in this range requires a less dense antenna array than in the LBA frequency domain.

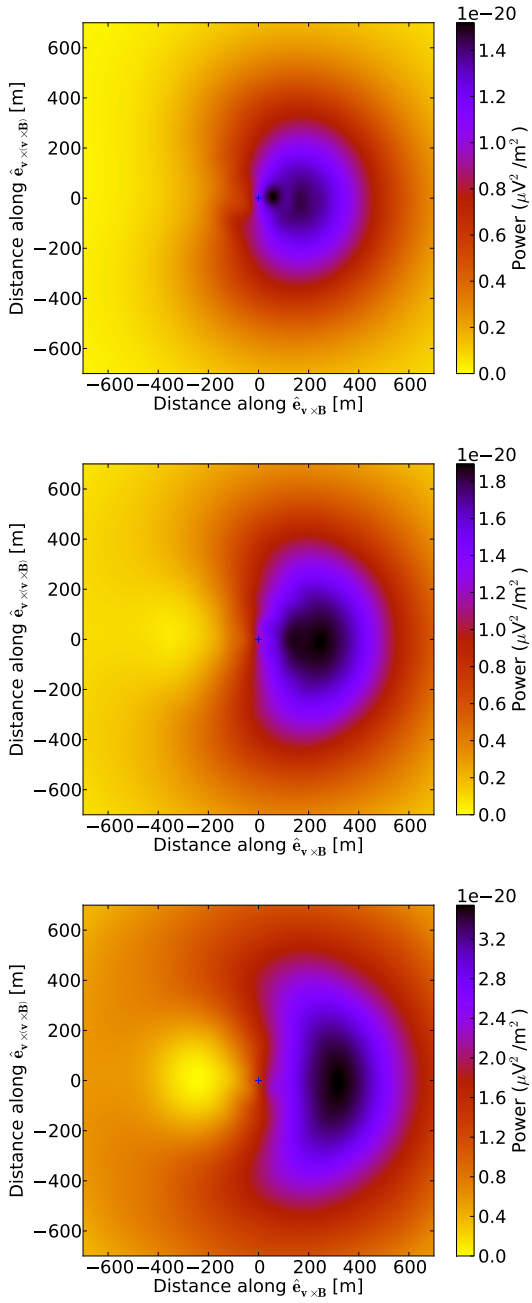

Fig. 2.18 Intensity footprints of 10^{15} eV vertical showers for the $2-9$ MHz band for the cases of no electric field (top), $E_{\parallel} = 50$ kV/m (middle), and $E_{\parallel} = 100$ kV/m (bottom).

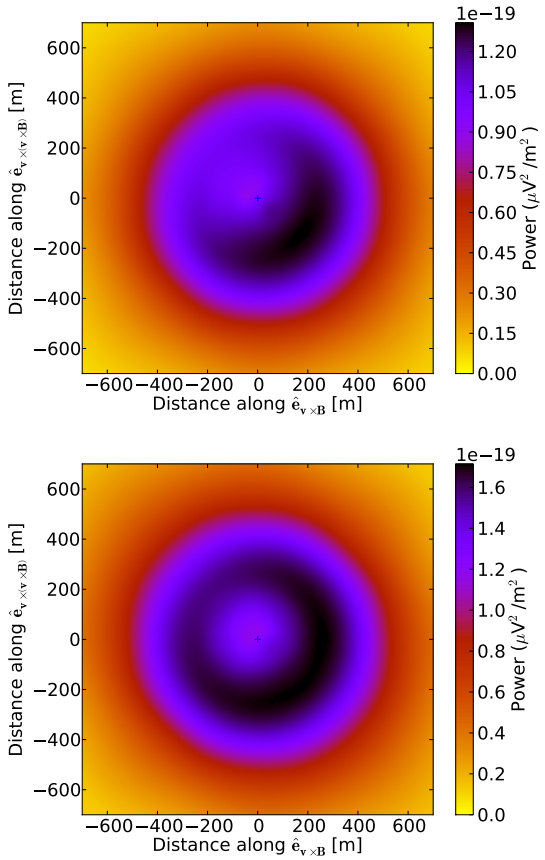

Fig. 2.19 Intensity footprints of 10^{15} eV vertical showers for the 2 - 9 MHz band for the cases of $F_\perp$ = 50 keV/m (top) and $F_\perp$ = 100 keV/m (bottom).

2.3.6 Adapting distance of the effects of E-fields

One interesting aspect to study is the intrinsic distance along the track of the shower over which the electric fields are averaged using radio emission from air showers as a probe. It was also shown in Ref. [74] that the number of positrons adapts quickly to the expected number when the electric field is switched on. To study this in more detail, we have changed the magnitude of the electric field at a certain height and determined the number of particles as a function of height in a CORSIKA calculation. The result is shown in Fig. 2.20, where the particle number is plotted as a function of

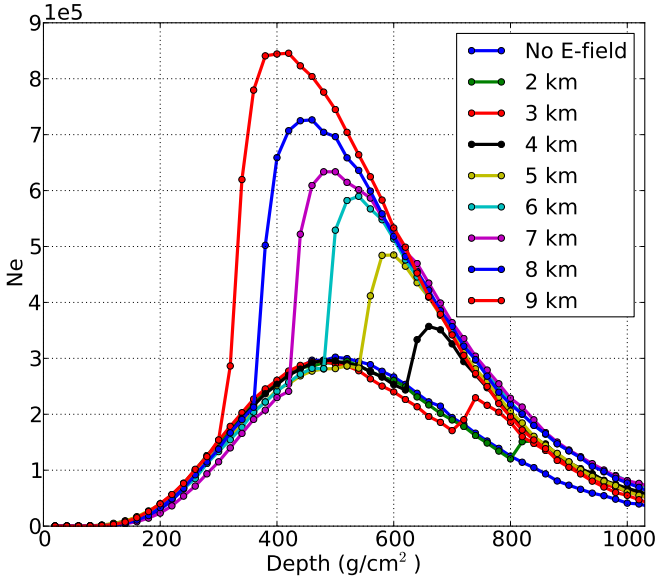

Fig. 2.20 The number of electrons with kinetic energy larger than 401 keV as a function of atmospheric depth for 10^{15} eV vertical showers, for electric fields as indicated at several altitudes. The depth of 0 means very high up in the atmosphere and the ground level is at the depth of 1036 g/cm^2.

slant depth in step sizes of 20 g/cm^2 for vertical showers. One remarkable feature one observes is that the particle number in the shower approaches a new equilibrium value which is apparently independent of the shower history. The distance over which this readjusting happens, the adapting distance, varies with height. It equals about 20 g/cm^2 at the height of 2 km and increases with the altitude to 80 g/cm^2 at 9 km. Within our simple picture, we expect this to vary as

$$X_a = \rho c \tau \,, \tag{2.32}$$

where an appropriate averaging over particle energies should be performed. At large heights, where the shower is still young and dominated by high-energy particles we expect on the basis of the energy-loss times (see Fig. 2.7) a longer distance of the order of X_0 shortening near the shower maximum where lower energetic electrons

dominate. Near the ground at LOFAR, the atmospheric electric fields are small [78] and thus do not affect the number of particles in the air showers at ground level. Therefore, the scintillators on the ground are not influenced by the atmospheric electric fields in clouds. This is supported by Ref. [79] (Figure 7) where it is shown (in mountain-top observations) that an enhanced rate of particles is only correlated to strong fields (fields in excess of 30 kV/m) at the height of the particle detectors.

2.4 Conclusion

We have studied in detail the effects of atmospheric electric fields on the structure of extensive air showers. In particular, we have focussed on the distribution of the particles in the shower disk. The effects depend on the orientation of the field with respect to the plane of the disk. This is because in earlier work we observed that atmospheric electric fields strongly influence the radio emission from extensive air showers. The simulations showed that the intensity of the radiation is almost independent of the strength of the electric field parallel to the shower direction. We also observed a peculiar dependence of the intensity on the strength of the field perpendicular to the shower. This picture is supported by air-shower Monte Carlo simulations using the CORSIKA code.

In order to understand these dependencies we have performed Monte Carlo simulations of the dynamics of the electrons using the CORSIKA code. To understand the power as has been observed at LOFAR the number of particles and their drift velocities in a layer of about 3 meters (half the wavelength) behind the shower front is critical. The Monte Carlo simulations indicate a non-trivial dependence on the strength of the applied electric field.

To gain some more insight, we have developed a simple picture where electrons are created at the shower front, move under the dynamics of the applied electric field, and disappear from the calculation after their energy loss exceeds a certain value. Under the influence of an accelerating electric field, the energy-loss time of electrons increases which increases their numbers. However, at longer times after they have been created, they will be at increasingly large distances behind the shower front and have moved outside the coherence region. The effect of an electric field perpendicular to the shower direction is more difficult to visualize, since there are two counteracting

effects to consider. A perpendicular field will accelerate electrons in the transverse direction and thus have the effect of increasing the current, though the total number of electrons hardly increases. Since particles move relativistically an increased transverse velocity will result in a decrease of the longitudinal velocity, since the total velocity cannot exceed the light velocity. As a result, for sufficiently large strengths of the transverse electric field, they will trail further than the coherence length behind the shower front and thus not contribute to radio emission at the observed frequencies. The balance between these two effects results in an initial increase of the emitted intensity proportional to the applied field followed by a regime where the intensity is roughly constant when the field exceeds a critical value of around 50 kV/m at the altitude of 5.7 km.

In order to increase the sensitivity of the measurements to atmospheric electric fields, it is shown that the deployment of antennas operating in the frequency window $2-9$ MHz would be beneficial. This frequency interval is not subject to the Galactic background because the ionosphere is not transparent at this frequency range. The precision of the electric field determination could also be increased by reducing the energy threshold of the measurement by decreasing the trigger threshold since this allows us to observe more air showers and thus improve the sampling. Such a study would not only deepen our understanding of the influence of atmospheric electric fields on air showers and their radio emission; it would also provide a powerful tool to study the electric fields in thunderclouds. The latter would be important to resolve the issue of lightning initiation [80, 41, 81].

Appendix 2.A CORSIKA

In the CORSIKA simulations, we use the high-energy hadronic interaction model QGSJET-II [82] and for the low-energy interactions we use FLUKA [83]. Atmospheric electric fields are implemented by turning on the EFIELD [74] option in CORSIKA. The geomagnetic field put into the simulations is the geomagnetic field at LOFAR. The “thinning" option with optimized weight limitation [84] is also used with a factor of 10^{-6} to keep the computing times at a reasonable level. We have simulated four kinds of iron showers: vertical showers of 10^{15} eV, 10^{16} eV, and 10^{17} eV and inclined showers of 10^{16} eV with a zenith angle of 30 degrees. Of partic-

ular relevance for radio emission is $X_{\max}$ which is also subject to shower-to-shower fluctuations. To limit this effect, simulations are selected where $X_{\max}$ differs by not more than 30 g/cm^2.

Chapter 3

Probing atmospheric electric fields in thunderstorms through radio emission from cosmic-ray induced air showers

P. Schellart, **T. N. G. Trinh**, et al.
Physical Review Letters 114, 165001 (2015)

Abstract

We present measurements of radio emission from cosmic-ray air showers that took place during thunderstorms. The intensity and polarization patterns of these air showers are radically different from those measured during fair-weather conditions. Using a simple two-layer model for the atmospheric electric field, these patterns can be well reproduced by state-of-the-art simulation codes. This in turn provides a novel way to study atmospheric electric fields.

One of the important open questions in atmospheric physics concerns the physical mechanism that initiates lightning in thunderclouds [41]. Crucial to the answer is the knowledge of atmospheric electric fields. Existing in situ measurements,

from balloons or airplanes, are limited due to the violent nature of thunderstorms. Furthermore, they inherently measure only the field in a small fraction of the cloud. Here, we present a new method to probe atmospheric electric fields through their influence on the pattern of polarized radio emission emitted by cosmic-ray induced extensive air showers.

The main mechanism for driving radio-wave emission from air showers is that the relativistic electrons and positrons in the electromagnetic part of the shower are accelerated in opposite directions by the Lorentz force exerted by the Earth's magnetic field. This produces a short, nanosecond timescale, coherent pulse of radio emission mostly at megahertz frequencies. The emission generated by this geomagnetic mechanism is unidirectionally polarized in the $\hat{e}_{\vec{v}\times\vec{B}}$ direction. Here, $\vec{v}$ is the propagation velocity vector of the shower and $\vec{B}$ represents the Earth's magnetic field [25, 85, 17, 20].

A secondary emission mechanism, contributing between $\sim 3-20\%$ to the signal amplitude depending on distance to the shower axis and the arrival direction of the shower [60, 37], results from a negative charge excess in the shower front. This consists of electrons knocked out of air molecules by the air shower. This also produces a short radio pulse but now polarized radially with respect to the shower symmetry axis [24].

The emission from both processes is strongly beamed in the forward direction, due to the relativistic velocities of the particles. Additionally, the non unity refractive index of the air causes relativistic time-compression effects leading to enhanced emission from parts of the shower seen at the Cherenkov angle [27, 86]. Interference between the differently polarized emission from both components leads to a complex and highly asymmetric *intensity pattern* [87]. In contrast, time compression effects do not alter the direction of the polarization vector of the emission. The *polarization pattern* of the radio emission thus points predominantly in the $\hat{e}_{\vec{v}\times\vec{B}}$ direction with a minor radial deviation. Strong atmospheric electric fields will influence the motions of the electrons and positrons in air showers. This is expected to be visible in the polarization patterns of the recorded emission [74]. Therefore, we analyze air showers recorded during thunderstorms.

Data for this analysis were recorded with the low-band, $10-90$ MHz, dual-polarized crossed dipole antennas located in the inner, $\sim$2 km radius, core of the

LOFAR radio telescope [23]. These antennas are grouped into circular stations which act as dishes for standard interferometric astronomical observations. For the purpose of air-shower measurements, all antennas are equipped with ring buffers that can store up to 5 s of raw voltage data sampled every 5 ns. A dedicated scintillator array, LORA, is located at the center of LOFAR to provide an independent trigger whenever an air shower with an estimated primary energy of $\geq 2 \cdot 10^{16}$ eV is detected [88]. When a trigger is received, 2 ms of raw voltage data around the trigger time are stored for every active antenna.

These data are processed in an offline analysis [36] from which a number of physical parameters are extracted and stored. These include the estimated energy of the air shower (as reconstructed from the particle detector data), the arrival direction of the air shower (as reconstructed from the arrival times of the radio pulses in all antennas), and for each antenna polarization information in the form of the Stokes parameters: I (intensity), Q, U and V. The orientation of the polarization vector is reconstructed from Stokes Q and U [37].

Over the period between June 2011 and September 2014, LOFAR has recorded a total of 762 air showers. The complex intensity pattern on the ground of almost all measured showers can be well reproduced by state-of-the-art air-shower simulation codes [61]. These codes augment well tested Monte Carlo air-shower simulations with radio emission calculated from first principles at the microscopic level [34, 26]. In this analysis we use the CoREAS plugin of CORSIKA [11] with QGSJETII [82] and FLUKA [83] as the hadronic interaction models. It was found previously that the exact shape of the pattern depends on the atmospheric depth of shower maximum, $X_{\max}$, and that the absolute field strength scales with the energy of the primary particle.

The radio footprints of 58 of the 762 air showers are very different from those predicted by simulations. Of these, 27 air showers have a measured signal-to-noise ratio below ten in amplitude — too low to get a reliable reconstruction. The polarization patterns of the other 31 showers differ significantly from those of 'normal' fair-weather air showers. This can be seen in the middle and bottom panels of Fig. 3.1 where the polarization direction is clearly coherent (i.e. non random) over all antennas but no longer in the expected $\hat{e}_{\vec{v}\times\vec{B}}$ direction. In addition, the intensity pattern of some of these showers shows a ring structure centered at the shower axis. This ring

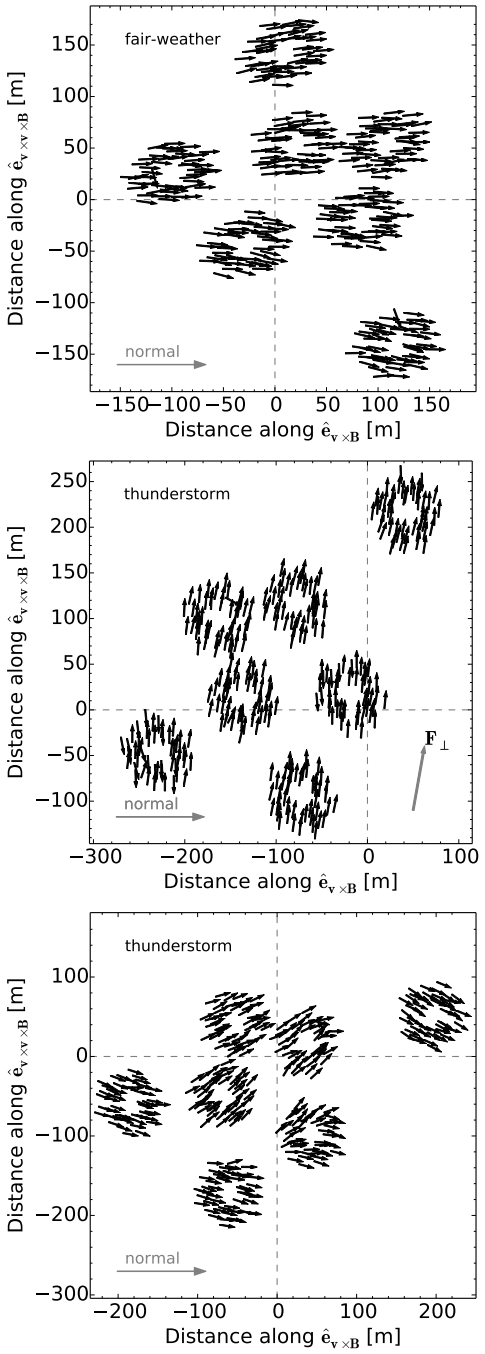

Fig. 3.1 Reconstructed polarization in the shower plane for three measured air showers.

pattern cannot be fitted by 'normal' fair-weather simulations that all show a bean shaped pattern at low $10-90$ MHz frequencies [61, 35]. Twenty of these showers occur within two hours of lightning strikes recorded within $\sim$150 km distance from LOFAR by the Royal Dutch Meteorological Institute (KNMI). Given the similarity of the polarization patterns of the remaining showers where no lightning strikes were measured, it is plausible that at these times the atmospheric electric field was also strong albeit not strong enough to initiate lightning. An electric field meter has since been installed at LOFAR that will provide independent verification for future measurements.

For the shower in the middle panel of Fig. 3.1, recorded during thunderstorm conditions, the pattern is uni-directional for the entire footprint. A second more complicated type is depicted in the bottom panel. Here the pattern is more 'wavy'. The analysis presented here focusses on an air shower of the first type where also a strong signal is measured by the LORA particle detectors.

We propose that the influence of atmospheric electric fields on air-shower radio emission can be understood in the following way.

The electric field, in the region of the cloud traversed by the air shower, can be decomposed into components perpendicular, $\vec{E}_\perp$, and parallel, $\vec{E}_\parallel$, to the shower symmetry axis. The perpendicular component of the field will not affect the number of particles but instead changes the net transverse force acting on the particles

$$\vec{F} = q(\vec{E}_\perp + \vec{v} \times \vec{B}). \tag{3.1}$$

This changes both the magnitude and the polarization of the radiation which follows $\vec{F}$. Depending on the polarity of the parallel component of the electric field either the electrons or the positrons get accelerated and as a consequence their number increases. These extra particles are lower in energy than the shower particles and lag behind the shower front. Thus, the emission produced by them is no longer coherent for frequencies above 10 MHz and does not significantly increase the observed emission intensity. For this reason the perpendicular component of the electric field determines the measured intensity and polarization direction.

In order to test this hypothesis, atmospheric electric fields were inserted into CoREAS air-shower simulations. By comparing fields acting purely parallel and

purely perpendicular to the shower axis it was found that the effect of $\vec{E}_\perp$ on the radio emission is much stronger and will dominate in most shower configurations where both components are present.

Having understood the basic effects of atmospheric electric fields on air-shower radio emission we proceed with a full reconstruction of LOFAR measurements. We follow the method developed in Ref. [61] to fit CoREAS simulations to LOFAR measurements. An atmospheric electric field is inserted into the simulations with the perpendicular component chosen such that the net force is in the measured average polarization direction (as indicated in the middle panel of Fig. 3.1). The parallel component is set to zero since its influence on the received radiation intensity and polarization pattern is negligible.

The simplest electric field configuration that can reproduce the main features both in the measured intensity and polarization patterns is composed of two electric field layers. The first layer starts at a height h_1 above the ground and extends down to a height h_2 at which the direction of the net force changes by 180° and the field strength decreases. Two layers are needed because with one layer the ring structure seen in the measurements is not reproducible.

In Fig. 3.2 the reconstruction is shown for the air shower for which the polarization pattern is depicted in the middle panel of Fig. 3.1. The reconstruction is optimal for $h_1 = 8$ km, $h_2 = 2.9$ km and $|\vec{E}_2|/|\vec{E}_1| = 0.53$. For these values $\chi^2/\text{ndf} = 3.2$ for a joint fit to both the radio and particle data. A perfect fit of $\chi^2/\text{ndf} \approx 1$, as is often found for fair-weather showers, is likely not attainable with a simplified electric field model. However, all the main features of the intensity and polarization pattern (namely the overall polarization direction and ring structure) are already correctly reproduced.

The fit quality is sensitive to changes in the relative field strength and h_2 as well as X_{max}. This can be seen in Fig. 3.3, where each parameter is varied while keeping the others at their optimum values. This fixing is not possible for X_{max} in CORSIKA, therefore simulations were selected where X_{max} varied by no more than 20 g/cm^2. The fit quality reaches its optimum value for $h_1 = 8$ km and is not sensitive to a further increase. This is expected because above this altitude the air shower is not yet fully developed and there are relatively few particles contributing to the emission.

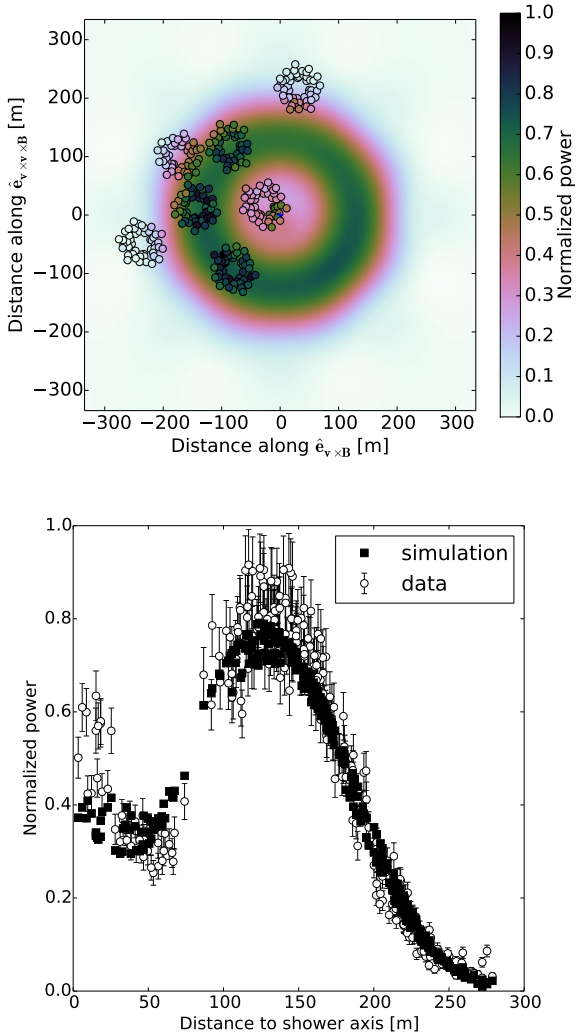

Fig. 3.2 Intensity pattern for an air shower measured during a thunderstorm in the shower plane (circles, top panel) and as a function of distance to the shower axis (circles, bottom panel). The best fitting CoREAS simulation is shown in the background and as squares, respectively. Where the colors of the small circles match the background, a good fit is achieved.

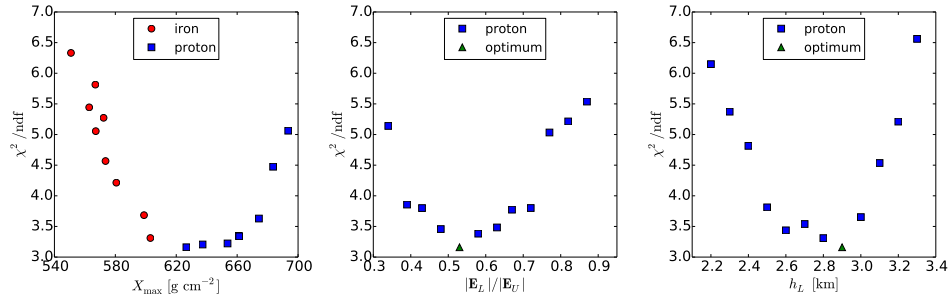

Fig. 3.3 Sensitivity of the fit quality to variations in the atmospheric depth of shower maximum $X_{\max}$ (left panel), the relative field strength (middle panel) and the field reversal altitude h_2 (right panel). The optimal proton simulation is the same for all plots.

The energy of the air shower is derived from the particle density on the ground, as measured by LORA, combined with the information on $X_{\max}$, as determined from the radio fit. For fair-weather air showers the measured radio intensity is related to the simulated values through a constant scaling factor [61] given the energy of the primary. For the air shower measured during thunderstorm conditions the predicted radio intensity lies below the measured value. However, the absolute electric field strength also influences the radio intensity. The intensity increases until the atmospheric electric field strength reaches $|\vec{E}_2| \geq 50$ kV/m. When the field strength is increased further the radio intensity stays constant. This saturation of the radio intensity appears to be related to the coherent nature of the emission but is still under investigation.

Measuring radio emission from cosmic-ray extensive air showers during thunderstorm conditions thus provides a unique new tool to probe the atmospheric electric fields present in thunderclouds. Unlimited by violent wind conditions and sensitive to a large fraction of the cloud this technique may help answer the long standing question "how is lighting initiated in thunderclouds?" It has been suggested in Ref. [89] that cosmic-ray induced air showers in combination with runaway breakdown may initiate lightning. If this is indeed true then LOFAR with its combination of particle detectors and radio antennas is well positioned to measure it.

Chapter 4

Thunderstorm electric fields probed by extensive air showers through their polarized radio emission

T. N. G. Trinh, O. Scholten, et al.
Physical Review D 95, 083004 (2017)

Abstract

We observe a large fraction of circular polarization in radio emission from extensive air showers recorded during thunderstorms, much higher than in the emission from air showers measured during fair-weather circumstances. We show that the circular polarization of the air showers measured during thunderstorms can be explained by the change in the direction of the transverse current as a function of altitude induced by atmospheric electric fields. Thus by using the full set of Stokes parameters for these events, we obtain a good characterization of the electric fields in thunderclouds. We also measure a large horizontal component of the electric fields in the two events that we have analysed.

4.1 Introduction

Lightning initiation [80] and propagation [41] are driven by the electric fields in a thunderstorm. However, performing measurements of these fields is very challenging due to the violent conditions in thunderclouds. A nonintrusive method to probe thunderstorm electric fields is through a measurement of radio emission from extensive air showers during thunderstorms [71].

When a high-energy cosmic ray strikes the Earth's atmosphere, it generates many secondary particles, a so-called extensive air shower. The dominant contribution to the radio emission from air showers during fair weather (*fair-weather events*) is driven by the geomagnetic field [25, 31]. Electrons and positrons are deflected in opposite directions due to the Lorentz force, which results in a current perpendicular to the shower axis. As the shower develops, this current varies with altitude, thereby producing radio emission. This radiation is linearly polarized in the $\hat{e}_{\mathbf{v}\times\mathbf{B}}$ direction, where $\mathbf{v}$ is the velocity of the shower front, $\mathbf{B}$ is the geomagnetic field, and $\hat{e}$ denotes an unit vector. In addition, as the shower propagates, a negative charge excess builds up in the shower front due to the knock-out of electrons from air molecules by the shower particles. The variation of this charge excess gives rise to a secondary contribution to the emission [24, 64]. The charge-excess emission is also linearly polarized, but radially with respect to the shower axis. For fair-weather events, we observe a small fraction of circular polarization due to the fact that the time structures of the radio pulses emitted from the charge-excess component and those from the transverse-current component are different [58]. Since the charge-excess pulses are delayed with respect to the transverse-current pulses and they are polarized in different directions, the polarization of the total pulse rotates from one direction to the other. In our analysis, this is seen as circular polarization where the magnitude and handedness depend on the distance and the azimuth position of the observer with respect to the shower axis.

As shown in [71], due to the influences of atmospheric electric fields, intensity and linear-polarization footprints of the showers observed during thunderstorms (*thunderstorm events*) are different from those of fair-weather events. In this paper we show that thunderstorm events have a larger circular polarization component near the shower axis than fair-weather events. We demonstrate quantitatively that this

can be explained as being due to the variation of the atmospheric electric field with altitude. The electric field changes the direction of the transverse current and thus changes the polarization direction of radio emission. The signals from the different layers are emitted in sequence when the air-shower front, progressing with essentially the light velocity, c, passes through. The emitted radio signals travel with a lower velocity than the shower front, c/n, where n is the index of refraction. Thus, near the shower axis, the pulses from the upper layers arrive with a delay with respect to the pulses from the lower layers resulting in a change of the polarization angle over the duration of the pulse, which is seen as circular polarization in the data. Therefore, the usage of the circular polarization measurements puts strong additional constraints on the structure of the atmospheric electric fields on top of the information obtained by using only the radio intensity. Since the circular polarization is due to a reorientation of the transverse current in the shower front the circular polarization does not depend on the azimuthal orientation of the antenna with respect to the shower axis, unlike is the case for the circular polarization of fair-weather events.

In this work, we present data on circular polarization seen in the radio emission of a large number of thunderstorm events close to the shower axis as measured with the Low-Frequency Array (LOFAR) radio telescope array, see Sec. 4.2. In Sec. 4.3, we present a toy model to explain the cause of circular polarization of air showers measured during thunderstorms. Two reconstructed thunderstorm events are presented in Sec. 4.4 to show that circular polarization is essential to obtain additional information about the atmospheric electric fields. Conclusions are given in Sec. 4.5.

4.2 LOFAR and data analysis

Data for the present analysis were recorded with the Low-Band Antennas (LBAs) in the core of the LOFAR radio telecope [23]. Each LBA consists of two dipoles and records in the frequency range of $10-90$ MHz. These antennas are grouped into circular stations. The stations are positioned with increasing density towards the center of LOFAR. The highest density is at the core where six such stations are located in a $\sim$320 m diameter region, the so-called 'Superterp'. For the purpose of air shower measurements, these antennas are equipped with ring buffers that can store the raw voltage traces sampled every 5 ns, up to 5 s. A trigger is obtained from a

particle detector array, Lofar Radboud Air Shower Array (LORA), from air showers with a primary energy in excess of 2×10^{16} eV [88].

The data are processed in an off-line analysis [36]. The arrival direction of the air shower is reconstructed based on the arrival times of the radio signals in all antennas. The primary energy of the air shower is estimated by using the particle detector data. The radio signal containing the pulse is received by an antenna where the signal amplitude S_i is determined at 5 ns time intervals, i.e., sampled at 200 MS/s, where the sample number is denoted by i. For each antenna, the Stokes parameters, I, Q, U and V, are expressed as

$$\begin{aligned} I &= \frac{1}{n}\sum_{i=0}^{n-1}\left(\left|\varepsilon_{i,\mathbf{v}\times\mathbf{B}}\right|^2+\left|\varepsilon_{i,\mathbf{v}\times(\mathbf{v}\times\mathbf{B})}\right|^2\right), \\ Q &= \frac{1}{n}\sum_{i=0}^{n-1}\left(\left|\varepsilon_{i,\mathbf{v}\times\mathbf{B}}\right|^2-\left|\varepsilon_{i,\mathbf{v}\times(\mathbf{v}\times\mathbf{B})}\right|^2\right), \\ U+iV &= \frac{2}{n}\sum_{i=0}^{n-1}\left(\varepsilon_{i,\mathbf{v}\times\mathbf{B}}\varepsilon^*_{i,\mathbf{v}\times(\mathbf{v}\times\mathbf{B})}\right), \end{aligned} \tag{4.1}$$

as derived in Ref. [37]. $\varepsilon_i = S_i + i\hat{S}_i$ are the complex signal voltages, where $\hat{S}_i$ is sample i of the Hilbert transform of S. The summation is performed over n = 5 samples, centered around the peak of the pulse. Stokes I is the intensity of the radio emission. Stokes Q and U are used to derive the linear-polarization angle

$$\psi = \frac{1}{2}\tan^{-1}\left(\frac{U}{Q}\right), \tag{4.2}$$

and V/I represents the amount of circular polarization.

During the period between June 2011 and January 2015, there were 118 fair-weather events [90] and 20 thunderstorm events [71] with radio signals detected in at least four LBA stations. For comparison, the circular polarization for 20 thunderstorm events and for six fair-weather events is shown in Fig. 4.1 and Fig. 4.2, respectively. The circular polarization for fair-weather events is very small near the shower axis and increases with distance [58]. Therefore, in order to show the dependence on azimuth angle, φ, we selected those fair-weather events that have data of at least 4 LBA stations beyond 150 m from the shower axis and where

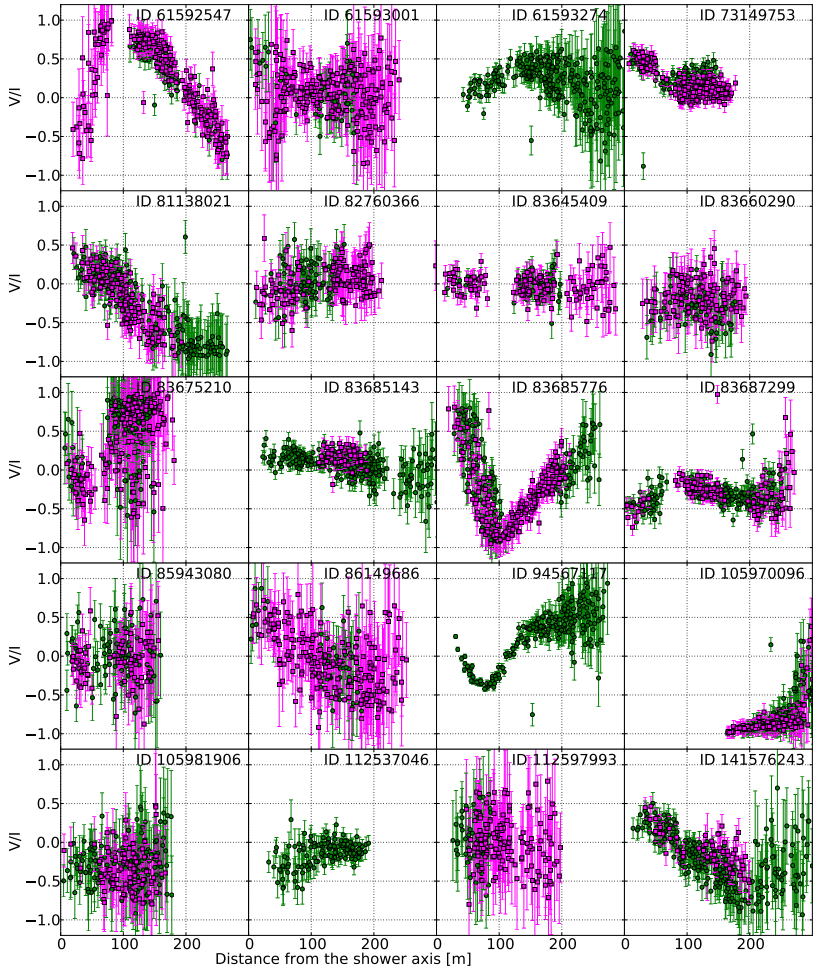

Fig. 4.1 The circular polarization for thunderstorm events as a function of distance from the shower axis. Green circles represent the circular polarization at the antennas having an azimuthal position $\varphi = 0^\circ - 180^\circ$ and magenta squares show those for $\varphi = 180^\circ - 360^\circ$, where $\varphi = 0$ lies on the positive $\hat{e}_{\mathbf{v}\times\mathbf{B}}$ axis. The ID numbers are used to label the air showers.

the uncertainties in the amount of circular polarization is less than 0.2. As can be seen from Fig. 4.1 and Fig. 4.2, there are significant differences between the circular polarization for the thunderstorm events and that for the fair-weather events. First, the circular polarization for the thunderstorm events does not depend on the azimuthal position, φ, of the antenna while for the fair-weather events it is proportional to $\sin\varphi$. Secondly, the circular polarization for some thunderstorm events changes sign at some distances while the dependence of the circular polarization on distance is almost the same for all fair-weather events as mentioned above. In Fig. 4.1, it can be seen that there are some thunderstorm events having a very small amount of circular polarization. These events are distinguished from fair-weather events by the linear polarization that has been discussed in Ref. [71]. Thirdly, the circular polarization for all fair-weather events is small near the shower axis while it varies from event to event for thunderstorm events.

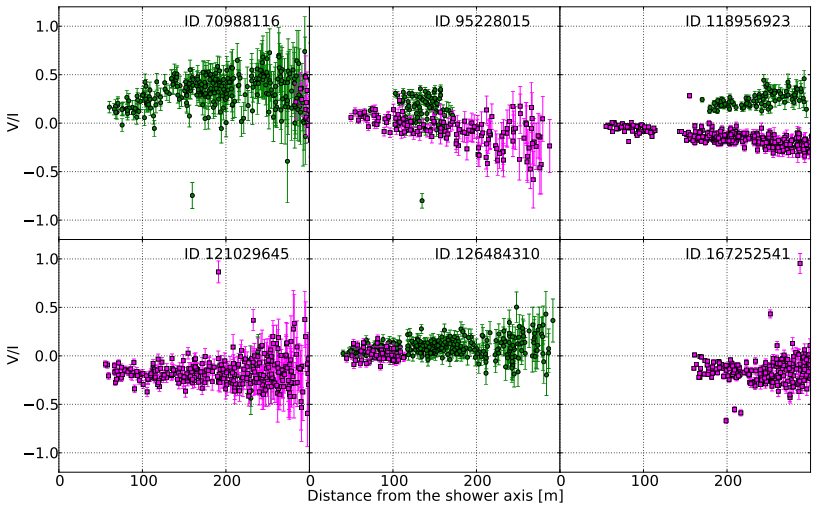

Fig. 4.2 The circular polarization for fair-weather events as a function of distance from the shower axis. Green circles represent the circular polarization at the antennas having an azimuthal position $\varphi = 0^\circ - 180^\circ$ and magenta squares show those for $\varphi = 180^\circ - 360^\circ$, where $\varphi = 0$ lies on the positive $\hat{e}_{\mathbf{v}\times\mathbf{B}}$ axis. The ID numbers are used to label the air showers.

This difference is also shown in Fig. 4.3, where the amount of circular polarization ($|V|/I$) within a 30 m radius of the shower axis is given for 884 antennas recording fair-weather data and 183 antennas taking thunderstorm data. We choose the radius of 30 meters to concentrate on the near-axis region while also keeping an area large enough to contain a sufficient number of antennas. The uncertainties indicated in Fig. 4.3 are determined from a Monte Carlo procedure. For 500 trials per antenna the Stokes parameters Q_t, U_t and V_t are chosen randomly from a Gaussian distribution where the mean and the standard deviation of the distribution correspond to the actual measurement. The Stokes I_t of each trial is calculated by using $I_t^2 = (Q_t^2 + U_t^2 + V_t^2) + W^2$ where W is calculated from the actual Stokes parameters measured by the antenna, $W^2 = I^2 - \left(Q^2 + U^2 + V^2\right)$. The spread (standard deviation) of the determined distribution of $|V_t|/I_t$ gives the uncertainty. Fig. 4.3 shows that the amount of circular polarization near the shower axis is consistently small for fair-weather events, while a large spread is seen for thunderstorm events. In Ref. [58] it was shown that for the fair-weather events the measured circular polarization is well understood. The physics of the measured circular polarization of the thunderstorm events is explained in detail in the following section.

4.3 Modeling

During thunderstorms the emission of radio waves from air showers is affected by atmospheric electric fields [68, 69, 71]. The atmospheric electric field can be decomposed into two components $\mathbf{E}_\perp$ and $\mathbf{E}_\parallel$, which are perpendicular and parallel to the shower axis, respectively. $\mathbf{E}_\parallel$ increases the number of either electrons or positrons, depending on its orientation, and decreases the other [71, 91]. Since the field compensates the energy loss of low-energy electrons, they 'live' longer and can thus trail further behind the shower front. As a result, the radiation from these particles does not add coherently in the frequency range $30-80$ MHz of the LOFAR LBAs.. The transverse component of the field $\mathbf{E}_\perp$ does not change the number of electrons and positrons, but changes the net transverse force acting on the particles [71, 91]

$$\vec{F}_\perp = q(\vec{E}_\perp + \vec{v} \times \vec{B}). \tag{4.3}$$

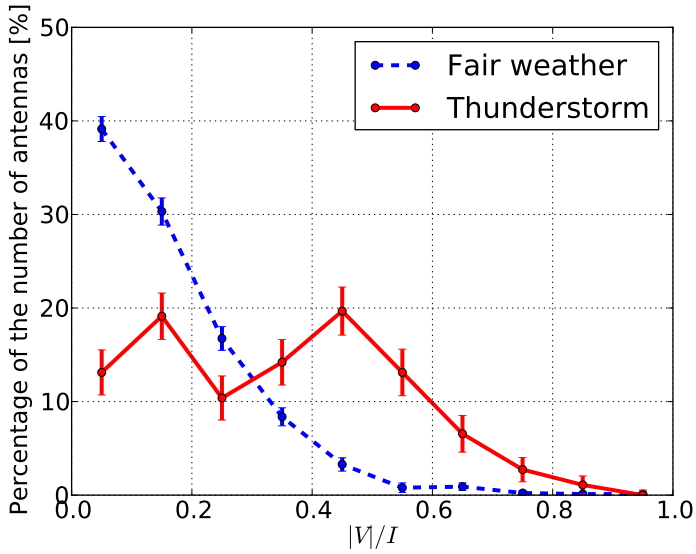

Fig. 4.3 Distribution of the amount of circular polarization in the area within the radius 30 m from the core for showers measured during fair weather and thunderstorms.

Hence, the magnitude and the direction of the induced transverse current change according to the net force $\mathbf{F}_\perp$. Since for the presented data the influence of the transverse component $\mathbf{E}_\perp$ on the radio emission dominates, the parallel component $\mathbf{E}_\parallel$ is set to zero in this work.

The transverse electric field changes the direction of the transverse current, so it also modifies the polarization of the transverse-current radiation. In thunderclouds, not only the magnitude but also the orientation of electric fields changes with altitude [53]. This causes a change of the transverse current in the thunderclouds and thus the linear polarization changes with time. As explained in the introduction, this results in a changing linear polarization angle over the duration of the pulse giving rise to a large value for V (see Eq. (5.1)), the component of circular polarization of the pulse.

We use a toy model to show the physics of large circular polarization of the pulses in some of the thunderstorm events. We consider the geometry given in Fig. 4.4 as an example. A vertical air shower passes through two layers where the electric field in each is constant. The fields are such that the net forces are perpendicular to each

other and make an angle φ with $\hat{e}_{\mathbf{v}\times\mathbf{B}}$ as shown in Fig. 4.4. The induced current in the shower front is proportional to the number of particles in the shower multiplied by the net force acting on them. The induced currents thus have orthogonal directions in the two layers where the peak of the current occurs at height h_m, corresponding to $X_{\max}$ of the shower, defined as the atmospheric (slant) depth where the number of air-shower particles reaches a maximum. For this case we consider the pulses emitted with a central frequency ω when the shower passes through each layer

$$\begin{aligned} \varepsilon_a &= A_a e^{i(\omega t+\eta_a)}\,, \\ \varepsilon_b &= A_b e^{i(\omega t+\eta_b)}\,, \end{aligned} \tag{4.4}$$

where $\eta = \eta_a - \eta_b = \omega\Delta t$ is the phase difference corresponding to an arrival-time difference Δt between the two pulses for an observer. In thunderstorms, the transverse current is generally enhanced by the atmospheric electric field, so its radiation is much larger than the charge-excess emission and thus we ignore the charge-excess contribution. Therefore, neither ε_a, ε_b nor η depends on the azimuth angle of the antenna position with respect to the shower axis. Since the transverse currents in the two layers are perpendicular to each their pulses are polarized in two perpendicular orientations on the ground. These pulses can be expressed as

$$\begin{aligned} \varepsilon_{\mathbf{v}\times\mathbf{B}} &= A_a e^{i(\omega t+\eta_a)}\cos\varphi - A_b e^{i(\omega t+\eta_b)}\sin\varphi\,, \\ \varepsilon_{\mathbf{v}\times(\mathbf{v}\times\mathbf{B})} &= A_a e^{i(\omega t+\eta_a)}\sin\varphi + A_b e^{i(\omega t+\eta_b)}\cos\varphi\,. \end{aligned} \tag{4.5}$$

Substituting these into Eq. (5.1) we obtain the Stokes parameters

$$\begin{aligned} I &= A_a^2 + A_b^2\,, \\ Q &= \left(A_a^2 - A_b^2\right)\cos 2\varphi - 2A_aA_b\sin 2\varphi\cos\eta\,, \\ U &= \left(A_a^2 - A_b^2\right)\sin 2\varphi + 2A_aA_b\cos 2\varphi\cos\eta\,, \\ V &= 2A_aA_b\sin\eta\,. \end{aligned} \tag{4.6}$$

For the special case when $\varphi = 0$, i.e. the net force in the upper layer is along $\hat{e}_{\mathbf{v}\times\mathbf{B}}$ and the one in the lower layer is along $\hat{e}_{\mathbf{v}\times(\mathbf{v}\times\mathbf{B})}$ (see Fig. 4.4), the phase shift

can be derived from the Stokes V and U parameters

$$\eta_{\varphi=0} = \arctan\left(\frac{V}{U}\right) . \tag{4.7}$$

We will show for this special case how η depends on the distance d from the shower

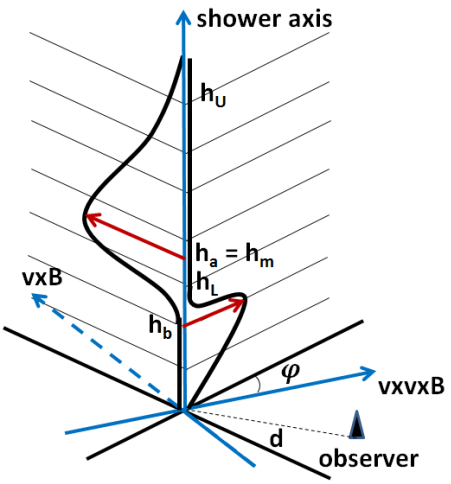

Fig. 4.4 The geometry used in the calculation and a typical current profile of a shower passing through a two-layered electric field where the fields in the two layers are oriented perpendicular to each other. The two solid red arrows indicate the net forces acting on air-shower particles.

axis for a fixed frequency ω. To simplify the calculation, we assume that at the height of h_a the current points in $\hat{e}_{\mathbf{v}\times\mathbf{B}}$ and emits radiation. After that the shower propagates down with the velocity c, and the current rotates to $\hat{e}_{\mathbf{v}\times(\mathbf{v}\times\mathbf{B})}$ at the height of $h_b = h_a - \Delta h$ and radiates another signal. The pulses emitted at different heights move with the reduced velocity $v = c/n$ and thus arrive with a time delay due to the fact that index of refraction n is larger than unity. The signals with a frequency ω which an observer at a distance d from the origin receives (since $\varphi = 0$) are

$$\begin{aligned} \varepsilon_{\mathbf{v}\times\mathbf{B}} &= A_a e^{i\omega(t-R_a/v)} , \\ \varepsilon_{\mathbf{v}\times(\mathbf{v}\times\mathbf{B})} &= A_b e^{i\omega(t-\Delta h/c-R_b/v)} , \end{aligned} \tag{4.8}$$

where $R_a = \sqrt{h_a^2 + d^2}$ and $R_b = \sqrt{h_b^2 + d^2}$ are the distances from the observer to the emission points and v is the velocity of the signals. $\Delta h/c$ accounts for the later arrival of the current at h_b. The phase shift of these two signals can be derived from Eq. (4.7)

$$\tilde{\eta} = \frac{\omega}{c}\left[n\left(\sqrt{h_b^2 + d^2} - \sqrt{h_a^2 + d^2}\right) + \Delta h\right]. \tag{4.9}$$

The phase shift $\tilde{\eta}$ is positive, which means that the signal radiated at h_a arrives earlier than the one at h_b. For $\tilde{\eta} = 0$, the two signals arrive at the observer at the same time. Note that Eq. (4.9) can only be used in the case where the two emission components are perpendicular to each other and one of the components is along $\hat{e}_{\mathbf{v}\times\mathbf{B}}$.

For comparison with the analytic calculation, we simulated three vertical showers with CoREAS [34] that included two-layered electric fields with the boundaries between electric fields at different altitudes h_L. The electric field EFIELD option [74] was implemented in CORSIKA [11]. The electric fields in the two layers are such that the net force in the upper layer points in $\hat{e}_{\mathbf{v}\times\mathbf{B}}$ and the one in the lower layer points in $\hat{e}_{\mathbf{v}\times(\mathbf{v}\times\mathbf{B})}$, which introduces two perpendicular transverse currents. The upper layer, with strength $|\mathbf{E_U}|$ = 50 kV/m, starts at a height h_U = 8 km above the ground and extends down to heights of h_L = 4 km, 3 km and 2 km for each simulation. At h_L the lower layer starts and the field strength decreases to $|\mathbf{E_L}|$ = 25 kV/m. The shower maximum $X_{\max}$ = 580 g/cm^2 is the same in all three simulations, corresponding to $h_m \approx 4.6$ km, which is in the upper layer.

In order to be compared with the analytic calculation where pulses are assumed to emit a central frequency ω, the phase shift η_C from the CoREAS simulations in the narrow frequency band, $60-65$ MHz, is derived and displayed in Fig. 4.5. The phase shift $\tilde{\eta}$ derived from Eq. (4.9) is also shown in Fig. 4.5 for ω = 65 MHz. To simplify the calculation, the refractive index is kept constant at $n = 1.00015$. Note that the heights h_a and h_b in Eq. (4.9) are the average heights from which the dominant intensity is emitted for the two polarization directions and are thus not equal to h_U and h_L. In the upper layer, the maximum emission occurs at $h_a = h_m$. In the lower layer, the height h_b depends on the distance from the observer to the shower axis. At large distances, beyond ~ 50 m, the maximum emission arrives from $h_b' = h_L - X_a/\rho$, where the air density ρ is approximately [53] $\rho(h) = 1.208\cdot 10^{-3}\exp(-h/8.4)$ g/cm^3 and X_a is the adapting distance varying with heights (see Fig. 20 in Ref. [91]). The

average values of h_b for the three simulations are 3.2 km, 2.53 km and 1.78 km, respectively. At the distance $d < h'_b \tan\theta = h'_b\sqrt{n^2-1}$, where θ is the opening angle corresponding to the distance d, the observer receives the dominant signal from $h'_b = d/\sqrt{n^2-1}$. As seen in Fig. 4.5, it is the distance at which all three lines coincide. At large distances, $\tilde{\eta}$ is positive which means the observer receives the signal radiated at h_a first and the one at h_b later. At about 50 m, the two signals arrive at the observer at the same time. It can be seen from Fig. 4.5 that the calculation agrees quite well with the simulations, which demonstrates that the source of the circular polarization is well understood. However, for more general geometries of atmospheric electric fields, the layer heights, field strengths and field orientations can only be found through a numerical optimization procedure.

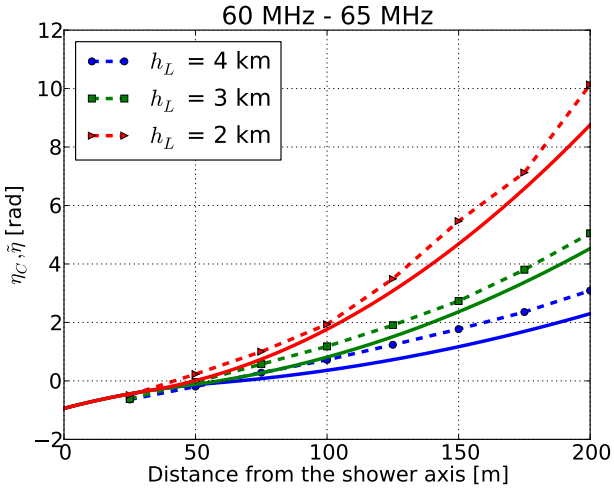

Fig. 4.5 The phase shift η as a function of distance from the shower axis. Dotted curve: phase shift η_C from CoREAS results. Solid curves: phase shift $\tilde{\eta}$ from an analytic calculation.

4.4 Probing the structures of atmospheric electric fields

As discussed in the previous section, the circular polarization in thunderstorm events is caused by the variation in the orientation of the atmospheric electric fields. There-

fore, using the full set of Stokes parameters, i.e. the combination of intensity, linear polarization, and circular polarization, allows a more accurate determination of the electric fields in the cloud layers where the air shower passes through than when using only intensity information as in Ref. [71]. To provide more insight into this assertion, we discuss in detail the reconstruction of two thunderstorm events which are called in this work event No.1 and event No.2.

Fitting thunderstorm events is challenging since the electric fields contain many parameters. Another problem is that since CoREAS is a Monte Carlo simulation, two calculations with similar electric fields can give considerably different results due to shower-to-shower fluctuations even when using the same random seed. Therefore, to determine the electric fields, we first perform a fit using a semianalytic calculation [33] of the radio footprint of air showers based on the current profile. This procedure requires much less CPU time and there are no shower-to-shower fluctuations. This allows for a standard steepest descent fitting procedure. Since this method only approximates the structure of the shower front, we use this to get close to the optimal choice after which we use CoREAS for the final calculations. In order to obtain a prediction of the two-dimensional footprints of the four Stokes parameters, we run CoREAS simulations for 160 antennas which form a star-shaped pattern with eight arms as in Ref. [61], and make an interpolation to reconstruct the full profile. The results are filtered in the frequency range of the LOFAR LBAs.

The electric field fields are labeled with indices 1, 2 and 3 where 1 is the top layer. Each layer is defined by the height h above the ground where the electric field starts and the field $\vec{E}_{\perp}$. Note that our analysis cannot determine the parallel components of the electric fields $\mathbf{E}_{\parallel}$; therefore we always work in the two-dimensional plane perpendicular to $\hat{e}_{\mathbf{v}}$. In this plane, the perpendicular components, $\mathbf{E}_{\perp}$, are expressed in two bases. 1) It can be expressed as the field strength $|\mathbf{E}_{\perp}|$ and the angle α between the net force and $\hat{e}_{\mathbf{v}\times\mathbf{B}}$, where the net force is the vectorial sum of the Lorentz force and the electric force given by the electric field. 2) It can also be decomposed into $E_{\mathbf{v}\times\mathbf{z}}$ and $E_{\mathbf{v}\times(\mathbf{v}\times\mathbf{z})}$, the components of $\mathbf{E}_{\perp}$ along $\hat{e}_{\mathbf{v}\times\mathbf{z}}$ and $\hat{e}_{\mathbf{v}\times(\mathbf{v}\times\mathbf{z})}$, respectively. Here $\hat{e}_{\mathbf{z}}$ is vertically pointing up.

The intensity footprint, the linear polarization footprint and the circular polarization footprint of thunderstorm event No.1, measured at 12:38:37 UTC, December

30^{th}, 2012, are displayed in Fig. 4.6. The fractions of Stokes parameters are shown in Fig. 4.7.

The intensity footprint (top panel of Fig. 4.6) of this event shows a bean shape which is also observed in fair-weather events. The differences are that the maximum intensity is not in the $\mathbf{v} \times \mathbf{B}$-direction as it is in fair-weather events and the linear polarization (middle panel Fig. 4.6) is not oriented mainly along $\hat{e}_{\mathbf{v}\times\mathbf{B}}$ as it is in the fair-weather events. The polarization footprint shows a 'wavy' pattern near the shower axis where the polarization is different from the one at the outer antennas. We observe a large fraction of circular polarization in this event, varying as a function of the distance from the antenna to the shower axis. This can be seen in the bottom panel of Fig. 4.6 and the right panel of Fig. 4.7. Therefore, for this event, using only the intensity footprint gives incomplete information about the atmospheric electric field. The simplest structure of the electric field which can capture the main features of this event is a three-layer field. The reconstruction is optimal for the values of the parameters given in Table 4.1. The simulation has values of $X_{\max} = 665$ g/cm^2. The primary energy of the shower is $E = 4.7 \times 10^{16}$ eV and the zenith angle is $\theta = 15.5^\circ$. Since we do not observe a ring-like intensity pattern, the emission from different layers should not interfere destructively, and thus the fields should not have opposite orientation as taken in Ref. [71]. The change in the orientation of the electric field between the second layer and the third layer, close to the ground, results in a change in the direction of the transverse current and thus gives rise to the rotation of the linear polarization as well as a large amount of circular polarization in the region close to the shower axis. Near the shower axis the radio signal is most sensitive to the later stages of the shower development, while at large distances the currents higher in the atmosphere have more weight. Thus, a much smaller circular polarization component is observed at larger distances. There are some differences between the measured and simulated Stokes parameters seen in Fig. 4.7 since the three-layered electric field is still an oversimplification of the realistic field. The reduced χ^2 for a joint fit of both the Stokes parameters and the particle data $\chi^2/\text{ndf} = 4.5$, which is large compared to $\chi^2/\text{ndf} \approx 1$ found in fair-weather showers. However, all main the features are captured.

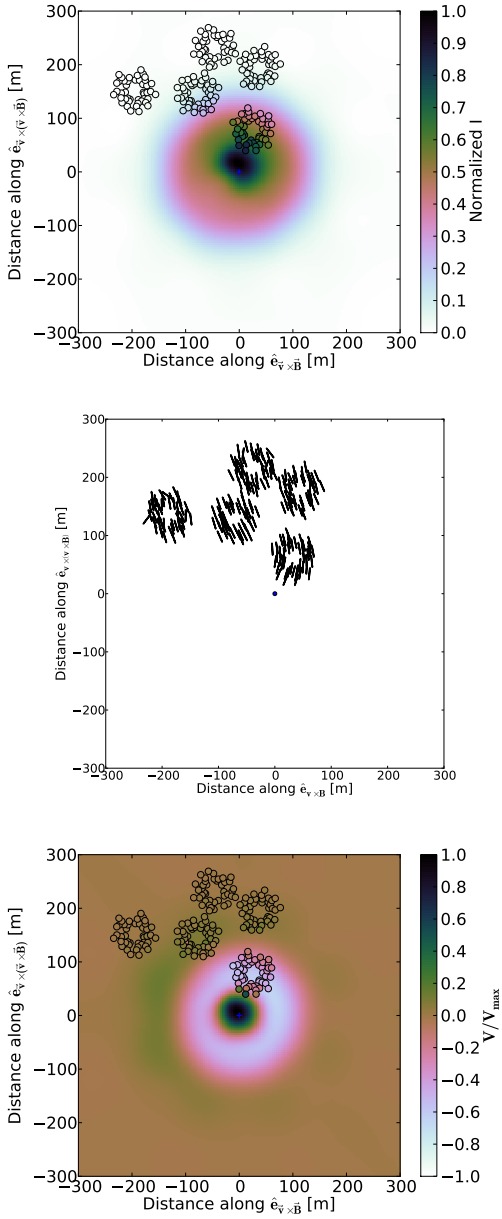

Fig. 4.6 Radio polarization footprints of the thunderstorm event No.1. Top: The intensity (Stokes *I*) footprint. Middle: Linear polarization as measured with individual LOFAR LBA (lines) in the shower plane. Bottom: The footprint of Stokes *V*, representing the circular polarization. In the top and bottom panels, the background color shows the simulated results while the coloring in the small circles represents the data.

Layer	1	2	3
Height (km)	$8-5$	$5-2$	$2-0$
$\lvert\vec{E}_{\perp}\rvert$ (kV/m)	50	15	9
α ($^{\circ}$)	98	98	8
$E_{\mathbf{v}\times\mathbf{z}}$ (kV/m)	46	13	4
$E_{\mathbf{v}\times(\mathbf{v}\times\mathbf{z})}$ (kV/m)	-22	-9	8

Table 4.1 The structure of the three-layered electric field of the thunderstorm event No.1.

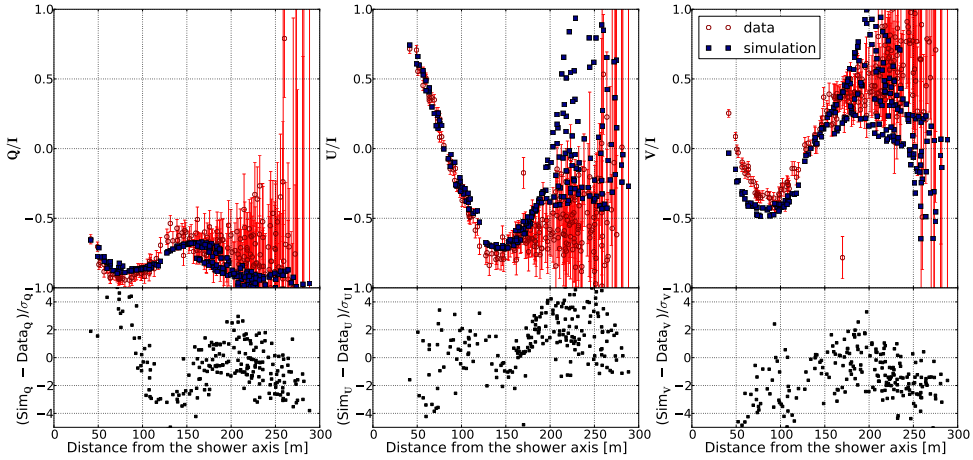

Fig. 4.7 The set of normalized Stokes parameters of the thunderstorm event No.1 as recorded with the LOFAR LBAs (open red circles) is compared to the results of the CoREAS simulation (filled blue dots). σ denotes one standard deviation error.

Fig. 4.8 shows the intensity footprint and the polarization footprint of thunderstorm event No.2, which was also presented in Ref. [71]. The fractions of Stokes parameters are shown in Fig. 4.9. This event was measured at 14:28:19 UTC, August 26^{th}, 2012. The ring-like structure in the intensity footprint (top panel of Fig. 4.8) and the overall polarization direction (middle panel of Fig. 4.8) indicate that at least a two-layered electric field is needed [71], where the electric fields are pointing in opposite directions to introduce a destructive interference between the radiation from the two layers. However, the large amount of circular polarization near the shower

axis (see the bottom panel of Fig. 4.8 and the right panel of Fig. 4.9) cannot be reproduced by such a field configuration since there is no rotation of the current. The simplest structure of an electric field which can capture the main features of this event is a three-layered field. Table. 4.2 presents the values of the electric field giving the best reconstruction of this shower. The electric fields obtained here follow the same general structure as presented in our earlier work [71]. Like in Ref. [71] the strength of the fields in the lower layer are about half the strength as in the upper layer with almost opposite orientation. However, in the present, more detailed, analysis an additional layer needed to be introduced which shows that the method used in this work gives more accurate information about the electric fields in thunderstorms. The shower maximum is $X_{\max}$ = 628 g/cm^2. The primary energy of this shower is E = 3.1×10^{16} eV and the zenith angle is $\theta = 24.8^\circ$.

There is also an almost complete reversal of the electric field from the second layer to the third layer which gives rise to the ring-like structure in the intensity footprint and keeps the linear polarization unique. The reduced χ^2 for a joint fit of both the Stokes parameters and the particle data is $\chi^2/\text{ndf} = 3.5$, which is large but reproduces all the main features.

Layer	1	2	3
Height (km)	$8-6.9$	$6.9-2.7$	$2.7-0$
$\lvert\vec{E}_\perp\rvert$ (kV/m)	50	20	18
α ($^\circ$)	-78	-104	67
$E_{\mathbf{v}\times\mathbf{z}}$ (kV/m)	-46	-12	14
$E_{\mathbf{v}\times(\mathbf{v}\times\mathbf{z})}$ (kV/m)	-16	-16	11

Table 4.2 The structure of the three-layered electric field of the thunderstorm event No.2.

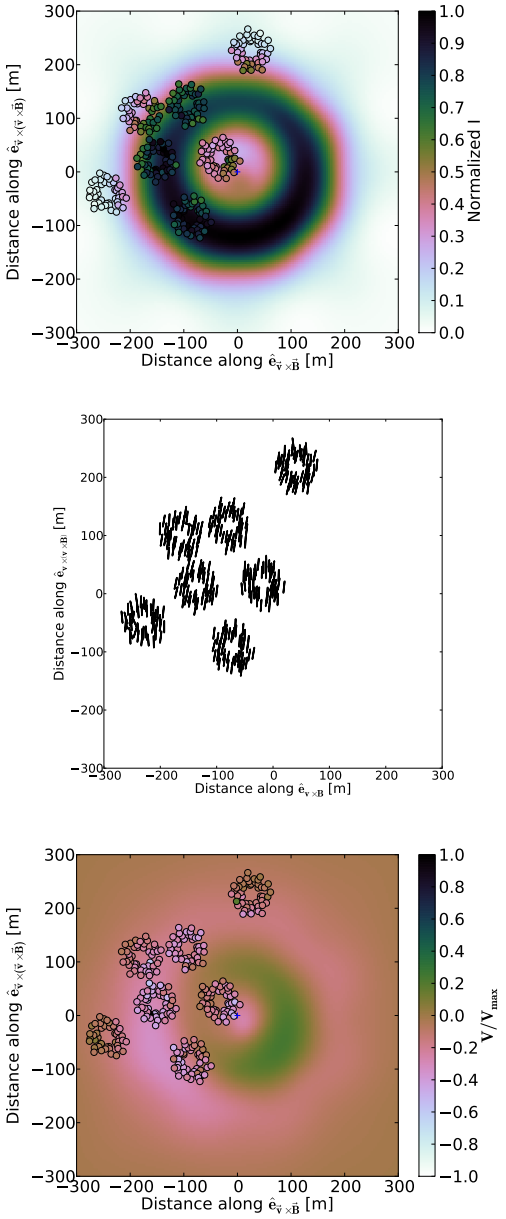

Fig. 4.8 Radio polarization footprints of the thunderstorm event No.2. Top: The intensity (Stokes I) footprint. Middle: Linear polarization as measured with individual LOFAR LBA (lines) in the shower plane. Bottom: The footprint of Stokes V, representing the circular polarization. In the top and bottom panels, the background color shows the simulated results while the coloring in the small circles represents the data.

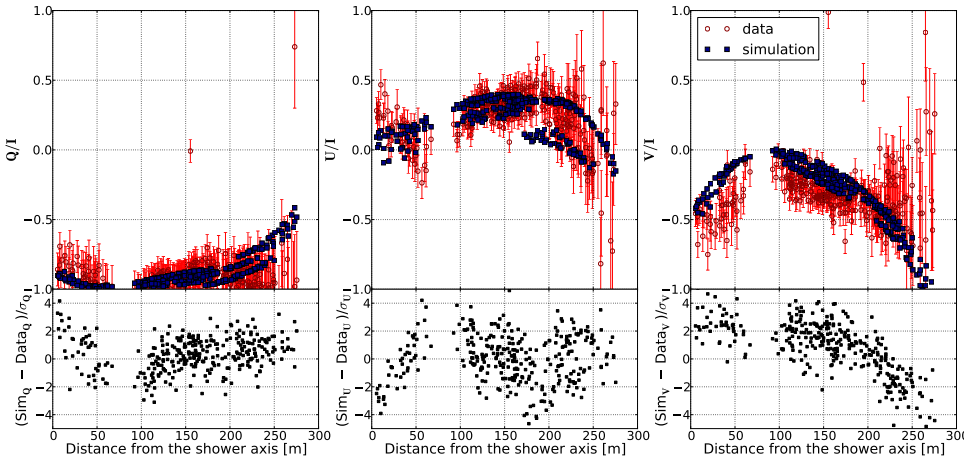

Fig. 4.9 The set of normalized Stokes parameters of the thunderstorm event No.2 as recorded with the LOFAR LBAs (open red circles) is compared to the results of the CoREAS simulation (filled blue dots). σ denotes one standard deviation error.

We have checked that the fit quality is sensitive to the heights of the layers on the order of hundred meters and the orientations of the electric fields at the level of degrees. However, it is not sensitive to heights above 8 km because at that height there are few particles in the shower and thus their contribution to the total radio emission is small. The electric fields shown in Table 4.1 and Table 4.2 only include the components of the true fields perpendicular to the shower axis. The parallel component of the electric fields hardly affects the LBA observations and thus it cannot be determined. In addition, in the frequency domain of the LBAs there is no sensitivity to the component of electric fields in excess of about 50 kV/m, so the strength of the perpendicular component can only be probed up to about this strength (see Ref. [91] for the discussion). To increase the sensitivity, we would need lower-frequency antennas.

However, as explained in the following we have measured large horizontal components of the electric fields along the shower axis in thunderclouds. A strict vertical electric field can be decomposed into two components, one along $\hat{e}_{\mathbf{v}}$ and the other one along $\hat{e}_{\mathbf{v}\times(\mathbf{v}\times\mathbf{z})}$. Measuring a component in $\hat{e}_{\mathbf{v}\times(\mathbf{v}\times\mathbf{z})}$ (see Table 4.1 and Table 4.2) could thus be a reflection of a vertical field since the present observations have little sensitivity to an $\hat{e}_{\mathbf{v}}$ component of the electric field. However, a nonzero

component in the $\hat{e}_{\mathbf{v}\times\mathbf{z}}$ direction (see Table 4.1 and Table 4.2) can never be a projection of a purely vertical electric field, and is thus a genuine signature of a horizontal component. We have confirmed that setting any of the $E_{\mathbf{v}\times\mathbf{z}}$ components to zero results in poorly reconstructed Stokes parameters. Therefore, it can be concluded that the atmospheric electric field is not fully vertical, but has a significant horizontal component. A three-layered structure and a horizontal component of the electric fields in thunderclouds have also been observed in balloon experiments [92, 53, 93, 41]. The large component of a horizontal electric field at high altitudes can be given by two oppositely charged regions inside a thundercloud. The small horizontal component at low altitudes can be given by the main negative-charge layer of a thundercloud in the center and a local positive-charge region at the bottom of the cloud.

4.5 Conclusion

Air showers measured with the LOFAR LBAs during thunderstorms have generally a much stronger circular polarization component near the shower axis than showers recorded during fair weather. We demonstrate on the basis of a simple model that this is a reflection of the fact that the orientation of atmospheric electric fields changes with height. This gives rise to a rotation in the direction of the transverse current as the air shower proceeds towards the surface of the Earth. This is also confirmed by CoREAS simulations.

Using the full set of the Stokes parameters thus strongly improves the determination of the atmospheric electric fields in thunderclouds. As specific examples, we have analyzed two thunderstorm events where we show that the intensity and polarization signature can only be described by a three-layered electric field. Also in baloon measurements, generally three different layers are observed below a height of 8 km. In our analysis, we also determine that the atmospheric electric field has a sizable horizontal component.

Chapter 5

Electric fields in thunderstorms measured by LOFAR

T. N. G. Trinh, O. Scholten, et al.
(In preparation to submit to JGR)

Abstract

We present measurements of radio emission from extensive air showers during thunderstorm conditions. Both intensity and polarization signatures of these events are very different from those measured during fair weather. We have developed a fitting procedure and analyzed 11 air showers. We show that, in order to reconstruct these showers, atmospheric electric fields in thunderclouds generally are composed of at least three layers. We find that the electric fields extracted from these events have some similar characteristics. Large horizontal components of the electric fields are observed in the middle and the top layers. The height of the bottom layer depends on the season. Based on our measurements, we describe a possible method to perform tomography for electric fields in thunderclouds.

5.1 Introduction

Lightning is a very interesting phenomenon but a detailed understanding of the process is still missing [41]. Knowledge of atmospheric electric fields plays an important role in understanding lightning initiation and propagation. However, measuring the fields is a very difficult task. Aircrafts [94], balloons and rockets [53] can measure the electric fields in the thunderclouds but they disturb the electric fields. In addition, they are influenced by violent winds and thus their directions change. Recently, a non-intrusive method, using radio emission from extensive air showers to determine thunderstorm electric fields was introduced [71]. Such measurements can be done with the Low Frequency Array (LOFAR) [23], explained further in Section 5.2.

An extensive air shower is produced when a primary cosmic ray enters into the atmosphere, generating many secondary particles when colliding with air molecules. These secondary particles will subsequently collide with air molecules and thus create an avalanche of particles in the atmosphere called an extensive air shower. In the plasma at the shower front, there are many electrons and positrons. In showers measured under fair-weather conditions, these electrons and positrons are deflected in opposite directions by the Lorentz force induced by the geomagnetic field. They generate a transverse current pointing to the direction of the Lorentz force and the changing current emits radio frequency radiation [25, 31]. This signal is linearly polarized along the direction of the Lorentz force, the $\mathbf{v} \times \mathbf{B}$-direction, where $\mathbf{v}$ is the direction of the shower and $\mathbf{B}$ is the Earth's magnetic field. Negative charge excess in the shower front also contributes to the radio emission [24, 64]. This excess is built up from the electrons that are knocked out of atmospheric molecules by interactions with shower particles. It also emits radio signals and its radiation is linearly polarized, but radially to the shower axis.

The electric fields during a thunderstorm affect the induced electric currents in air showers and thus the radiation from them [91]. The electric field component parallel to the shower axis, $\mathbf{E}_{\parallel}$, increases the number of electrons or positrons, depending on its sign. However, the particles generated by $\mathbf{E}_{\parallel}$ have low energies and thus they trail far away from the shower front. For this reason, the radio-emission of the additional charged particles contributes coherently in the low frequency regime of

less than 10 MHz, well below the frequency range of the LOFAR low band antennas, which ranges from 30 MHz to 80 MHz. As a result, LOFAR is not sensitive to $\mathbf{E}_{\parallel}$. The electric field perpendicular to the shower axis, $\mathbf{E}_{\perp}$, does not change the number of particles, but changes the direction and the strength of the force acting on the particles. As a result, the polarization and the magnitude of the current in the shower front change and thus radio signals do as well. Therefore, there are large differences in the intensity footprint between an air shower measured during a thunderstorm, a so-called thunderstorm event, and an air shower recorded during fair weather, a so-called fair-weather event. Because of these differences seen in the intensity pattern, using the method first introduced in Ref. [71], we can determine $\mathbf{E}_{\perp}$ during thunderstorms. We are not sensitive to heights larger than above about 8 km and lower than about 1 km since at these high and low altitudes the number of shower particles is small and thus the radio signals emitted from them is negligible. Unlike other electric field measurements, this technique is non-intrusive, i.e. it does not disturb the electric fields in the thunderclouds during the measurement.

We also observe significant differences in circular polarization between thunderstorm events and fair-weather events [95]. Unlike fair-weather events, we often see that the circular polarization for thunderstorm events does not depend on the azimuth positions of the antennas and the distance to the shower axis. In addition, the circular polarization for the fair-weather events is small near the shower axis where the charge-excess contribution vanishes [58] while it is large in many thunderstorm events. The reason for this is that in the fair-weather events, the circular polarization is caused by the time delay of the transverse-current pulse and the charge-excess pulse [58] while in the thunderstorm events, it is caused by the rotation of the direction of the current around the shower axis. Therefore, circular polarization data give useful information for the determination of atmospheric electric fields.

The microscopic models that produce the complete radiation field emitted from charged particles in the shower are ZHAires [30] and CoREAS [63]. CoREAS is a plugin for the shower simulation code CORSIKA [11]. For thunderstorm cases, atmospheric electric fields are implemented by turning on the EFIELD option [74] in CORSIKA. Since CoREAS is based on a Monte-Carlo simulation, changing a simple shower parameter will affect the development of the shower as a whole. This effect is similar to the well-known shower-to-shower fluctuations. Moreover, since CoREAS

traces individual charged particles, it requires large computer resources. Recently, an analytic code called MGMR3D has been developed [33]. MGMR3D calculates the radio footprint of an extensive air shower using a semi-analytical macroscopic approach based on the longitudinal structure of the current distribution. In contrast to CoREAS, this approach has no shower-to-shower fluctuations and requires little computing time. It has been shown that MGMR3D gives a good agreement with CoREAS for both fair-weather and thunderstorm cases [33].

In this work, we determine electric fields during thunderstorm conditions by fitting the radio intensity and polarization patterns of thunderstorm events. Since CoREAS simulations are time consuming and suffer shower-to-shower fluctuations, it is hard to use CoREAS in doing the fitting, especially in multi-dimensional fitting. Therefore, in this chapter, we develop a new fitting technique which consists of two steps. As a first step, by using MGMR3D to fit the radio intensity and polarization patterns, we determine the current profile from which the electric fields are extracted. Then we plug the parameters which give the best fits into CoREAS for the final calculations. We will show the results of 11 good thunderstorm events measured during a one-and-a-half-year period and discuss the implications for the thunderstorm structure.

5.2 LOFAR and data analysis

Data were recorded with LOFAR, a radio telescope built in the North of the Netherlands with many remote stations across Europe. The antennas of LOFAR are grouped into stations. Each station contains 96 low-band antennas (LBA; $10-90$ MHz) and 48 high-band antennas (HBA; $110-240$ MHz). The densest concentration of antennas, called the 'Superterp', is located near Exloo, in Drenthe in the Netherlands. The Superterp has a diameter of $\sim$320 m and consists of 6 stations. Electromagnetic pulses are measured by the dipoles, sampled every 5 ns and stored for 5 s on ring buffers for each active antenna. The data is Fourier transformed and filtered to the interval from 30 MHz to 80 MHz since below 30 MHz and above 80 MHz, radio frequency interference is strong. A trigger is obtained from a particle detector array, LOfar Radboud air shower Array (LORA), for air showers with a primary energy in

excess of 2×10^{16} eV [88]. Data for the present analysis are taken from LBAs mainly at the Superterp.

We use the following criterion to select good thunderstorm events. First, as shown in Ref. [71], the linear polarization in thunderstorm events are very different from that in fair-weather events, so it is used as the first signature in collecting thunderstorm events. Second, the events should have radio signals recorded in at least 4 LBA stations and there should be at least one station within 100 m from the shower axis receiving signals. Third, the mean fractional uncertainty of the intensity should be less than 30%; otherwise, the uncertainties of the data are too large to draw any conclusions. Fourth, since the core position is very essential in fitting, the events should have at least one scintillator having the energy deposit larger than 100 MeV. This will be discussed in more detail in Section 5.3. In this work, we have analyzed data from December 2011 to August 2014. During this period, there were 31 thunderstorms events from which 11 thunderstorm events that obey all aforementioned conditions were selected. We also cross-check with lightning data from the Royal Netherlands Meteorological Institute. For these 11 thunderstorm events, there were lightning strikes occurring within about 150 km from the LOFAR 'Superterp' and within two hours from the data-tracking period. The correlation between thunderstorm events and lightning activity will be discussed in more detail in Section 5.5.

The data were processed in an off-line analysis [36] where the arrival direction and the energy of air showers were estimated. In addition, for each antenna, the Stokes parameters expressed as

$$\begin{aligned} I &= \frac{1}{n}\sum_{i=0}^{n-1}\left(\left|\mathcal{E}_{i,\mathbf{v}\times\mathbf{B}}\right|^2+\left|\mathcal{E}_{i,\mathbf{v}\times(\mathbf{v}\times\mathbf{B})}\right|^2\right), \\ Q &= \frac{1}{n}\sum_{i=0}^{n-1}\left(\left|\mathcal{E}_{i,\mathbf{v}\times\mathbf{B}}\right|^2-\left|\mathcal{E}_{i,\mathbf{v}\times(\mathbf{v}\times\mathbf{B})}\right|^2\right), \\ U+iV &= \frac{2}{n}\sum_{i=0}^{n-1}\left(\mathcal{E}_{i,\mathbf{v}\times\mathbf{B}}\mathcal{E}^{*}_{i,\mathbf{v}\times(\mathbf{v}\times\mathbf{B})}\right), \end{aligned} \tag{5.1}$$

are calculated [37]. Note that all Stokes parameters are real. $\mathcal{E}_i = S_i + i\hat{S}_i$ are the complex signal radiation fields, where $\hat{S}_i$ is sample i of the Hilbert transform of S.

The radiation fields S are recovered from the measured voltages by inverting the antenna calibration. The summation is performed over n = 11 samples, centered around the peak of the pulse. Stokes I is the intensity of the radio emission. Stokes Q and U are used to derive the linear-polarization angle

$$\psi = \frac{1}{2}\tan^{-1}\left(\frac{U}{Q}\right), \tag{5.2}$$

and Stokes V represents the circular polarization.

5.3 Reconstruction technique

In fair-weather events, the intensity pattern depends strongly on $X_{\max}$, the atmospheric depth where the number of secondary particles reaches a maximum. Therefore, for the fair-weather events, $X_{\max}$ can be found by fitting the measured intensity pattern on the ground with CoREAS as presented in Ref. [61]. Here, we will follow the same basic principle. However, during thunderstorm conditions, the transverse current in air showers varies with height not only because of the variation of the number of charged particles with height like in the fair-weather events, but also because of the changes in the electric fields. In thunderstorm events, the effects from the electric fields generally dominate the height variation of the number of charged particles. Since the electric fields and thus the transverse currents change both their magnitude and direction, it is necessary to consider both intensity and polarization data or, equivalently, a full set of Stokes parameters.

For this work, we will use the idealized three-layer charge structure. There is an upper positive charge on top, a negative charge in the middle and a small positive charge region at the bottom. This charge structure implies that the electric field should have three layers. Each layer i is defined by h_i, the altitude of the top of the layer, and the strength and direction of $\mathbf{E}_\perp$. The layers will be identified by indices 1, 2 and 3. The top layer, 1, thus has the field $\mathbf{E}_{\perp\mathbf{1}}$ stretching between the heights h_1 and h_2. The bottom layer, often layer 3, with the field $\mathbf{E}_{\perp\mathbf{3}}$ is between h_3 and the ground. The three-layered structure of the electric fields is consistent with balloon measurements measuring the vertical components of the electric fields [93, 53]. Note that there are also horizontal components of the electric fields since charge layers

are not flat and do not have the same sizes. In this work, we only consider the field $\mathbf{E}_\perp$ which is perpendicular to the shower axis. For a vertical shower, the field $\mathbf{E}_\perp$ is horizontal. In reality, we usually measure inclined showers, so $\mathbf{E}_\perp$ contains both horizontal and vertical components of the electric fields. As discussed in the introduction, $\mathbf{E}_\parallel$ has very little effect on the radio emission in the frequency range from $30-80$ MHz [71, 91], and so it is set to 0 in this work. As discussed in Ref. [91], when the perpendicular electric field $E_\perp$ is small, the drift velocity and thus the amplitude of the radio signal is proportional to the strength of the electric field. When the electric field becomes larger than about 50 kV/m, the increased drift velocity results in a decreased longitudinal velocity since the total velocity cannot exceed the speed of light. For this reason, some charged particles start to trail further behind the shower front and their radiation is not added coherently in the LOFAR frequency range. This results in a saturation in the radio intensity starting when the electric field is larger than about 50 kV/m. In each layer, the electric field $\mathbf{E}_\perp$ is homogeneous and thus it should be considered as an effective electric field. Any change in the field over distances smaller than about 500 m gives very small effects [91].

The core position is essential in doing the fitting. In principle, the core position can be determined by LORA data, however, analysis of fair-weather data suggests that the actual core position, as determined from the radio data, can easily be displaced by 50 m from the core position determined from the LORA data. Therefore, in fair-weather events, the core position is found by doing the fitting for both radio and particle data [61]. In thunderstorm events, finding the core position is more difficult and using the fitting to find it is not the best way because the intensity and polarization patterns of the thunderstorm events, in general, are complicated and we cannot measure the whole pattern but only parts. In addition, they are not the same in all thunderstorm events, but vary from event to event. Also, as discussed later, in the first step when using MGMR3D, we do the fitting for the Stokes parameters, but we cannot do the fitting for the particle density. For this reason, if we use the fitting to find the core position, we may get a wrong core position which can generate a weird particle-density profile. For these reasons, we correct the core position manually. We use the core position defined by LORA as the first guess and move the core around such that both radio and particle data change smoothly as a function of distance from

the shower axis. The core position which we find is kept fixed in both MGMR3D calculations and CoREAS simulations.

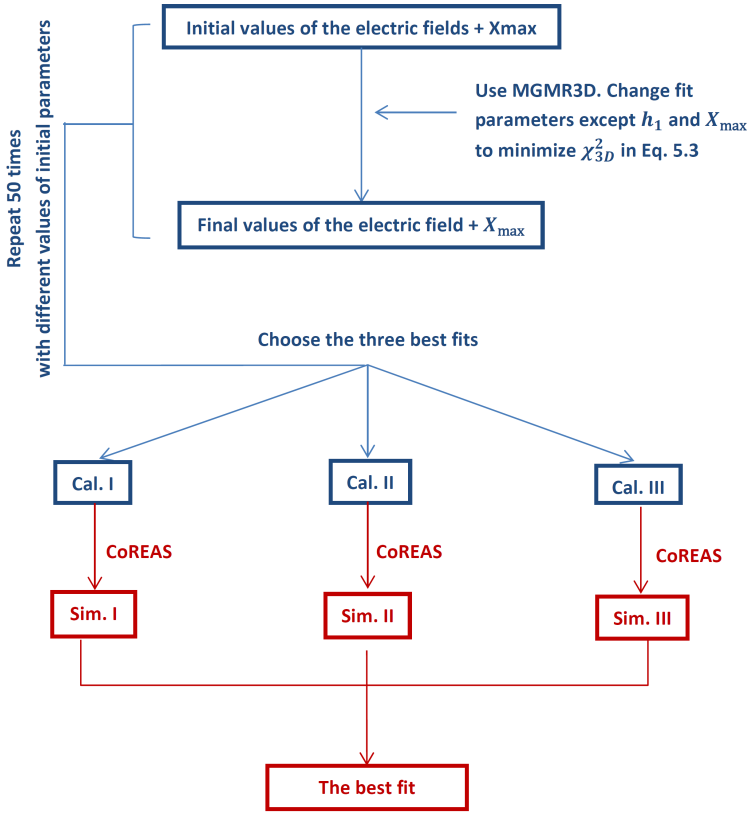

Fig. 5.1 The fitting procedure

Unlike in fair-weather events where there is only one free parameter, $X_{\max}$, thunderstorm events have many free parameters depending on the model for the electric field. For a three-layer model of electric fields, the number of the parameters is 10. Hence, a grid search is not practical for the fitting. In order to fit these parameters to the data, we use the method of steepest descent. In order to use this method, one needs to make sure that a small change in the radio footprints is due to a small change in the parameters of the electric field and not due to shower-to-shower fluctuations. Therefore, as mentioned in the introduction and as shown schematically

in the diagram in Fig. 5.1, the fitting procedure for thunderstorm events contains two steps. In the first step, we use MGMR3D since it does not have shower-to-shower fluctuations and it requires little computing time. Since the current profile is the product of the drift velocity, mainly determined by the strength of the electric fields, and particle profile, mainly determined by $X_{\max}$, the strength of the electric fields can compensate $X_{\max}$ to a certain extent. Thus, $X_{\max}$ and the electric fields are not linearly independent. For this reason, we fit the parameters in the electric field profile while keeping $X_{\max}$ fixed. In addition, as mentioned in the introduction, since we are not very sensitive to h_1, we also keep it fixed in order to reduce the number of fit parameters. The initial values of $X_{\max}$ and h_1 are chosen randomly in the ranges of $500-800$ g/cm^2 and $6-15$ km, respectively. The initial values of the other parameters are also randomly selected. By using the steepest descent method, we change 8 parameters of the three-layered electric fields to minimize

$$\chi^2_{3D} = \sum_{\text{antenna}} \sum_{S=I}^{Q,U,V} \left(\frac{S_{\text{ant}} - f_r^{3D} S_{\text{cal}}\left(x_{\text{ant}} - x_0, y_{\text{ant}} - y_0\right)}{\sigma^S_{\text{ant}}} \right)^2 . \tag{5.3}$$

Here S_{ant} denotes the measured Stokes parameter calculated from a 55-ns window for an antenna located at $(x_{\text{ant}}, y_{\text{ant}})$ with an uncertainty σ^S_{ant} and S_{cal} is the calculated Stokes parameter. The shower core is located at (x_0, y_0). f_r^{3D} is a scaling factor of the radio intensity which is introduced to facilitate the fitting. The magnitude of the intensity, related to the energy of the shower, will be determined in the following step in conjunction with the particle spectrum.

CoREAS and MGMR3D agree quite well for thunderstorm cases when the perpendicular electric fields do not exceed about 100 kV/m. Hence, in MGMR3D, we put the limit on the strength of the electric fields at 100 kV/m. It has been checked that, if the fields are larger than this limit, the discrepancy between CoREAS and MGMR3D starts to increase. For each event, the fit in MGMR3D is repeated 50 times with different initial values of the parameters to make sure that we obtain a global minimum. Doing many calculations also helps us to check the uniqueness of our solutions. The results show that the current profiles are rather unique. This will be discussed in details in Sec. 5.4.

In the second step, we use CoREAS which has shower-to-shower fluctuations and which also simulates particle density. The parameters of the atmospheric electric fields and $X_{\max}$ from the three best fits given by MGMR3D are plugged into CoREAS for final calculations. The three best fits obtained in MGMR3D are called Calculation (Cal.) I, Cal. II and Cal. III. The CoREAS simulations corresponding to these calculations are Simulation (Sim.) I, Sim. II and Sim. III. For CoREAS simulations, χ^2_C values are calculated for both the Stokes parameters and the particle lateral distribution

$$\begin{aligned}\chi^2_C = &\sum_{\text{antenna}} \sum_{S=I}^{Q,U,V} \left(\frac{S_{\text{ant}} - f_r S_{\text{sim}}\left(x_{\text{ant}} - x_0, y_{\text{ant}} - y_0\right)}{\sigma^S_{\text{ant}}} \right)^2 \\ &+ \sum_{\text{particle detector}} \left(\frac{D_{\text{det}} - f_p D_{\text{sim}}\left(x_{\text{det}} - x_0, y_{\text{det}} - y_0\right)}{\sigma_{\text{det}}} \right)^2 ,\end{aligned} \tag{5.4}$$

where S_{sim} is the simulated Stokes parameter. D_{det} is the deposited energy measured by a LORA detector at the position $(x_{\text{det}}, y_{\text{det}})$ with an uncertainty σ_{det}. D_{sim} is the simulated deposited energy which is converted from the CORSIKA particle output by using a GEANT4 [96] simulation of LORA detectors. In Eq. 5.4, two scaling factors were introduced, the scaling factor for particle energy, f_p, and the scaling factor for the power, f_r. Since the number of particles on the ground is, to a good approximation, proportional to the energy of the shower, the energy in the simulation, E_{sim}, is adjusted until the scaling factor for particles, $f_p = E_{\text{CR}}/E_{\text{sim}}$ is unity, where E_{CR} is the energy of the air shower that is consistent with the results of the LORA detectors. The scaling factor for the radio power, f_r, obtained in CoREAS simulations remains. The units are chosen such that for fair-weather events $f_r = 1$. In principle, it is proportional to $E_\perp$ if the field is smaller than 50 kV/m and can thus be used to determine the strength of the fields. In practice, one of the fields in the fit can be stronger than 50 kV/m and this proportionality cannot be used any more. Thus, f_r is important for determining the quality of the fit since it depends on $X_{\max}$ as will be argued in Sec. 5.4 for different events. In the CORSIKA software, $X_{\max}$ is a result of the simulation. Therefore, for each configuration of the electric field, we perform 20 CoREAS simulations and choose the simulation which has the best reduced χ^2_C value.

The difference in $X_{\max}$ between the best simulations and MGMR3D calculations is less than 15 g/cm^2 .

5.4 Electric field determination

In this section, we will discuss the fitting for 11 thunderstorm events which were recorded during the period from December 2011 to August 2014 and obey all selection criteria mentioned in Section 5.2. As discussed in Section 5.3, for each event, we choose the three best fits from MGMR3D, each with a different value of $X_{\max}$ for which the optimal electric field configuration is searched. This is done because the parameters are not linearly independent, i.e. a change in $X_{\max}$ can be compensated by a change in the electric fields, keeping almost the same current structure. The parameters from these best fits are plugged into CoREAS for final calculations. The fit parameters and the reduced χ^2 obtained from both MGMR3D and CoREAS are given in the tables for each event (see Appendix). The best fit, given in bold in the tables, is chosen based on the reduced χ^2 obtained by CoREAS simulations. For the cases where the values of the reduced χ^2 are comparable, in order to determine the optimal electric field structure, we take the calculation where $f_r \approx 1$ as the best one. This will be discussed in more detail later in this section. The current profiles, the best fit of the Stokes parameters and particle density for each event are also displayed in the figures in the Appendix.

The tables of the fit parameters and the plots of the current profiles of all events (see the Appendix) show that for each event the heights of the middle and the bottom layers within the three best fits obtained by MGMR3D are almost the same. In addition, the height dependences of the currents in the three best fits are rather similar at low altitudes but they have some differences at altitudes higher than 5 km or 7 km depending on the events. However, the values of the reduced χ^2 values obtained by these fits do not differ much. The reason for this is that at large distances from the shower axis where mainly the radio emission from high altitudes is measured, there are no antennas or the data have rather large uncertainties. Therefore, at high altitudes, the current profiles are not unique and thus we are not sensitive to the electric fields at these heights. However, the current profiles and thus the electric field structures at low altitudes are well defined.

When the current changes sign in all layers, we obtain a comparable fit for the Stokes parameters. Thus, there are two solutions that are equivalent. At the level of the Stokes parameters, it is hard to distinguish between these two solutions. In order to do so, one needs to check the polarity of the radio pulses. In this work, we have compared the polarity of the calculated radio pulses generated by MGMR3D and that of the measured pulses by LOFAR in order to choose correct structures of the current and thus the electric fields. First, we have checked the polarity of the pulses of fair-weather events between data and MGMR3D to make sure that they are consistent. Then we have checked the polarity for all thunderstorm events. As an example, Fig. 5.2 shows the comparison between calculated and measured pulses at a distance of 125 m from the shower axis of event 8. As shown in the figure, the $\mathbf{v} \times (\mathbf{v} \times \mathbf{B})$-component of the pulse between MGMR3D and data are similar. The $\mathbf{v} \times \mathbf{B}$-component has some differences but it is dominated by noise. If the current profile is inverted, the sign of the amplitude will change.

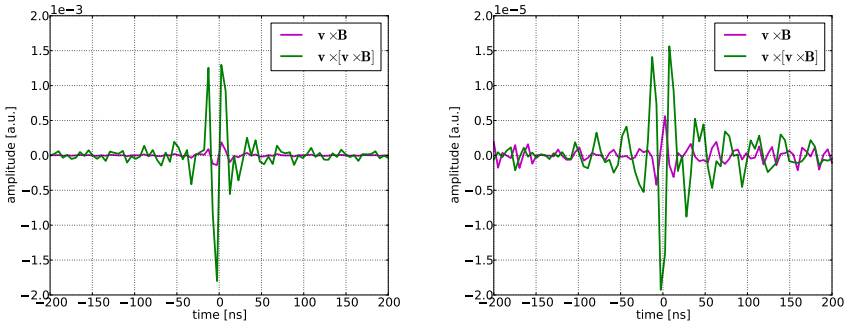

(a) Radio pulses generated by MGMR3D (b) Radio pulses measured by LOFAR

Fig. 5.2 Polarity of radio pulses at an antenna from event 8.

In general, the reduced χ^2 values obtained from MGMR3D and CoREAS are slightly different due to two reasons. Firstly, the radio patterns given by two codes are comparable but not exactly the same. Secondly, the fit in MGMR3D is done for only Stokes parameters while in CoREAS it is a joined fit to Stokes parameters as well as to the particle data.

All events except events 1, 5, and 6 show that over a wide range of $X_{\max}$ values, a reasonable agreement between the MGMR3D calculations and the data can be

obtained (see the tables in the Appendix). This is due to the fact that the height dependence of the currents in these fits are rather similar as shown in the figures of the current profiles (see Appendix). As discussed above, since the current is the product of the drift velocity as determined by the electric field and the particle profile as determined mainly by $X_{\max}$, one can be compensated by the other. For example, as can be seen in Table 5.4 of event 2, for larger values of $X_{\max}$, the relative strength of the fields E_2 versus E_1 becomes smaller. However, the number of particles on the ground depends strongly on $X_{\max}$ due to the attenuation of electrons in the atmosphere. For a large value of $X_{\max}$, i.e. the number of particles reaches the maximum closer to the ground, the number of particles on the ground is large. Therefore, for two showers having the same number of particles on the ground, the shower that has a larger value of $X_{\max}$ has a smaller energy $E_{\rm sim}$. Since $E_{\rm sim}$ is small, the amplitude of the radio signals generated by this shower also gets smaller. Thus, the radio scaling factor f_r is large for a large value of $X_{\max}$. As discussed in Section 5.3, an important factor for the amplitude of the radio signal is the strength of the electric field. For small electric fields, it is proportional to the field strength while it saturates for strong fields. Therefore, the radio scaling factor f_r depends also on the electric field. It reduces when the electric field increases and starts to saturate when the electric field becomes very large. As a result, this scaling factor f_r depends on both the field strength and the energy of the shower. For these reasons, although there are multiple solutions with a wide range of $X_{\max}$ values, the scaling factor f_r puts a constraint on choosing the best solution. For example, as shown in Table 5.4 of event 2, all three CoREAS simulations give almost the same reduced χ^2 value. However, since the values of $X_{\max}$ in Sim. I is smallest, the energy of the air shower is largest. In addition, the maximum strengths of electric fields are about the same, the radio scaling factor f_r thus mostly depends on the energy of the shower. As can be seen from the table, Sim. I of event 2 is the best fit since it has the smallest reduced χ^2 and the strength of the electric field is also well defined as the radio scaling factor f_r is unity. In contrast, the scaling factor f_r obtained within the three best fits in event 1, 5 and 6 does not show the dependence on $X_{\max}$ or on the energy of the shower. Note that event 1 is the worst case of all good thunderstorm events which we have analyzed. The fit of the intensity pattern is not really good (see the middle panel of Fig. 5.10), the scaling factor of the radio power f_r is not well determined. In event 5, since the current profiles from

the best fits obtained by MGMR3D are not the same, the scaling factor f_r depends not only on the energy of the shower but also on the electric fields. Unlike other thunderstorm events, event 6 is a special case because the intensity pattern strongly depends on $X_{\max}$. Table 5.3 shows that Sim. III fits the data best and the other two simulations which have smaller $X_{\max}$ do not reproduce the intensity pattern well. For this reason, the value of f_r in Sim. I and Sim. II are not well determined and thus are not comparable to the value obtained in Sim. III.

In event 1, 2, 4, 7, 8, and 10, the intensity pattern has a ring-like structure as can be seen from Fig. 5.3 which displays the intensity footprint of event 8. In the 1D plots of the Stokes parameters (see the middle panels of Fig. 5.10, Fig. 5.11, Fig. 5.14, Fig. 5.21, Fig. 5.27), the ring-like structure is seen as a peak in the Stokes I at a distance between 100 m to 250 m from the shower axis. The electric fields in the upper and lower layers of these events are almost in opposite directions introducing a destructive interference between the radio emission of these layers which gives rise to a ring-like structure in the intensity pattern. In addition, the radius of the ring in the intensity is strongly correlated to the height where the field is inversed. For smaller radii, the heights are smaller. For example, in event 2, the radius of the ring is 100 m and thus the field is inversed at 2.1 km (see Table. 5.4) while in event 10, the radius of the ring is about 250 m and thus the field is inversed at 4.9 km (see Table. 5.12). In event 2, the amount of circular polarization (Stokes V) measured is very small (see the middle panel of Fig. 5.11). Thus, this event can be fitted by a two-layered electric field where the fields in the two layers are almost opposite to each other (see Table. 5.4). In contrast to this event, events 1, 7, 8, and 10 which also show the ring-like structure in the intensity have a large amount of circular polarization. Therefore, these events cannot be reconstructed well by a two-layered electric field structure. In order to do that, the electric field needs to have at least three layers (see Table. 5.3, Table. 5.6, Table. 5.10, Table. 5.12). A third layer is needed to introduce the change in the orientation of the electric fields and thus the rotation of the transverse current which results in a large amount of circular polarization. In addition, a third layer also give rises to the change in the linear polarization which causes a 'wavy' pattern. Fig. 5.4, as an example, shows the 'wavy' pattern of event 7 where the linear polarization rotates about 90° from small distances near the shower axis to large distances beyond 100 m from the shower axis. Event 4 is an odd one

since there is large amount of circular polarization near the shower axis but the linear polarization is unique over all antennas (see the middle panel of Fig. 5.14). Therefore, as shown in Table. 5.6, the electric fields in the bottom and the middle layers are not fully opposite but they have an angle of about 150°.

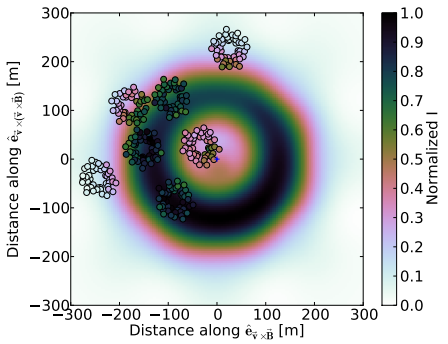

Fig. 5.3 The intensity (Stokes *I*) footprint of event 8. The background color shows the simulated results while the coloring in the small circles represents the data.

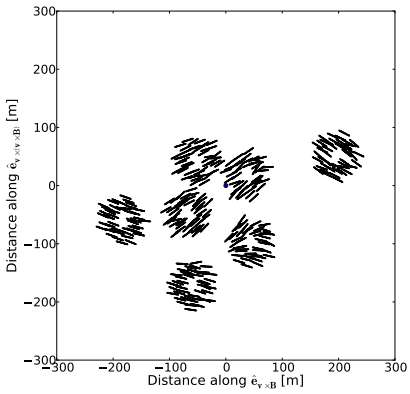

Fig. 5.4 Linear polarization footprint of event 7 as measured with individual LOFAR LBAs (lines) in the shower plane.

In contrast to the events just discussed above, in events 3, 6, 9, and 11, the intensity patterns are similar to those in fair-weather events (see the middle panels of Fig. 5.12, Fig. 5.19, Fig. 5.24, Fig. 5.G). However, in these events with the exception

of event 11, unlike the fair-weather events, the signals are not polarized along the $\mathbf{v} \times \mathbf{B}$-direction because Q/I is not equal to 1 (see the middle panels of Fig. 5.12, Fig. 5.19, Fig. 5.24). In both events 3 and 6, since U/I is about -1, the linear polarization makes an angle of about -45° with the $\mathbf{v} \times \mathbf{B}$-direction. For this reason, the electric fields in the layers where the current is large, i.e. the middle layer of event 3 and the top layer of event 6 (see Table. 5.5 and Table. 5.8), make an angle of about -55° with respect to the $\mathbf{v} \times \mathbf{B}$-direction. There is some amount of circular polarization in these two events but it is small. In event 9 which has been discussed in detail in Ref. [95], the polarization footprint shows a 'wavy' pattern and there is a large amount of circular polarization, varying as a function of distance from the shower axis. Therefore, the electric field in the middle and the bottom layer rotates 90° to introduce the rotation of the linear polarization as well as the amount of circular polarization (see Table. 5.11). Event 11 is an odd case because not only the intensity but also the linear polarization looks like those of fair-weather events, except for the signals measured at large distances from the shower axis where Q/I is much smaller than 1 (see the middle panel of Fig. 5.G). The main difference from a fair-weather event is, however, that the circular polarization is large and changes its handedness with distances which is caused by the rotation of the electric fields and thus the currents in three layers. Near the shower axis, the signal at the bottom layer arrives earlier than the signal from the other layers because the showers propagates with the speed of light while the signal moves at a reduced speed due to the finite refractivity of air. This gives rise to a large amount of circular polarization at small distances, V/I = 0.4. At 150 m from the shower axis, the signal from the middle layer arrives sooner than the signal from the bottom layer, so V/I = -0.4. Similarly, beyond 150 m, the signal from the top layer arrives sooner than that in the other layers, so the circular polarization continues to decrease at large distances.

The features of circular polarization in event 11 are also shown in event 5 (see the middle panel of Fig. 5.16). However, unlike event 11 and the other thunderstorm events showing a fair-weather intensity pattern, event 5 shows a different intensity pattern. At large distances beyond 100 m from the shower axis, the intensity drops as a function of distance as it does in fair-weather events, however, at small distances, it is almost constant. As a result, as shown in Table. 5.7 and the top panel of Fig. 5.16,

the electric field and thus the current in the bottom layer is very small yielding a small radio signal near the shower axis.

As discussed in Section 5.3, the core position is found manually and is kept the same in both MGMR3D and CoREAS. For each event, we also show the fit of the particle density as a function of distance from the shower axis on the ground (see plots of particle density in the Appendix). We show the particle profiles where the core position is defined by LORA or after readjusting it. The absolute value of the core offset is small for most of the events, except event 11 (see the discussion in the Appendix).

5.5 Discussion

We have analyzed 11 thunderstorm events measured in the period from December 2011 to August 2014 from which the electric fields are extracted. Table. 5.1 shows for all 11 thunderstorm events the UTC time, the zenith angle, θ and the azimuth angle, ϕ, which can be used to reconstruct the shower directions (see Fig. 5.5). There were 4 thunderstorm events (1, 2, 3, and 9) measured during the winter, 6 events (5, 6, 7, 8, 10, and 11) during the summer and event 4 in April. In particular, there were 3 events recorded within 12 minutes in a winter night and 3 events measured within 36 minutes in a summer day. This allows a comparative analysis which will be discussed in Sec. 5.5.3. The table also shows the electric field configuration extracted from the thunderstorm events. All of these events can be reconstructed rather well by a three-layer model of atmospheric electric fields. The atmospheric electric fields extracted from these 11 thunderstorm events have some interesting features.

5.5.1 Charge structure

Since the heights h_1, h_2 and h_3 are the altitudes where the electric field changes, they correspond to the altitudes of the charge regions in the thundercloud. The sign of the charge in different layers needs to be interpreted on a case-by-case basis which will be discussed later in this section. All events show that the lowest layer which we can detect for the summer events (5, 6, 7, 8, 10 and 11) lies at a much higher altitude

Event - ID	UTC Time	θ (°)	ϕ (°)	h_1 (km)	$E_{1\mathbf{v}\times\mathbf{z}}$ (kV/m)	h_2 (km)	$E_{2\mathbf{v}\times\mathbf{z}}$ (kV/m)	h_3 (km)	$E_{3\mathbf{v}\times\mathbf{z}}$ (kV/m)	h_0 (km)	h_{-10} (km)
1	14/12/2011, 21:02:27	39.4	144.8	7.6	2	3.3	85	1.6	2	0.7	2.3
2	14/12/2011, 21:10:01	14.1	134.0	9.2	35	-	-	1.9	69	0.7	2.3
3	14/12/2011, 21:14:34	24.4	333.0	7.9	22	5.0	38	2.3	4	0.7	2.3
4	26/04/2012, 15:22:33	22.2	129.0	10.1	8	7.4	7	3.0	5	1.5	3.4
5	28/07/2012, 02:20:21	22.3	2.2	7.2	3	5.6	77	3.2	10	3.6	5.6
6	26/08/2012, 13:52:23	22.8	143.8	7.8	76	-	-	3.7	5	2.5	4.2
7	26/08/2012, 14:02:56	17.6	309.5	7.3	7	3.6	2	1.7	11	2.5	4.2
8	26/08/2012, 14:28:19	24.8	308.7	8.0	40	6.9	20	2.7	17	2.5	4.2
9	30/12/2012, 12:38:37	15.6	304.0	8.0	50	5.0	15	2.0	1	0.8	2.2
10	26/07/2013, 12:17:26	15.5	40.2	7.6	14	4.9	70	3.6	44	3.8	5.7
11	27/06/2014, 14:44:03	14.6	238.6	6.3	46	4.5	3	3.3	3	2.5	4.2

Table 5.1 The left part of the table shows the event ID, the time of measurements and the directions of 11 showers. The next three parts show the height of the top region where the layer starts and the horizontal electric field $E_{\mathbf{v}\times\mathbf{z}}$ determined from the best fit (see Appendix). Note that event 2 and event 6 have only two layers which are labelled as the top and the bottom ones. The last two columns present isotherm altitudes found from GDAS data (see [97]).

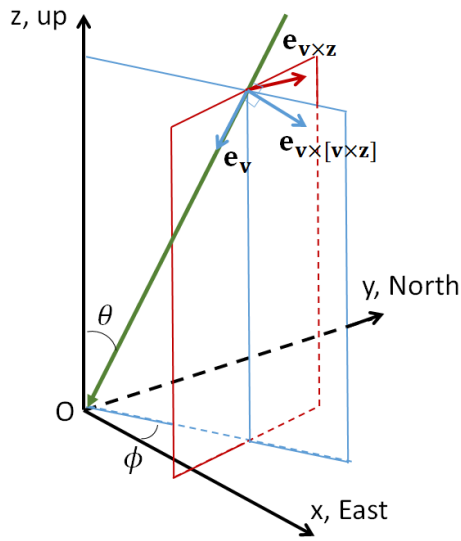

Fig. 5.5 The shower direction and the electric field components.

than for the winter events (1, 2, 3 and 9). This seasonal difference is most likely due to the temperature difference between summer and winter.

Summer events

Of the summer events, three events (5, 10, and 11) seem to have three distinct charge regions that likely correspond to upper positive, main negative, and lower positive charge regions. The other three summer events 6, 7, and 8, are special because these events passed through the same thunderstorm within 36 minutes. As shown in Table 5.1, h_3 in event 7 is much lower than that in events 6 and 8. This can be interpreted due to a local small positive charge region that is only seen in event 7. Since the showers of events 6 and 7 came from two different directions, the regions of the thunderclouds where they passed through may not be the same. In addition, although the showers of events 7 and 8 passed through a similar part of the atmosphere, the time between these two events is 26 minutes which could be long enough for the charge in the region where these events passed through to change because of the motion of the thunderclouds. These could be the reasons why the small lower positive layer in event 7 is not seen in events 6 and 8. The main negative

charge region seems to lie around 2.7 to 3.7 km, shown by h_3 in event 6 and 8 and h_2 in event 7. h_1 in events 6 and 7 could refer to the upper positive charge region around 7.3 km to 7.8 km. In event 8, the upper positive layer could lie at $h_2 = 6.9$ km and there could be another small screening layer at $h_1 = 8$ km which is not present in events 6 and 7. Ref. [42] has shown that, for Florida summer thunderstorms, the lower positive charge region tends to lie on the 0° C isotherm and the negative charge region tends to lie between the 0° C and -10° C isotherms. The last two columns of Table 5.1 show the altitudes of the 0° C and -10° C isotherms for comparison with our measured charge layer altitudes. Most of the summer events we measured are consistent with the lower positive charge regions occurring near the 0° isotherm.

Winter events

In contrast, the four winter events (1, 2, 3 and 9) have the lowest detected charge region which is at least a kilometer higher than the 0° C isotherm. For events 1, 3 and 9, there are three possibilities. First, these events could have a traditional tri-polar structure: upper positive, main negative, and lower positive charge regions. This means the lowest charge region detected is the lower positive layer lying at an altitude much higher than the 0° C isotherm. This is not consistent with Ref. [42] or our summer events. It could be that for these three events occurring in December, when the 0° C isotherm is at a very low altitude, the thunderstorm charging mechanism differs from that of summer thunderstorms, where the 0° C isotherm is at a much higher altitude. Second, since we are not sensitive to the parallel component of the electric fields, it is hard to determine the vertical component and thus the charge polarity of the different layers. Therefore, it could be that these events have an inverted-polarity charge structure: upper negative, main positive and lower negative charge regions, which is also shown in Ref. [98]. A third possibility is that there could be a charge layer at the 0° C isotherm but our method might not be sensitive to it since the radio emission close to the ground gives minor contribution to the intensity pattern. Event 2 is odd since it has only two charge regions and the field in the lower one is large. This could point to the fact that there is another charge layer near the ground which we are not sensitive to.

5.5.2 Electric fields

We are able to determine the electric field component $\mathbf{E}_\perp$, which is perpendicular to the shower axis. Since LOFAR is not sensitive to $\mathbf{E}_\parallel$, which is parallel to the shower axis, it is hard to determine the total electric fields for each individual event. The perpendicular component $\mathbf{E}_\perp$ can be decomposed into $\mathbf{E}_{\mathbf{v}\times\mathbf{z}}$ and $\mathbf{E}_{\mathbf{v}\times[\mathbf{v}\times\mathbf{z}]}$ components (see Fig. 5.5). The component $\mathbf{E}_{\mathbf{v}\times\mathbf{z}}$ is purely horizontal and does not contribute to the vertical electric field [95]. For each event, the component $\mathbf{E}_{\mathbf{v}\times\mathbf{z}}$ is derived for each of the different layers and is presented in Table 5.1. As shown in Table 5.1, we observe large horizontal electric fields in all 11 thunderstorm events. The large horizontal electric field can be present in any layer but mostly at high altitudes as can be seen from Fig. 5.6 which presents the distributions of the horizontal component $E_{\mathbf{v}\times\mathbf{z}}$ in three layers. The left panel of the figure shows that the horizontal electric fields between the bottom layer and the ground are small except for the horizontal field in event 2. The fields become large inside the thunderclouds as seen in the middle and right panels of the figure. This is as one would expect since the horizontal component of the field is due to the fact that the charge layers are not purely horizontal, or one is at the edge of the charged layer. Since the charges on the ground are influenced by the charges in the bottom layer of thunderclouds and Dutch ground is flat, the electric field between the ground and the bottom charge layer is most likely vertical. In event 2 where the field below the lower layer is large, as discussed above, it could be that there was a lower charged layer at altitudes lower than 1 km which we are not sensitive to. Thus, the field of 69 kV/m may not be the field between the cloud and ground but is between the middle and lower charged layers. Inside the cloud, the charge-layer structure is more complicated.

5.5.3 Tomography of electric fields

As discussed above, we can only determine the perpendicular component $\mathbf{E}_\perp$ since LOFAR is not sensitive to the parallel component $\mathbf{E}_\parallel$ of the electric field. However, there are two groups of events which were measured in a short time span (see Table 5.1). So, if one assumes that the field in the thundercloud where the showers of these events pass through does not change very fast, one can determine the component $\mathbf{E}_\parallel$ and thus the total electric field $\mathbf{E}$. We consider two showers i and j coming close

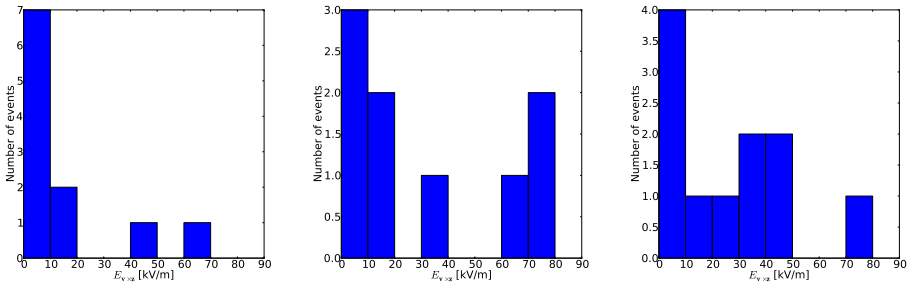

(a) Bottom layer (b) Middle layer (c) Top layer

Fig. 5.6 $E_{\mathbf{v}\times\mathbf{z}}$ distribution

in time and from $\mathbf{v_i}$ and $\mathbf{v_j}$ directions, respectively. The perpendicular components of the electric fields determined from these two events are $\mathbf{E_{i\perp}}$ and $\mathbf{E_{j\perp}}$. Assuming that the total fields $\mathbf{E}$ in the thundercloud where the showers of these two events passing through are the same, we obtain

$$\begin{aligned} \mathbf{E} &= \mathbf{E}_{i\perp} + E_{i\parallel}\mathbf{v}_i \\ \mathbf{E} &= \mathbf{E}_{j\perp} + E_{j\parallel}\mathbf{v}_j\,, \end{aligned} \tag{5.5}$$

where $E_{i\parallel}$ and $E_{j\parallel}$ are the magnitude of the parallel components of the electric fields in two events. This system of vector equations can be written in scalar equations by taking the dot product of Eq. (5.5) with $\mathbf{v}_i \times \mathbf{v}_j$, $\mathbf{v}_i$ and $\mathbf{v}_j$, respectively. One thus obtains

$$\mathbf{E}_{\perp i} \cdot (\mathbf{v}_i \times \mathbf{v}_j) = \mathbf{E}_{\perp j} \cdot (\mathbf{v}_i \times \mathbf{v}_j)\,, \tag{5.6}$$

and

$$\begin{aligned} E_{\parallel i} &= \frac{\mathbf{E}_{\perp j}\cdot\mathbf{v}_i + (\mathbf{v}_i\cdot\mathbf{v}_j)(\mathbf{E}_{\perp i}\cdot\mathbf{v}_j)}{1-(\mathbf{v}_i\cdot\mathbf{v}_j)^2} \\ E_{\parallel j} &= \frac{\mathbf{E}_{\perp i}\cdot\mathbf{v}_j + (\mathbf{v}_i\cdot\mathbf{v}_j)(\mathbf{E}_{\perp j}\cdot\mathbf{v}_i)}{1-(\mathbf{v}_i\cdot\mathbf{v}_j)^2}\,. \end{aligned} \tag{5.7}$$

The total electric field $\mathbf{E}$ is consistent for two events if Eq. (5.6) is obeyed, then $E_{\parallel i}$ and $E_{\parallel j}$ can be calculated from Eq. (5.7) and the total field $\mathbf{E}$ can thus be derived. We apply this analysis in two groups, (events 1, 2 and 3) and (events 6 and 7), where the events in the groups were recorded in short time slots. The core positions of these

showers at different altitudes are shown in Fig. 5.7 and Fig. 5.8. For each event,

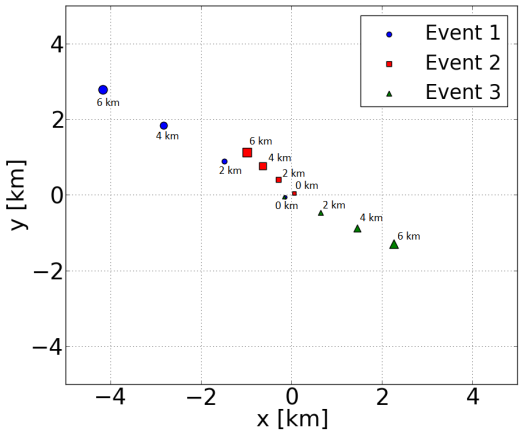

Fig. 5.7 The core positions of events 1, 2, and 3 at different altitudes.

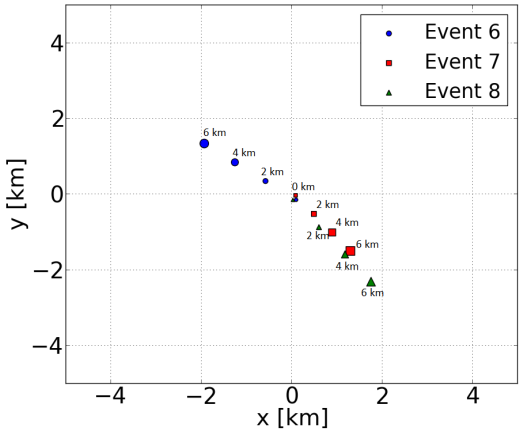

Fig. 5.8 The core positions of events 6, 7, and 8 at different altitudes.

we have checked the consistency of the electric fields (see Eq. (5.6)) for the three best fits and the results are given in Table. 5.2. To be able to judge if two showers move through a similar electric field configuration, as expressed by the criterium of Eq. (5.6), we need to have an estimate of the uncertainties in the extracted values of

$\mathbf{E}_\perp$. Here we may distinguish two different contributions. One is due to the fact that for different values of $X_{\max}$ one obtains a fit with a very similar chi-square value. The fits are distinguished on the basis of the value of the value of the normalization factor f_r that should be close to unity. Solutions with a similar chi-square value and a value for f_r that differs less than a factor 2 from the optimal solution can thus be considered equivalent. Another contribution to the uncertainty is the intrinsic uncertainty for the fit at a fixed value of $X_{\max}$. This is estimated by performing a re-fit of the field configuration keeping one field fixed at a value somewhat different from the optimum and checking the change in chi-square. This yields an estimate of the uncertainty of about 10 kV/m. For fields that exceed a value of 70 kV/m an equivalent fit can be obtained by decreasing this to 70 kV/m. Our conclusion is that the results given in Table 5.2 are accurate to within 5 kV/m for the smaller components while only up to 20 kV/m for components exceeding 50 kV/m.

5.5.4 Tomography of events 1, 2, and 3

For the first group of events 1, 2 and 3, we see that the fields in the bottom layers of these events are not consistent because the projections of $\mathbf{E}_{\perp\mathbf{i}}$ and $\mathbf{E}_{\perp\mathbf{j}}$ on $\mathbf{v_i} \times \mathbf{v_j}$-direction are different in sign or magnitude (see Table. 5.2). The shortest time gap is between event 2 and event 3, which is 4 minutes, and the distance between two points where the showers of these two events pass through in the bottom layer is about 1.5 km. Therefore, it could be that in this thundercloud, the horizontal electric field, and thus the charge density change over a distance less than about 1.5 km and in a period less than 4 minutes. Another possibility could be due to the fact that in event 2 there is a lower charge layer near the ground which will change $E_{3\mathbf{v}\times\mathbf{z}}$ and this would imply that the electric fields in these events are consistent but our analysis is not sensitive to this lower layer. For events 1 and 2, we have also checked the consistency of the electric fields in the top layer since these events come close in space (see Fig. 5.7); however, the electric fields in the top layer is not consistent since $\mathbf{E}_{\perp i} \cdot (\mathbf{v}_i \times \mathbf{v}_j)$ and $\mathbf{E}_{\perp j} \cdot (\mathbf{v}_i \times \mathbf{v}_j)$ are different in sign and magnitude (see Table. 5.2).

Layer in i – Layer in j	$\mathbf{E}_{\perp i} \cdot (\mathbf{v}_i \times \mathbf{v}_j)$			$\mathbf{E}_{\perp j} \cdot (\mathbf{v}_i \times \mathbf{v}_j)$		
	Sim. I	Sim. II	Sim. III	Sim. I	Sim. II	Sim. III
Bottom in 1 – Bottom in 2	-65	-70	-90	52	52	37
Top in 1 – Top in 2	-2	3	4	-27	-33	-60
Bottom in 2 – Bottom in 3	55	56	40	6	2	3
Bottom in 1 – Bottom in 3	-62	-67	-88	5	2	3
Bottom in 6 – Middle in 7	-2	-6	-6	17	15	12
Bottom in 6 – Bottom in 7	-2	-6	-6	-14	-10	-7

Table 5.2 Checking the consistency of electric fields extracted from events 1, 2 and 3 and from events 6 and 7 (see Eq. (5.6)). $\mathbf{E}_{\perp 1} \cdot (\mathbf{v}_1 \times \mathbf{v}_2)$ for the three best fits of event 1 are -65, -70, -90, respectively. $\mathbf{E}_{\perp 2} \cdot (\mathbf{v}_1 \times \mathbf{v}_2)$ for the three best fits of event 2 are 52, 52, 37, respectively.

5.5.5 Tomography of events 6, 7, and 8

For the second group of events 6, 7, and 8, we can see from the cloud reflectivity images shown in Fig. 5.18 that event 8 was recorded at a time when a very different cloud was over head as when events 6 and 7 were recorded. Tomography might thus be applied to events 6 and 7. Since for event 6, unlike for 7, no evidence for a separate layer below 1.7 km is found we have compared the bottom layer for 6 with the bottom as well as the middle layer for7. As one can see from the Table 5.2, the total electric fields **E** for the bottom layer of event 6 and the middle layer of 7 are not consistent, however the values for the bottom layers are much closer and this case is used to reconstruct the full electric field using Eq. (5.7). The determined components of the electric field are $(\text{East,North,Up})_{\text{bottom}} = (2.7 \pm 2.6, -14.4 \pm 3.0, -35.8 \pm 0.2)$ where the error bar denotes the spread in values obtained by using either event 6 or event 7. The sign of the vertical component of the field indicates a layer of positive charge at an height of 1.7 km in event 7. A similar analysis for the top layers of events 6 and 7, even though Table 5.2 shows that the components in the direction of $e_{\mathbf{v}_i \times \mathbf{v}_j}$ are not really consistent, gives $(\text{East,North,Up})_{\text{top}} = (16 \pm 23, 44 \pm 25, -93 \pm 2)$. The large errors in the horizontal components is a reflection of the mentioned inconsistency and surprisingly the up component is determined rather well indicating positive charge on top. Thus the picture emerges where the middle layer has negative charge while the top and bottom layers are positively charged.

5.5.6 Comparison with lightning location data

We have used the lightning discharges from KNMI [99] to check whether there were lightning flashes occuring nearby the LOFAR 'Superterp' and close to the time when 11 thunderstorm events were measured. For five events 6, 7, 8, 10 and 11, there were thunderclouds overhead at the time when these events were measured (see Fig. 5.17, Fig. 5.25, and Fig. 5.28). For events 1-3, 4, and 5, there were no lightning activities overhead, but we found lightning discharges at some distances from the LOFAR 'Superterp' within one hour from the measured time of these events but this does not mean that there was no charge separation for these events. The figures of radar reflectivity such as Fig. 5.9 show that radar reflectivity values exceed 35 dBZ for all events except 1-3 and 9. Note that for these events the 0°-isotherm

is well below the 1500-m level (at which radar data are displayed; see Table 5.1), resulting in a high fraction of ice in the radar measurement volume, leading to lower reflectivity values.

5.6 Conclusion

In this work, we have used our technique to analyze 11 thunderstorm events measured from December 2011 to August 2014. The intensity patterns and the polarization signatures of these events are reproduced rather well by our simple three-layer model of the electric fields. We have observed rather large horizontal component of the electric fields. Most of the summer events we measured have a clear triple layered structure and the lower positive charge region occurs near the 0 isotherm. For the winter events, as discussed above, there are some possibilities which can happen. Therefore, further work is needed to clarify the results.

Appendix 5.A

The appendix contains detailed results of the analysis for 11 thunderstorm events. We organize the events by day and there are plots of cloud reflectivity in a wider area around the LOFAR 'Superterp'. If there was lighting activity near by or overhead the 'Superterp', we also show a plot of lightning discharges. For each event, we include a table showing the fitting results, a plot of the current profiles of three best fits obtained from MGMR3D, a plot showing the best fit of the Stokes parameters and the particle density on the ground.

5.A.1 December 14th, 2011

For the three events detected on December 14th, 2011, there was no lightning activity detected in the vicinity of the Superterp. The nearest lightning activity was detected at a distance of 200 km and we have thus not included a lightning map. Cloud reflectivity measurements, Fig. 5.9, show that at the time of the shower detections an active cell of a cloud was passing over the Superterp. During the time span of the observations this cell passed over.

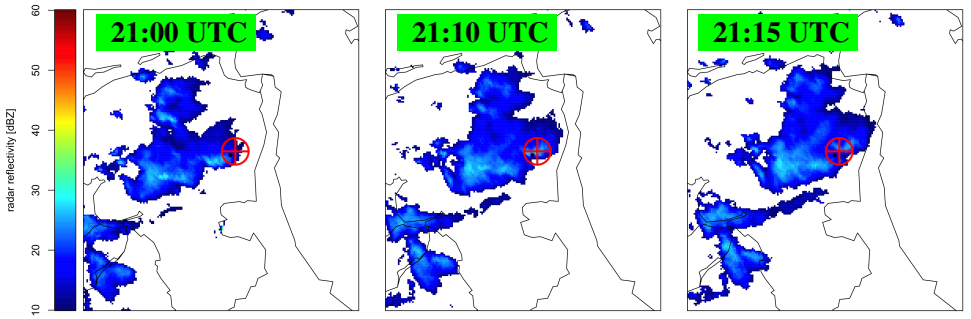

Fig. 5.9 Radar reflectivity in dBz as determined for different UTC times on 14/12/2011. The red ⊕ marks the location of the LOFAR 'Superterp'. There were 3 events measured on this day. Event 1 was measured at 21:02:27 UTC, event 2 at 21:10:01 UTC, and event 3 at 21:14:34 UTC.

Event 1 - 61592547

At small distances near the shower axis, the intensity determines the electric field in the bottom layer because the radio signals received here comes from the bottom layer. We choose Sim. III as the best fit since it has smallest reduced χ^2 and the ratio f is comparable to that in Sim. I. Since the intensity at small distances is very small, the electric field in the bottom layer is almost opposite to that in the middle layer in order to subtract the radio emission coming from the upper layers.

Calculation	I			II			**III**		
Energy (eV)	1.4×10^{17}			4.6×10^{16}			$\mathbf{4.0 \times 10^{16}}$		
Layer	1	2	3	1	2	3	**1**	**2**	**3**
h (km)	13.3	7.9	2.8	16.7	9.3	2.8	**7.6**	**3.3**	**1.6**
E (kV/m)	14	14	103	41	17	104	**15**	**107**	**42**
α (°)	156	-125	101	104	-109	104	**-103**	**119**	**-109**
$X_{\max}$ (g/cm^2)	526			634			**743**		
$X_{\max}$ (km)	$\equiv$ 7.3			$\equiv$5.9			$\equiv$ **4.7**		
χ^2_{3D}	3.12			3.36			**3.36**		
χ^2_C	4.41			4.14			**3.15**		
f	8.2			13.3			**8.4**		

Table 5.3 The values of the fit parameters and the results obtained by MGMR3D and CoREAS for event 1.

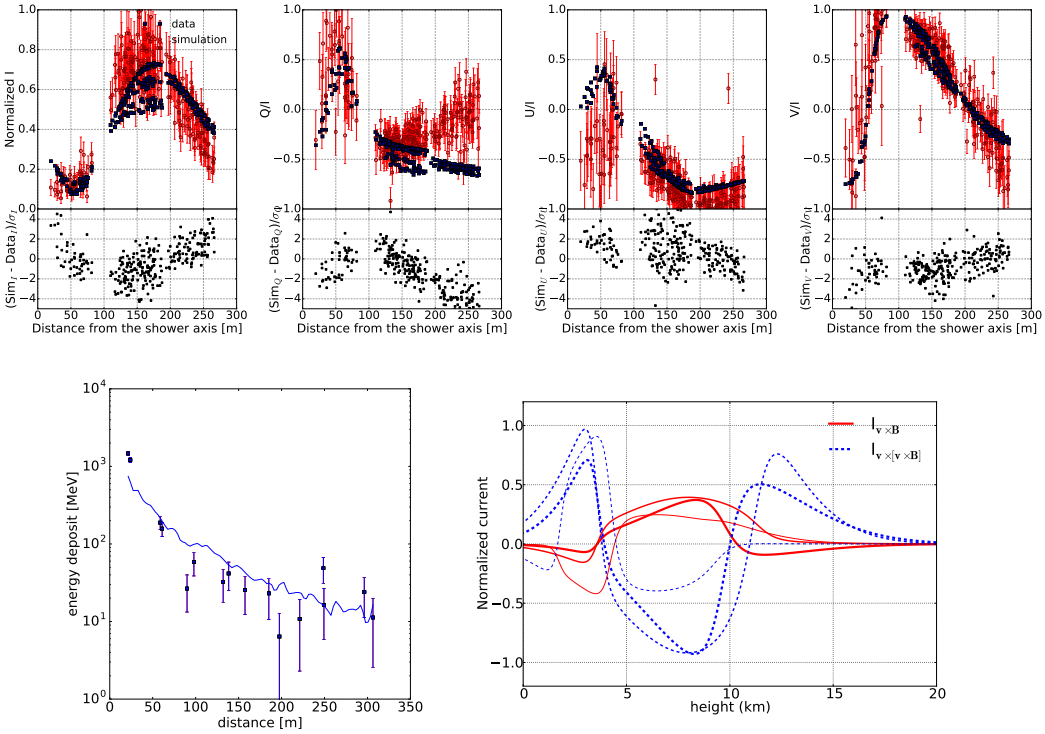

Fig. 5.10 Event 1. Top panel: The current profiles of three best fits obtained in MGMR3D. The thickness of the curves represents the value of the reduced χ^2 obtained in MGMR3D. For smaller values of the reduced χ^2, the curve is thicker. Middle panel: The fit III of normalized Stokes parameters between LOFAR data (open red circles) and CoREAS simulation (filled blue dots). σ denotes one standard deviation error. Bottom panel: The fit III of particle density on the ground between LORA data (points) and CoREAS simulation (curve). The core position in the fit is taken the same as it is determined by the LORA data.

Event 2 - 61593001

Near the shower axis, at about 50 m, the intensity reaches a minimum and starts to increases at distances near the shower axis. Therefore, the radiation from the bottom layer and thus the current in this layer are large as can be seen in the top panel of Fig. 5.11. Since $X_{\max}$ in Sim. I is small, the height where the number of particles reaches a maximum is in the top layer and thus the particle density becomes small in the bottom layer. For this reason, to have a large current at the bottom layer, the electric field in this layer needs to be strong, as shown in Table 5.4.

Calculation	**I**		II		III	
Energy (eV)	$\mathbf{2.9 \times 10^{16}}$		2.0×10^{16}		1.6×10^{16}	
Layer	**1**	**2**	1	2	1	2
h (km)	**9.2**	**1.9**	8.9	1.9	9.4	2.1
E (kV/m)	**42**	**86**	52	89	98	62
α (°)	**-174**	**9**	-173	10	-172	9
$X_{\max}$ (g/cm^2)	**595**		645		708	
$X_{\max}$ (km)	$\equiv$ **4.6**		$\equiv$ 4.1		$\equiv$ 3.3	
χ^2_{3D}	**0.91**		0.89		0.90	
χ^2_C	**1.34**		1.35		1.39	
f	**1.0**		1.4		2.0	

Table 5.4 The values of the fit parameters and the results obtained by MGMR3D and CoREAS for event 2.

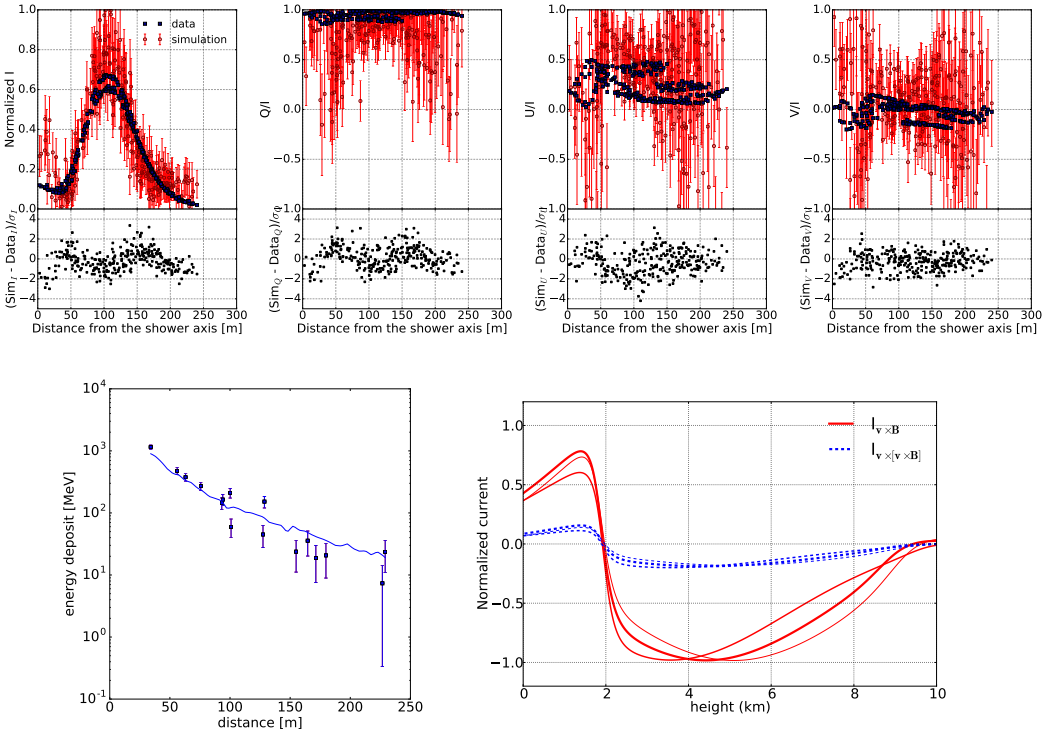

Fig. 5.11 Same as Fig. 5.10 but for event 2 where simulation I is selected. The core position in the fit is taken the same as it is determined by the LORA data.

Event 3 - 61593274

Sim. I is chosen to be the best fit since both values of the reduced χ^2 and the ratio f are smallest.

Calculation	**I**			II			III		
Energy (eV)	$\mathbf{4.3 \times 10^{16}}$			2.7×10^{16}			2.0×10^{16}		
Layer	**1**	**2**	**3**	1	2	3	1	2	3
h (km)	**7.9**	**5.0**	**2.3**	6.2	5.7	2.1	6.2	4.8	2.2
E (kV/m)	**23**	**89**	**17**	48	92	5	42	94	3
α ($^\circ$)	**-107**	**-59**	**-46**	-127	-60	-52	-109	-61	-140
$X_{\max}$ (g/cm^2)	**560**			670			758		
$X_{\max}$ (km)	$\equiv$ **5.6**			$\equiv$4.2			$\equiv$ 3.3		
χ^2_{3D}	**1.46**			1.48			1.47		
χ^2_C	**1.98**			2.45			2.09		
f	**2.7**			5.1			8.2		

Table 5.5 The values of the fit parameters and the results obtained by MGMR3D and CoREAS for event 3.

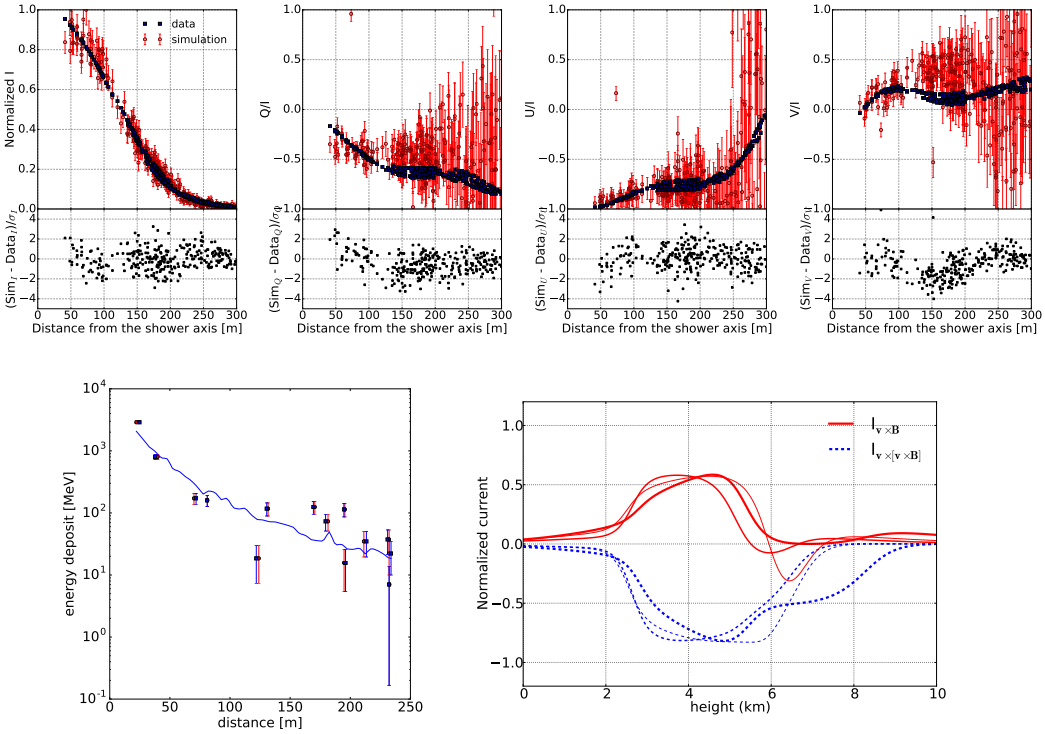

Fig. 5.12 Same as Fig. 5.10 but for event 3 where simulation I is selected. For this event the core position was moved over a distance of 3 m from the position originally determined from the LORA data. The bottom left panel shows in red the core position defined by LORA data while the blue markers show the results after adjusting the core position.

Appendix 5.B April 26th, 2012

At the time of this event there was lightning activity detected at a distance of about 100 km however none within the vicinity of the LOFAR core. The cloud-reflectivity data, Fig. 5.13, show that the shower passed through the edge of a rather extended cloud system with a very active core at about 20 km from the Superterp.

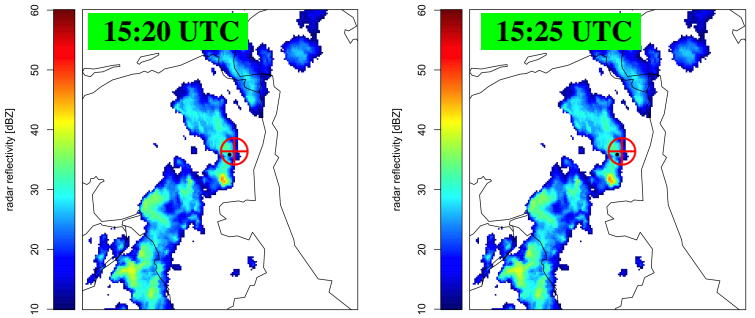

Fig. 5.13 The red ⊕ marks the location of the LOFAR 'Superterp'. Event 4 was measured at 15:22:33 UTC.

Event 4 - 73149753

Sim. I is preferred since the reduced χ^2 is smallest and the ratio f is comparable to that in Sim. II. As shown in the middle panel of Fig. 5.14, there is a small difference in the circular polarization near the shower axis. CoREAS predicts a smaller amount of circular polarization than visible in the data. At first sight, one may expect that this discrepancy could be solved by adding another layer below h_3 to introduce some rotation of the current which results in circular polarization. However, since Q and U show the same dependence as a function of distance, the linear polarization in all antennas is along a unique orientation. Therefore, the net forces between different layers cannot rotate much. Otherwise, the linear polarization would have a 'wavy' pattern.

Calculation	I			**II**			III		
Energy (eV)	6.0×10^{16}			$\mathbf{4.2 \times 10^{16}}$			3.6×10^{16}		
Layer	1	2	3	**1**	**2**	**3**	1	2	3
h (km)	11.2	7.1	3.2	**10.1**	**7.4**	**3.0**	10.9	7.2	3.1
E (kV/m)	58	65	30	**62**	**99**	**34**	56	77	21
α (°)	96	66	-111	**76**	**73**	**-102**	105	67	-126
$X_{\max}$ (g/cm^2)	507			**548**			633		
$X_{\max}$ (km)	$\equiv 6.3$			$\equiv$ **5.6**			$\equiv 4.5$		
χ^2 (MGMR3D)	3.35			**3.30**			3.36		
χ^2 (CoREAS)	3.85			**3.51**			3.62		
f	5.0			**5.9**			8.9		

Table 5.6 The values of the fit parameters and the results obtained by MGMR3D and CoREAS for event 4.

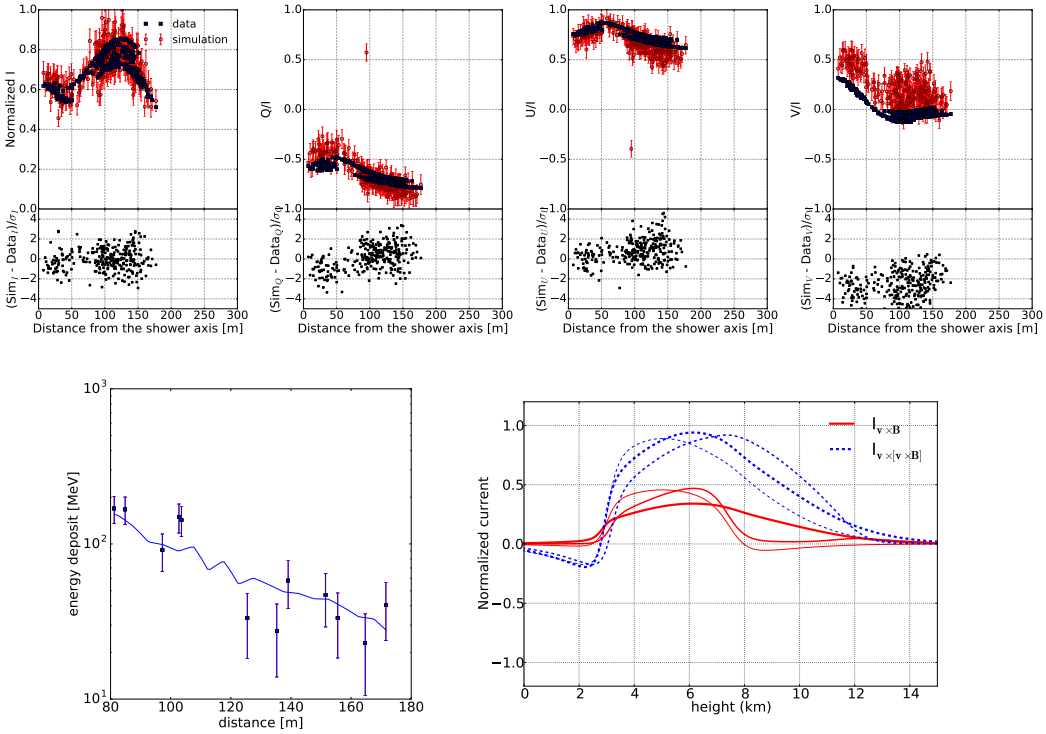

Fig. 5.14 Same as Fig. 5.10 but for event 4 where simulation II is selected.

Appendix 5.C July 28th, 2012

For event 5 lightning activity is detected only more than 12 hours after detecting the event and none at the time of the event. The cloud reflectivity data of Fig. 5.15 show that at the time of this event an extensive cloud was over head that was not moving much. The shower passed through the edge of the cloud with an active core in close vicinity.

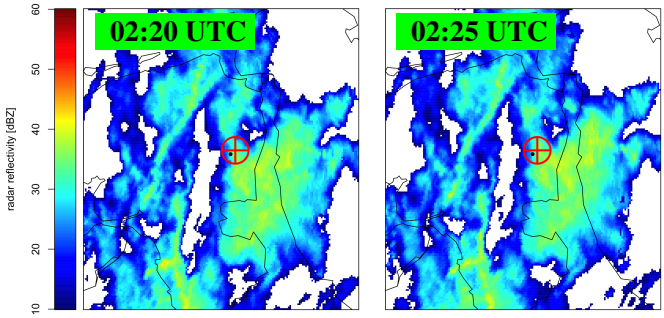

Fig. 5.15 The red ⊕ marks the location of the LOFAR 'Superterp'. Event 5 was measured at 02:20:21 UTC.

Event 5 - 81138021

Sim. III is chosen to be the best fit since both the reduced χ^2 and the ratio f are smallest.

Calculation	I			**II**			III		
Energy (eV)	3.4×10^{16}			$\mathbf{2.0 \times 10^{16}}$			1.4×10^{16}		
Layer	1	2	3	**1**	**2**	**3**	1	2	3
h (km)	6.2	5.6	3.0	**7.2**	**5.6**	**3.2**	7.4	5.4	3.1
E (kV/m)	76	87	17	**72**	**87**	**13**	92	93	13
α (°)	-59	-106	-176	**-43**	**-108**	**-175**	-39	-105	-174
$X_{\max}$ (g/cm^2)	523			**585**			657		
$X_{\max}$ (km)	$\equiv 6.0$			$\equiv$ **5.1**			$\equiv 4.3$		
χ^2_{3D}	0.93			**0.96**			0.99		
χ^2_C	1.29			**0.98**			1.02		
f	8.9			**5.5**			10.0		

Table 5.7 The values of the fit parameters and the results obtained by MGMR3D and CoREAS for event 5.

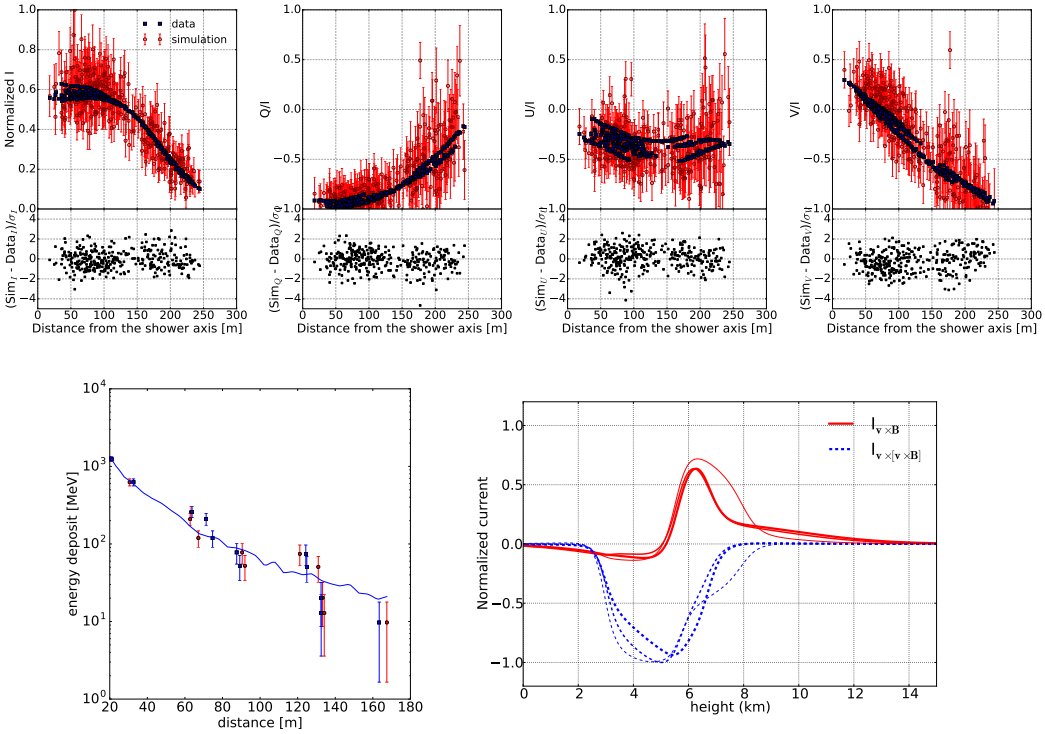

Fig. 5.16 Same as Fig. 5.12 but for event 5 where simulation II is selected. The core position was moved by 9 m from the original location determined from the LORA data.

Appendix 5.D August 26th, 2012

During the time of of detecting events 6, 7, and 8 there was some lightning activity observed by the the Météorage lightning detection network in the close vicinity of the Superterp, see Fig. 5.17. All three events occurred within a time span of 36 minutes, however the cloud reflectivity images, Fig. 5.18, clearly show that while events 6 and 7 passed through different sides of the same cloud, event 8 passed through a different one. The clouds were moving rather fast from west to east.

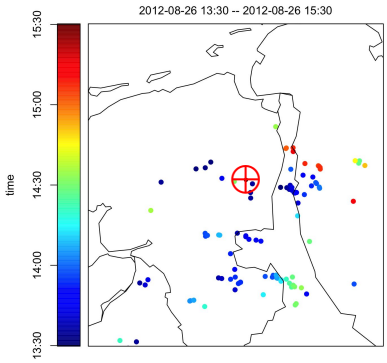

Fig. 5.17 Lightning discharges on 26/08/2012 between 13:30 and 15:00 UTC. The red ⊕ gives the location of LOFAR 'Superterp'. There were three events measured on this day. Event 6 was measured at 13:52:23 UTC, event 7 at 14:02:56 UTC, and event 8 at 14:28:19 UTC.

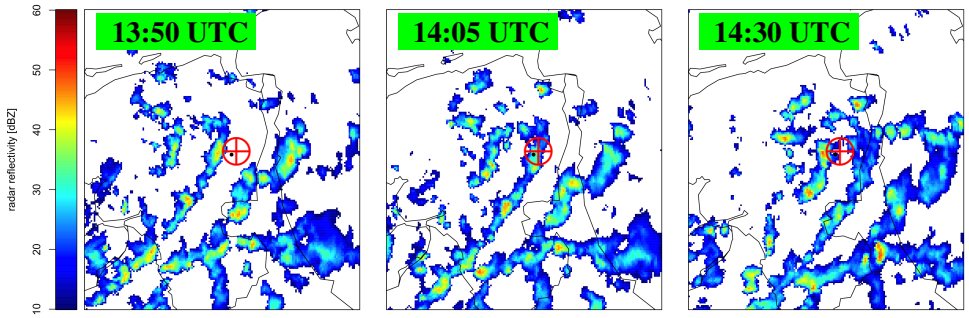

Fig. 5.18 The red ⊕ in the center marks the location of the LOFAR 'Superterp'. There were 3 events measured on this day. Event 6 was measured at 13:52:23 UTC, event 7 at 14:02:56 UTC, and event 8 at 14:28:19 UTC.

Event 6 - 83685143

The amount of circular polarization V/I is very small since the electric field in the bottom layer is very small and thus there is no rotation of the current. Sim. III is the best fit since the reduced χ^2 value and the ratio f are smallest.

Calculation	I		**II**		III	
Energy (eV)	5.7×10^{16}		$\mathbf{4.3 \times 10^{16}}$		3.0×10^{16}	
Layer	1	2	**1**	**2**	1	2
h (km)	8.0	3.8	**7.8**	**3.7**	7.8	3.8
E (kV/m)	93	3	**90**	**7**	89	7
α (°)	-63	-150	**-58**	**-178**	-60	-169
$X_{\max}$ (g/cm^2)	517		**602**		659	
$X_{\max}$ (km)	$\equiv 6.1$		$\equiv$ **5.0**		$\equiv 4.3$	
χ^2_{3D}	1.47		**1.57**		1.51	
χ^2_C	1.97		**1.44**		1.94	
f	2.8		**2.5**		7.0	

Table 5.8 The values of the fit parameters and the results obtained by MGMR3D and CoREAS for event 6.

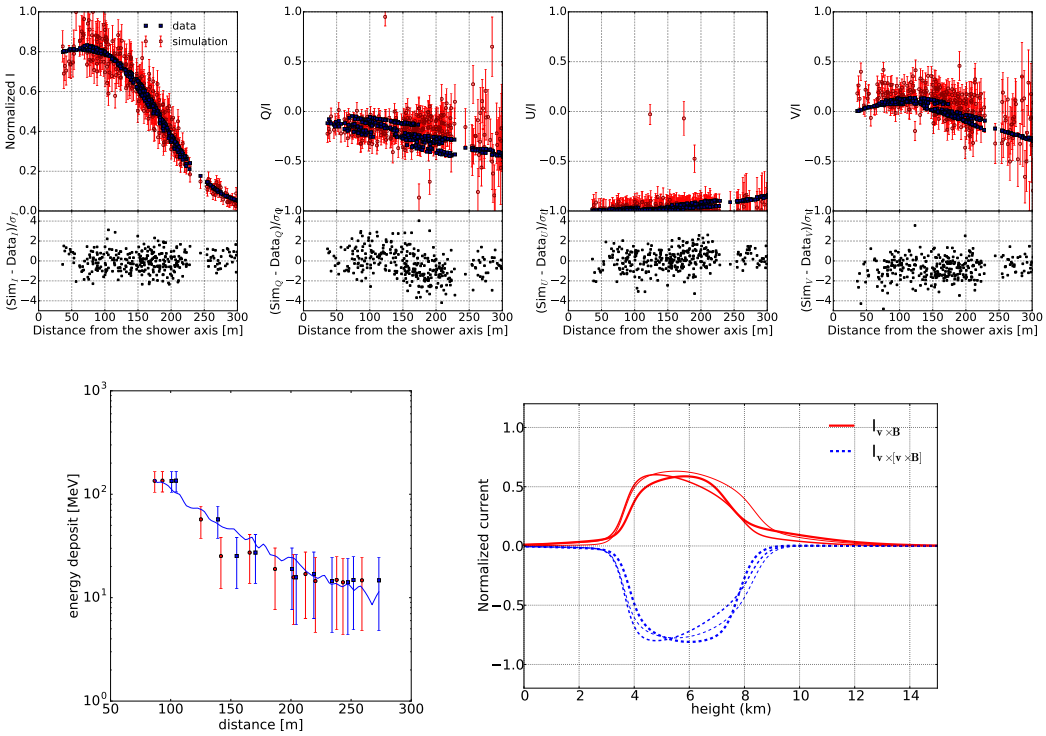

Fig. 5.19 Same as Fig. 5.12 but for event 6 where simulation II is selected. The core position was moved by 15 m from the original location determined from the LORA data.

Event 7 - 83685776

Sim. I is the best fit because both values of the reduced χ^2 and the ratio f are smallest.

Calculation	**I**			II			III		
Energy (eV)	$\mathbf{5.5 \times 10^{16}}$			3.5×10^{16}			2.0×10^{16}		
Layer	**1**	**2**	**3**	1	2	3	1	2	3
h (km)	**7.3**	**3.6**	**1.7**	7.3	3.5	1.7	7.5	3.4	1.7
E (kV/m)	**13**	**106**	**26**	25	104	20	31	107	20
α (°)	**-35**	**180**	**24**	-31	179	20	-31	177	11
$X_{\max}$ (g/cm^2)	**550**			650			730		
$X_{\max}$ (km)	$\equiv$ **5.4**			$\equiv 4.1$			$\equiv 3.2$		
χ^2_{3D}	**2.82**			2.29			2.34		
χ^2_C	**1.92**			1.95			2.29		
f	**4.9**			5.7			10.0		

Table 5.9 The values of the fit parameters and the results obtained by MGMR3D and CoREAS for event 7.

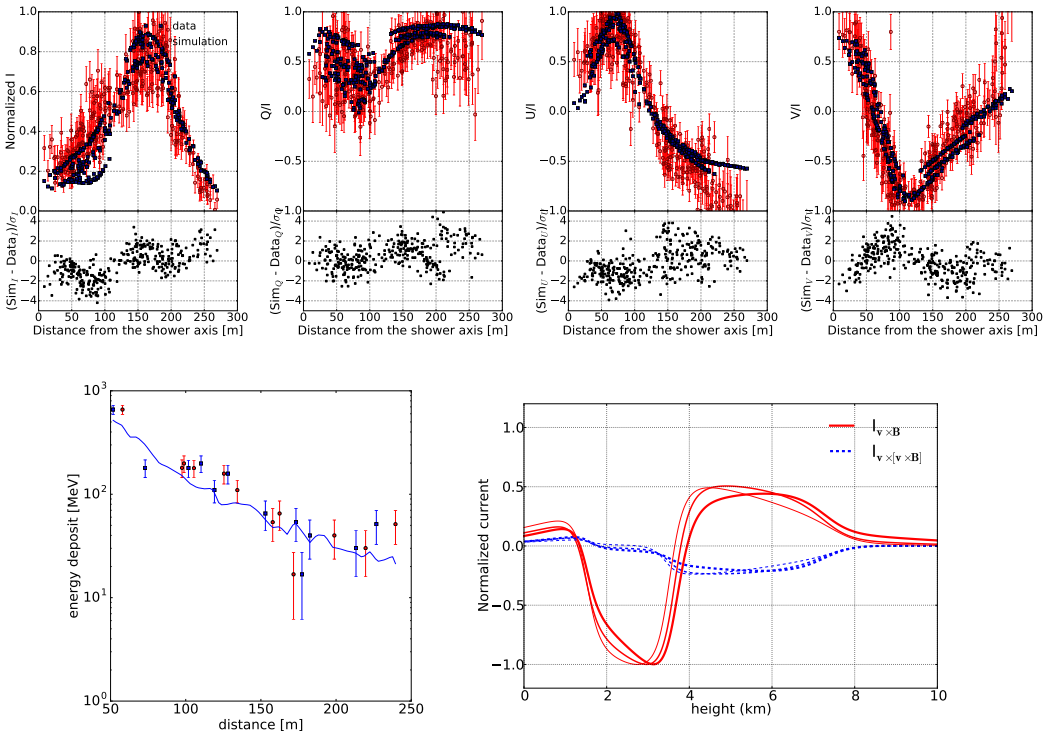

Fig. 5.20 Same as Fig. 5.12 but for event 7 where simulation I is selected. The core position was moved by 31 m from the original location determined from the LORA data.

Event 8 - 83687299

Sim. I is the best fit since the reduced χ^2 is smallest and the ratio f is unity.

Calculation	**I**			II			III		
Energy (eV)	$\mathbf{1.2 \times 10^{17}}$			1.0×10^{17}			5.0×10^{16}		
Layer	**1**	**2**	**3**	1	2	3	1	2	3
h (km)	**8.0**	**6.9**	**2.7**	7.9	6.7	2.8	8.0	6.8	2.7
E (kV/m)	**50**	**20**	**18**	49	24	21	49	28	15
α ($^\circ$)	**-78**	**-104**	**67**	-76	-106	62	-75	-104	63
$X_{\max}$ (g/cm^2)	**628**			656			750		
$X_{\max}$ (km)	$\equiv$ **4.7**			$\equiv$ 4.4			$\equiv$ 3.4		
χ^2_{3D}	**3.42**			3.37			3.52		
χ^2_C	**2.60**			2.86			4.64		
f	**1.0**			2.1			9.0		

Table 5.10 The values of the fit parameters and the results obtained by MGMR3D and CoREAS for event 8.

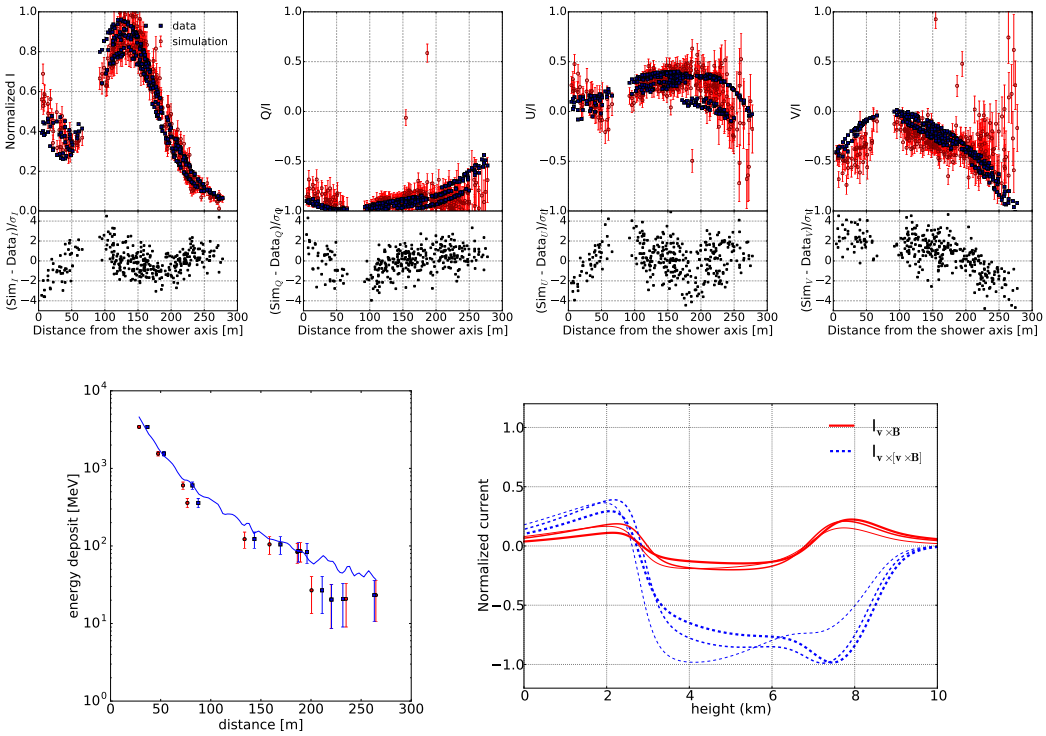

Fig. 5.21 Same as Fig. 5.12 but for event 8 where simulation I is selected. The core position was moved by 13 m from the original location determined from the LORA data.

Appendix 5.E December 30th, 2012

At the time of detection of event 9 the nearest lightning activity detected at a distance of 100 km, see Fig. 5.22. The cloud reflection images, Fig. 5.23, show that the clouds move fast from West to East and that at the shower must have passed right through the edge of an active cloud cell.

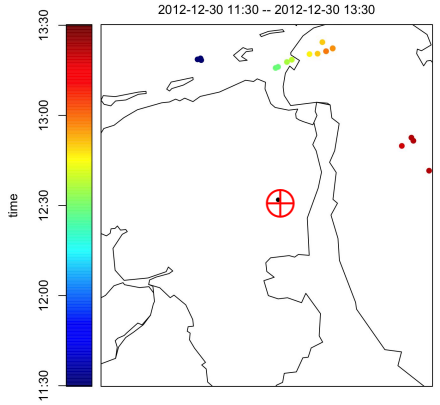

Fig. 5.22 Lightning discharges on 30/12/2012. The red ⊕ is the location of LOFAR 'Superterp'. Event 9 was measured at 12:38:37 UTC.

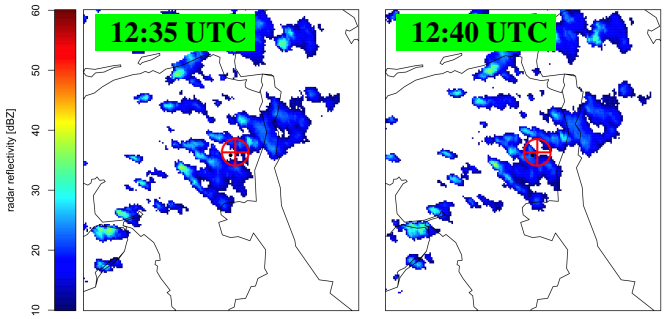

Fig. 5.23 The red ⊕ marks the location of the LOFAR 'Superterp'. Event 9 was measured at 12:38:37 UTC.

Event 9 - 94567117

Sim. III is the best fit since the reduced χ^2 is smallest and the ratio f is unity.

Calculation	I			II			**III**		
Energy (eV)	1.2×10^{17}			7.5×10^{16}			$\mathbf{7.0 \times 10^{16}}$		
Layer	1	2	3	1	2	3	**1**	**2**	**3**
h (km)	8.5	4.8	2.1	8.2	4.6	2.1	**8.0**	**5.0**	**2.0**
E (kV/m)	12	48	45	15	20	45	**50**	**15**	**9**
α (°)	103	108	15	44	108	12	**98**	**98**	**8**
$X_{\max}$ (g/cm^2)	670			743			**773**		
$X_{\max}$ (km)	$\equiv 3.8$			$\equiv 3.0$			$\equiv$ **2.7**		
χ^2_{3D}	3.82			3.63			**3.65**		
χ^2_C	5.60			4.21			**3.50**		
f	2.7			1.5			**1.0**		

Table 5.11 The values of the fit parameters and the results obtained by MGMR3D and CoREAS for event 9.

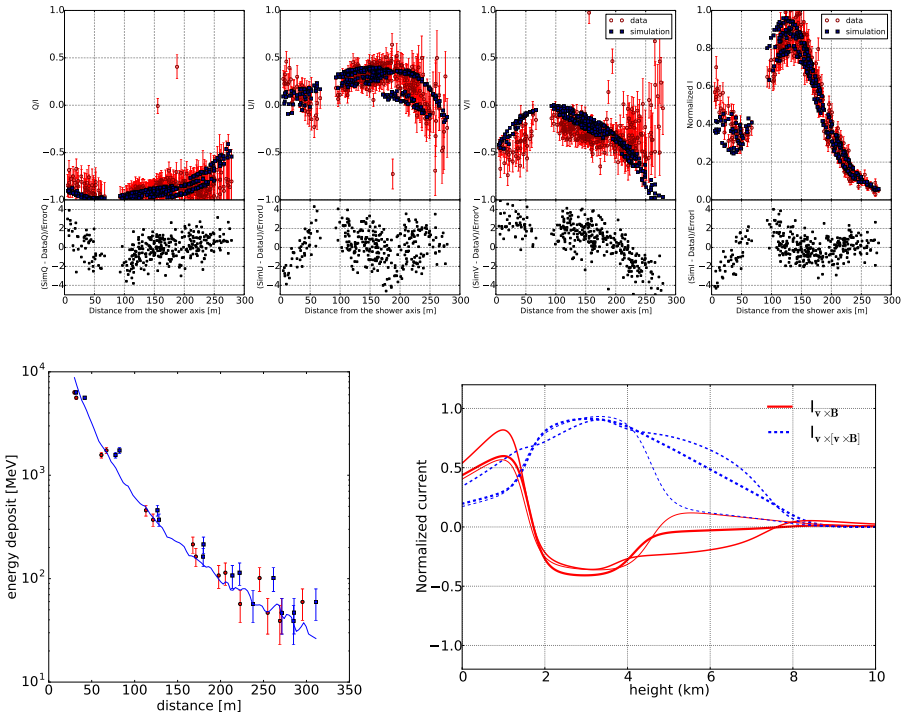

Fig. 5.24 Same as Fig. 5.12 but for event 9 where simulation III is selected. The core position was moved by 17 m from the original location determined from the LORA data.

Appendix 5.F July 26th, 2013

Considerable lightning activity was observed in the vicinity of the core at the time of detection of event 10, see Fig. 5.25. The cloud reflectivity data shown in Fig. 5.26 indicate much higher values than seen for most of the other cases as would be consistent with this being a real thundercloud with lightning activity. The shower passed very close to the most active region.

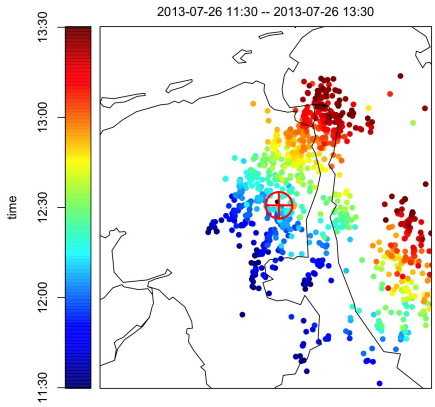

Fig. 5.25 Lightning discharges on 26/07/2013. The red ⊕ is the location of LOFAR 'Superterp'. Event #10 was measured at 12:17:26 UTC.

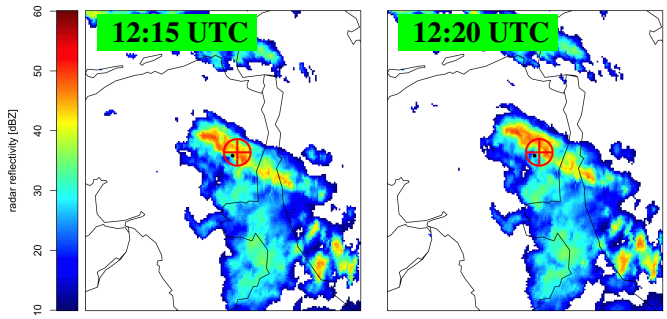

Fig. 5.26 The red ⊕ marks the location of the LOFAR 'Superterp'. Event 10 was measured at 12:17:26 UTC.

Event 10 - 112537046

Sim. I is the best fit since both the reduced χ^2 and the ratio f are smallest.

Calculation	**I**			II			III		
Energy (eV)	$\mathbf{9.4 \times 10^{16}}$			4.2×10^{16}			2.6×10^{16}		
Layer	**1**	**2**	**3**	1	2	3	1	2	3
h (km)	**7.6**	**4.9**	**3.6**	7.1	5.0	3.4	7.3	4.9	3.4
E (kV/m)	**28**	**90**	**44**	97	93	32	97	57	22
α (°)	**92**	**-110**	**-147**	71	-115	-145	69	-116	-145
$X_{\max}$ (g/cm^2)	**505**			630			753		
$X_{\max}$ (km)	$\equiv$ **5.9**			$\equiv$ 4.3			$\equiv$ 2.9		
χ^2_{3D}	**1.56**			1.65			1.58		
χ^2_C	**1.96**			2.10			3.07		
f	**4.0**			7.8			40.0		

Table 5.12 The values of the fit parameters and the results obtained by MGMR3D and CoREAS for event 10.

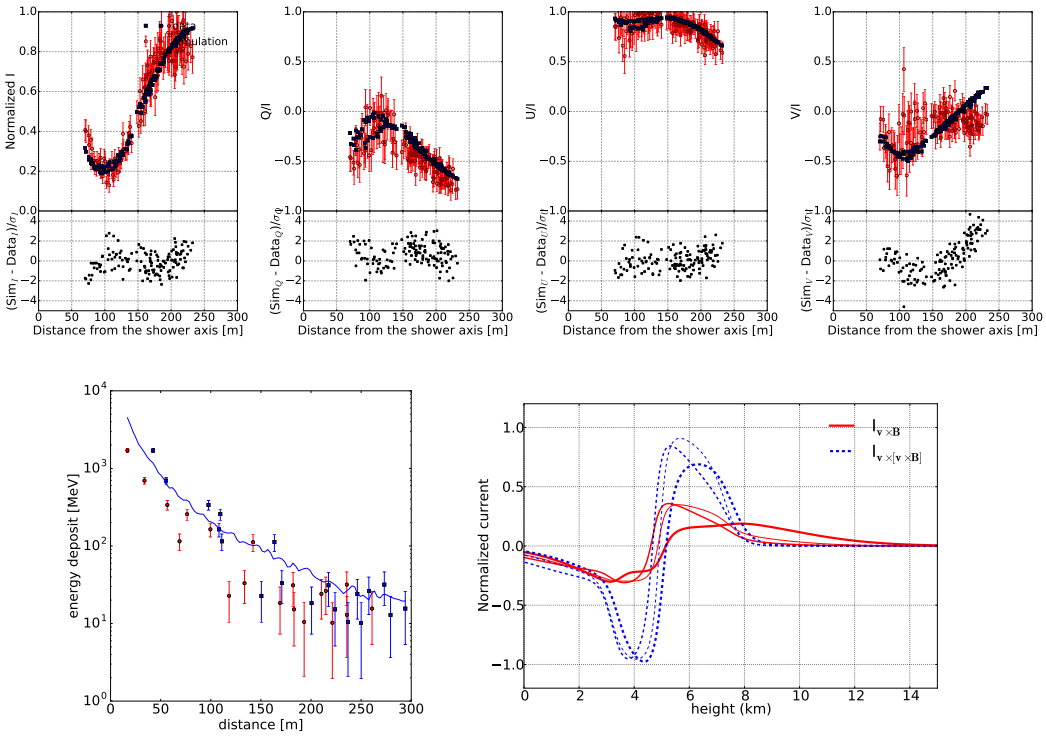

Fig. 5.27 Same as Fig. 5.12 but for event 10 where simulation I is selected. The core position was moved by 44 m from the original location determined from the LORA data.

Appendix 5.G June 27th, 2014

Fig. 5.28 shows that there is lightning activity observed close to the core and at about the time of observing event 11. Comparing this with the cloud reflectivity data, Fig. 5.29, indicates that at the lime of recording this event the active cell was still only approaching the Superterp and still at a distance of about 50 km to the South-West. The rim of the thundercloud was just over the Superterp.

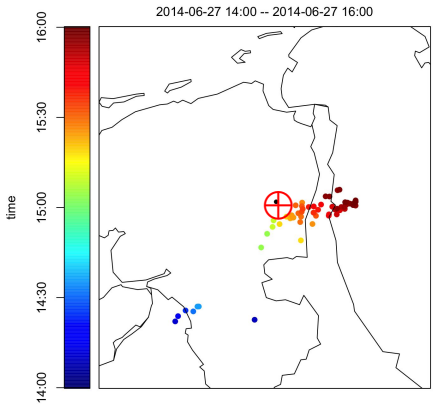

Fig. 5.28 Lightning discharges on 27/06/2014. The black star gives the location of the LOFAR 'Superterp'. Event 11 was measured at 14:44:03 UTC.

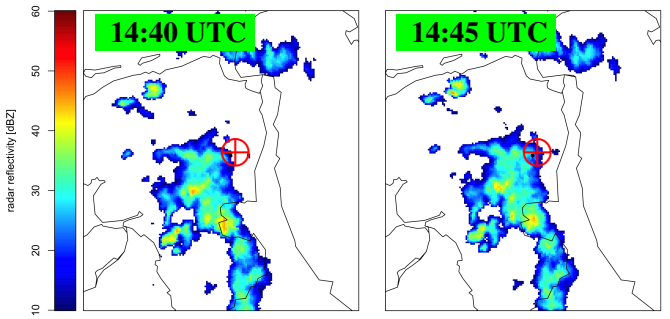

Fig. 5.29 The red ⊕ marks the location of the LOFAR 'Superterp'. Event 11 was measured at 14:44:03 UTC.

Event 11 - 141576243

Sim. II is the best fit because the reduced χ^2 value is smallest and the ratio f is unity. The reduced χ^2 values obtained by CoREAS is larger than that in MGMR3D because of the particle fit. The left bottom panel of Fig. 5.26 shows that the particle fit is rather good, but there is one point at about 50 m which cannot be fitted. We have checked the LORA signal of this point and seen that the noise level is significantly large in this detector, so this data point is not reliable. As discussed in Section 5.5, there were lightning activity overhead LOFAR at the time when this event was measured. Thus, this could be that the LORA detectors have been affected by the lightning. These effects has been observed by the surface detector of the Pierre Auger Observatory [100].

Calculation	I			**II**			III		
Energy (eV)	6.8×10^{16}			$\mathbf{4.8 \times 10^{16}}$			3.6×10^{16}		
Layer	1	2	3	**1**	**2**	**3**	1	2	3
h (km)	6.1	4.2	2.9	**6.3**	**4.5**	**3.3**	6.1	3.9	3.0
E (kV/m)	30	38	5	**50**	**49**	**5**	54	29	3
α (°)	36	-27	-124	**43**	**-21**	**-109**	43	-22	-142
$X_{\max}$ (g/cm^2)	522			**618**			711		
$X_{\max}$ (km)	$\equiv 5.7$			$\equiv$ **4.4**			$\equiv 3.3$		
χ^2_{3D}	1.33			**1.30**			1.39		
χ^2_C	3.45			**2.97**			3.56		
f	1.2			**1.0**			2.3		

Table 5.13 The values of the fit parameters and the results obtained by MGMR3D and CoREAS for event 11.

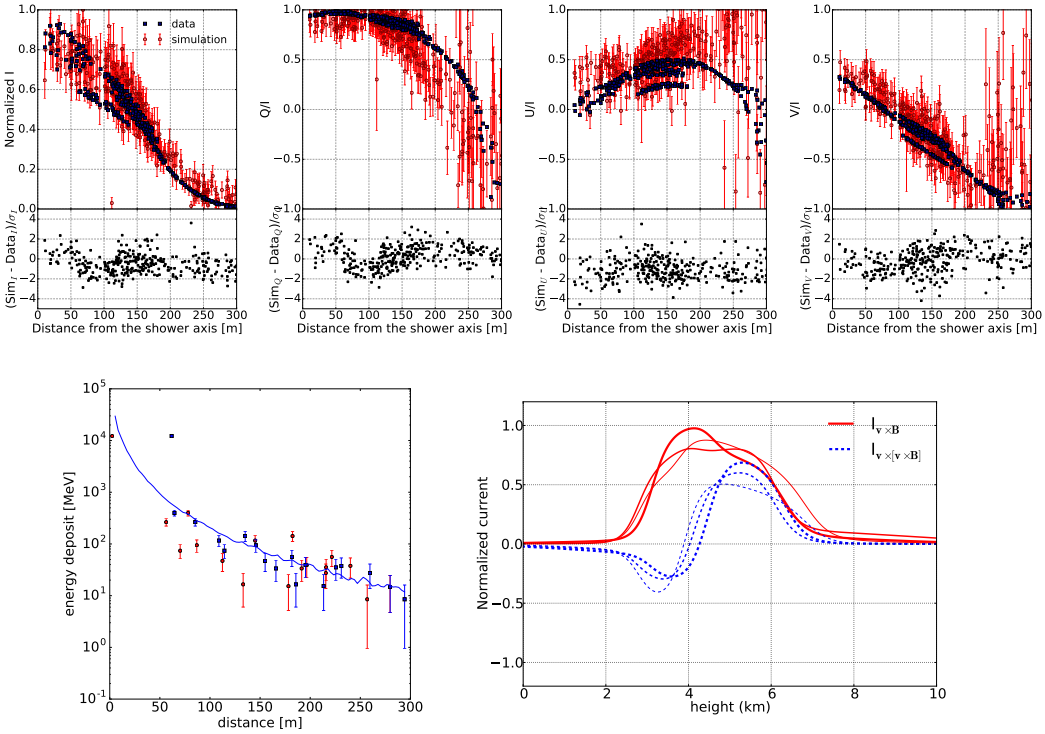

Fig. 5.30 Same as Fig. 5.12 but for event 11 where simulation II is selected. The core position was moved by 61 m from the original location determined from the LORA data.

Chapter 6

Outlook

The development of a non-intrusive method to probe atmospheric electric fields during thunderstorm conditions has been described in this thesis. As discussed in the thesis, strong atmospheric electric fields significantly influence radio emission from extensive air showers. These effects have been observed at LOFAR. We see differences between thunderstorm events and fair-weather events. Thunderstorm events can thus be used to determine the electric fields along the shower axis. In order to probe the electric fields, we fit both intensity patterns and polarization signatures. We have used our technique to analyze thunderstorm events measured at LOFAR during the period between December 2011 and August 2014. We find that using the three-layer model of the electric fields, we can reconstruct the intensity patterns and the polarization signatures of all thunderstorm events which we have analyzed rather well. We also find interesting features of the electric fields and charge structure in thunderclouds as discussed in the thesis.

However, further work is still needed to confirm our findings and to fully understand the charge distribution in the thunderclouds. Among 11 thunderstorm events which we have analyzed, we found seven thunderstorm events that showed an electric field with a traditional triple layer structure. However, we do not know the charge polarity of each layer. Since LOFAR is not sensitive to the electric field component parallel to the shower axis, it is hard to determine vertical components of the electric fields and thus the charge polarity is unknown. There are several ways to determine the charge polarity. One way to derive the vertical components of the electric fields

and the charge polarity is to have some thunderstorm events measured close in time and the electric field of the region where these thunderstorm events pass through has not changed yet. If this is the case, we are able to derive the vertical component and thus the total electric field as discussed in the thesis. To increase this probability, one can increase the trigger rate and thus one can measure more events. At present, an air shower is recorded if there are at least 12 LORA detectors triggered. This keeps the trigger rate around one event per hour. If the minimum number of LORA detectors triggered is reduced to 9, we can record two events per hour [101]. Increasing the trigger rate, one can record more air showers which have smaller primary energies. For fair-weather cases, these low-energy events are not helpful since their radio signals are dominated by noise. However, during thunderstorm conditions, the intensity of the radio emission is significantly enhanced due to the strong electric fields. Therefore, the radio intensity of thunderstorm events is still much larger than the noise level although the primary energy of these events could be small. Another way to determine the charge polarity is using the data from the electric field meter. This meter has been installed at LOFAR to measure the vertical electric field component near the ground. It can be used to determine the charge polarity of the bottom layer in thunderclouds in the summer. In the winter, the meter may not help to determine the charge polarity because there might be a charge layer at low altitudes near the ground which our technique is not sensitive to. In addition, as a long-term work, antennas sensitive to a lower frequency band $2-9$ MHz can be installed to measure the vertical component of the electric fields. As shown in this thesis, the effects of the parallel components of the electric fields as well as the influence of the perpendicular electric fields stronger than about 50 kV/m can be observed in the frequency band between 2 MHz to 9 MHz. Installing these lower-frequency antennas would help to extract more information about the direction as well as the magnitude of the electric fields. As has been shown in the thesis, the intensity patterns at these frequencies show a much more gradual fall-off with distance than those in the frequency domain from 30 MHz to 80 MHz; thus we need a less dense antenna array.

For all thunderstorm events which we have analyzed, we found that the electric fields between the lower charge layer and the ground are smaller than those inside the thunderclouds. Analyzing more thunderstorm events would help to confirm this finding. Since clouds are at lower altitudes in the winter and our technique

is not sensitive to heights lower than 1 km, it would be good to analyze more thunderstorm events in the summer. For the whole Netherlands which has an area of about 41000 km^2 [102], the number of thunderstorm days per year is about 20 [103]. Multicell thunderstorms, the most common type of thunderstorms, are usually large, about 100 km in diameter. They move with an average speed of about 50 km/h and last on average for 2 hours. For these reasons, at the LOFAR core, there could be at most 20 thunderclouds passing by during the whole year. Since winter thunderstorms are much rarer than summer thunderstorms, the number of summer thunderstorms at LOFAR could be about 15 per year. For a thunderstorm lasting for about 2 hours, LORA could trigger 2 events if it works well. So, there would be about 30 thunderstorm air showers recorded every year. Therefore, it can be predicted that to record about 100 summer thunderstorm events will take about 3.5 years. In order to reduce the time of measurement, one can increase the trigger rate to record more events as discussed above. If the minimum number of LORA detectors triggered is reduced to 9, one could record 100 summer thunderstorm events in 21 months. In Chapter 5, we have shown that events could occur under non-thunderstorm conditions in which the atmospheric electric fields were strong but there was no lightning activitity. Therefore, the time to record 100 summer thunderstorm events can be reduced roughly to 21 months for the present trigger condition and to about 10 months for the trigger condition of 9.

To be able to analyze a large number of thunderstorm events, it would be better to automatize the fitting procedure. This can be done potentially although there are some difficulties. As discussed in the thesis, in thunderstorm events, it is difficult to fit the core position automatically as it has been done in fair-weather events. At present, this step has to be done manually before starting the fitting procedure. It can be automatized by assuming that the core is at the position such that there should be a smooth dependence of all Stokes parameters and particle density as a function of distance to the shower axis. Moreover, since the fit parameters are not linearly independent, fits are not always converging. Hence, the fits can be stuck in a local minimum. If this happens, we change the value of one fit parameters in order to leave the local minimum and continue to run the fit. This step is done manually, but it needs to be automatized in the future. In addition, on the basis of the Stokes parameters, there are two possible current profiles which can fit: a current profile

and its inverted structure. In order to choose the correct one, we need to check the polarity of the pulses in some antennas. At present, this step is done manually, but it can be done automatically. One can find which of the pulses generated by the current structures reproduces the data best.

Since our technique is new, it is useful to verify our results. This can be done by comparing with the results from other measurements. For example, based on the changes of the electric fields extracted from thunderstorm events, we can determine the heights of charge layers in thunderclouds. It is useful to compare the heights of charge layers extracted from our analysis with the top and bottom heights of clouds from KNMI data. This may also help to confirm if there are any charge layers at low altitudes which we are not sensitive to for the winter thunderstorm events. In addition, for the thunderstorm events which we have analyzed, we have checked if there was any lightning activity at the LOFAR core right before or after the time when thunderstorm events were measured. However, within a time interval of 5 s, we have not observed a coincidence between a cosmic ray event and a lighting stroke. The reason could be that at the time these thunderstorm events were measured, coverage of lightning detection networks was not sufficient. For the Earth Network, the number of sensors which can detect lightning flashes at the LOFAR core and its vicinity has been increased from the two that were located at a distance of about 390 km from the 'Superterp' [104]. Nowadays, four new stations within a distance of 200 km from the 'Superterp' have been installed. Therefore, the cross-checking with the lightning network data is useful to repeat for data which have been taken recently and which will be recorded in the future.

The study in this thesis offers valuable insights into the electric fields and charge structure in clouds by using LOFAR. In addition, LOFAR can also be used as a lightning mapping array to map lightning flash in 3D. These new abilities makes LOFAR a good device for understanding more about the mystery of lightning.

References

[1] "CORSIKA webpage." https://www.ikp.kit.edu/corsika/.

[2] "Pictures and Posters on ASTRON's website." https://www.astron.nl/about-astron/press-public/pictures/pictures#Pictures_LOFAR.

[3] "The Nobel Prize in Physics 1903." https://www.nobelprize.org/nobel_prizes/physics/laureates/1903.

[4] V. F. Hess, "Durchdringenden Strahlung bei sieben Freiballonfahrten," *Physikalische Zeitschrift*, vol. 13, pp. 1084–1091, 1912.

[5] J. R. Hörandel, "Models of the knee in the energy spectrum of cosmic rays," *Astroparticle Physics*, vol. 21, pp. 241 – 265, 2004.

[6] T. Wibig and A. W. Wolfendale, "At what particle energy do extragalactic cosmic rays start to predominate?," *Journal of Physics G: Nuclear and Particle Physics*, vol. 31, p. 255, 2005.

[7] A. M. Hillas, "Can diffusive shock acceleration in supernova remnants account for high-energy galactic cosmic rays?," *Journal of Physics G: Nuclear and Particle Physics*, vol. 31, p. R95, 2005.

[8] J. Blümer, R. Engel, and J. R. Hörandel, "Cosmic rays from the knee to the highest energies," *Progress in Particle and Nuclear Physics*, vol. 63, pp. 293 – 338, 2009.

[9] P. Auger, P. Ehrenfest, R. Maze, J. Daudin, and R. A. Fréon, "Extensive Cosmic-Ray Showers," *Reviews of Modern Physics*, vol. 11, pp. 288–291, 1939.

[10] P. Schellart, *Measuring Radio Emission from Air Showers*. PhD Thesis, Radboud University Nijmegen, The Netherlands, 2015.

[11] D. Heck *et al.*, *CORSIKA: a Monte Carlo code to simulate extensive air showers. Report FZKA 6019*. 1998.

[12] P. Hansen, J. Alvarez-Muñiz, and R. Vázquez, "A comprehensive study of shower to shower fluctuations," *Astroparticle Physics*, vol. 34, pp. 503 – 512, 2011.

[13] M. Ludwig *et al.*, "A detailed comparison of REAS3 and MGMR simulations for radio emission from EAS," no. arXiv:1202.3352, 2012, arXiv:1202.3352.

[14] J. V. Jelley and other, "Radio pulses from extensive air showers," *Nature*, 1965.

[15] H. R. Allan, "Low Frequency Radio Emission from Extensive Air Showers," *Nature*, vol. 237, pp. 384 – 385, 1972.

[16] D. J. FEGAN and D. M. JENNINGS, "UHF Radio Pulses from the Zenith associated with Extensive Air Showers," *Nature*, 1969.

[17] H. Falcke *et al.*, "Detection and imaging of atmospheric radio flashes from cosmic ray air showers," *Nature*, vol. 435, pp. 313–316, 2005.

[18] W. Apel *et al.*, "Progress in air shower radio measurements: Detection of distant events," *Astroparticle Physics*, vol. 26, pp. 332 – 340, 2006.

[19] D. Ardouin *et al.*, "Radioelectric field features of extensive air showers observed with CODALEMA," *Astroparticle Physics*, vol. 26, pp. 341 – 350, 2006.

[20] D. Ardouin *et al.*, "Geomagnetic origin of the radio emission from cosmic ray induced air showers observed by CODALEMA," *Astroparticle Physics*, vol. 31, pp. 192 – 200, 2009.

[21] F. Schröder *et al.*, "Tunka-Rex: a Radio Antenna Array for the Tunka Experiment," *AIP Conference Proceedings*, vol. 1535, 2013.

[22] J. Kelley and P. Auger, "AERA: The auger engineering radio array," *Proceedings of the 32nd International Cosmic Ray Conference, ICRC 2011*, vol. 3, pp. 112–115, 2011.

[23] M. P. van Haarlem *et al.*, "LOFAR: The LOw-Frequency ARray," *Astronomy & Astrophysics*, vol. 556, p. A2, 2013.

[24] G. Askaryan, "Excess Negative Charge of the Electron-Photon Shower and Coherent Radiation Originating from It. Radio Recording of Showers under the Ground and on the Moon," *The Physical Society of Japan*, vol. Vol: 17, Suppl. A-III, 1962.

[25] F. D. Kahn and I. Lerche, "Radiation from Cosmic Ray Air Showers," *Royal Society of London Proceedings Series A*, vol. 289, pp. 206–213, 1966.

[26] J. Alvarez-Muñiz, W. R. Carvalho, and E. Zas, "Monte Carlo simulations of radio pulses in atmospheric showers using ZHAireS," *Astroparticle Physics*, vol. 35, pp. 325 – 341, 2012.

[27] K. D. de Vries, A. M. van den Berg, O. Scholten, and K. Werner, "Coherent Cherenkov Radiation from Cosmic-Ray-Induced Air Showers," *Physical Review Letter*, vol. 107, p. 061101, 2011.

[28] K. Werner, K. D. de Vries, and O. Scholten, "A realistic treatment of geomagnetic Cherenkov radiation from cosmic ray air showers," *Astroparticle Physics*, vol. 37, no. Supplement C, pp. 5 – 16, 2012.

[29] T. Huege, M. Ludwig, and C. W. James, "Simulating radio emission from air showers with CoREAS," *AIP Conference Proceedings*, vol. 1535, pp. 128–132, 2013.

[30] J. Alvarez-Muñiz, W. R. C. Jr., and E. Zas, "Monte Carlo simulations of radio pulses in atmospheric showers using ZHAireS," *Astroparticle Physics*, vol. 35, pp. 325 – 341, 2012.

[31] O. Scholten, K. Werner, and F. Rusydi, "A macroscopic description of coherent geo-magnetic radiation from cosmic-ray air showers," *Astroparticle Physics*, vol. 29, pp. 94 – 103, 2008.

[32] K. Werner, K. D. de Vries, and O. Scholten, "A realistic treatment of geomagnetic Cherenkov radiation from cosmic ray air showers," *Astroparticle Physics*, vol. 37, pp. 5 – 16, 2012.

[33] O. Scholten, T. N. G. Trinh, K. D. de Vries, and B. M. Hare, "Analytic calculation of radio emission from parametrized extensive air showers: A tool to extract shower parameters," *Physical Review D*, vol. 97, p. 023005, Jan 2018.

[34] T. Huege, "Theory and simulations of air shower radio emission," *AIP Conference Proceedings*, vol. 1535, pp. 121–127, 2013.

[35] A. Nelles *et al.*, "Measuring a Cherenkov ring in the radio emission from air showers at 110–190 MHz with LOFAR," *Astroparticle Physics*, vol. 65, pp. 11 – 21, 2015.

[36] Schellart, P. *et al.*, "Detecting cosmic rays with the LOFAR radio telescope," *Astronomy & Astrophysics*, vol. 560, p. A98, 2013.

[37] P. Schellart *et al.*, "Polarized radio emission from extensive air showers measured with LOFAR," *Journal of Cosmology and Astroparticle Physics*, vol. 2014, p. 014, 2014.

[38] V. A. Rakov and M. A. Uman, *Lightning: Physics and Effects*. Cambridge University Press, 2007.

[39] P. R. Krehbiel, M. Brook, and R. A. McCrory, "An analysis of the charge structure of lightning discharges to ground," *Journal of Geophysical Research: Oceans*, vol. 84, pp. 2432–2456, 1979.

[40] P. Krehbiel, "The Earth's electrical environment," *The Electrical Structure of Thunderstorms*, pp. 90–113, 1986.

[41] J. R. Dwyer and M. A. Uman, "The physics of lightning," *Physics Reports*, vol. 534, pp. 147 – 241, 2014. The Physics of Lightning.

[42] J. T. Pilkey *et al.*, "Rocket triggered lightning propagation paths relative to preceding natural lightning activity and inferred cloud charge," vol. 119, pp. 13,427–13,456, 2014. 2014JD022139.

[43] W. D. Rust *et al.*, "Inverted-polarity electrical structures in thunderstorms in the Severe Thunderstorm Electrification and Precipitation Study (STEPS)," *Atmospheric Research*, vol. 76, pp. 247 – 271, 2005. Atmospheric Electricity.

[44] "Lightning." https://www.britannica.com/science/lightning-meteorology.

[45] G. Grenet, "Le nuage d'orage: machine el' ctrostatique," *Meteorology*, vol. 3, pp. 306–307, 1947.

[46] B. Vonnegut, *Possible mechanism for the formation of thunderstorm electricity*. Bulletin of the American Meteorological Society, 1953.

[47] D. MacGorman and W. Rust, *The Electrical Nature of Thunderstorms*. New York: Oxford University Press, 1998.

[48] T. Takahashi, "Riming electrification as a charge generation mechanism in thunderstorms," *Journal of the Atmospheric Sciences*, vol. 35, pp. 1536–1548, 1978.

[49] W. Gaskell and A. J. Illingworth, "Charge transfer accompanying individual collisions between ice particles and its role in thunderstorm electrification," *Quarterly Journal of the Royal Meteorological Society*, vol. 106, pp. 841–854, 1980.

[50] E. R. Jayaratne, C. P. R. Saunders, and J. Hallett, "Laboratory studies of the charging of soft-hail during ice crystal interactions," *Quarterly Journal of the Royal Meteorological Society*, vol. 109, pp. 609–630, 1983.

[51] E. R. Jayaratne and C. P. R. Saunders, "The "rain gush", lightning, and the lower positive charge center in thunderstorms," *Journal of Geophysical Research: Atmospheres*, vol. 89, pp. 11816–11818, 1984.

[52] P. Berdeklis and R. List, "The Ice Crystal–Graupel Collision Charging Mechanism of Thunderstorm Electrification," *Journal of the Atmospheric Sciences*, vol. 58, pp. 2751–2770, 2001.

[53] T. C. Marshall, M. P. McCarthy, and W. D. Rust, "Electric field magnitudes and lightning initiation in thunderstorms," *Journal of Geophysical Research: Atmospheres*, vol. 100, pp. 7097–7103, 1995.

[54] T. C. Marshall *et al.*, "Rocket and balloon observations of electric field in two thunderstorms," *Journal of Geophysical Research: Atmospheres*, vol. 100, pp. 20815–20828, 1995.

[55] J. R. Dwyer, "A fundamental limit on electric fields in air," *Geophysical Research Letters*, vol. 30, 2003.

[56] T. C. Marshall *et al.*, "Observed electric fields associated with lightning initiation," *Geophysical Research Letters*, vol. 32, 2005.

[57] J. R. Dwyer, M. A. Uman, and H. K. Rassoul, "Remote measurements of thundercloud electrostatic fields," *Journal of Geophysical Research: Atmospheres (1984–2012)*, vol. 114, 2009.

[58] O. Scholten *et al.*, "Measurement of the circular polarization in radio emission from extensive air showers confirms emission mechanisms," *Physical Review D*, vol. 94, p. 103010, 2016.

[59] O. Scholten and K. Werner, "Macroscopic model of geomagnetic-radiation from air showers," *Nuclear Instruments and Methods in Physics Research Section A: Accelerators, Spectrometers, Detectors and Associated Equipment*, vol. 604, pp. S24 – S26, 2009. ARENA 2008.

[60] A. Aab *et al.*, "Probing the radio emission from air showers with polarization measurements," *Physical Review D*, vol. 89, p. 052002, 2014.

[61] S. Buitink *et al.*, "Method for high precision reconstruction of air shower $X_{\max}$ using two-dimensional radio intensity profiles," *Physical Review D*, vol. 90, p. 082003, 2014.

[62] A. Corstanje *et al.*, "The shape of the radio wavefront of extensive air showers as measured with LOFAR," *Astroparticle Physics*, vol. 61, pp. 22 – 31, 2015.

[63] T. Huege *et al.*, "The convergence of EAS radio emission models and a detailed comparison of REAS3 and MGMR simulations," *Nuclear Instruments and Methods in Physics Research Section A: Accelerators, Spectrometers, Detectors and Associated Equipment*, vol. 662, Supplement 1, pp. S179 – S186, 2012. 4th International workshop on Acoustic and Radio EeV Neutrino detection Activities.

[64] K. D. de Vries *et al.*, "The lateral distribution function of coherent radio emission from extensive air showers: Determining the chemical composition of cosmic rays," *Astroparticle Physics*, vol. 34, pp. 267 – 273, 2010.

[65] K. D. de Vries, O. Scholten, and K. Werner, "The air shower maximum probed by Cherenkov effects from radio emission," *Astroparticle Physics*, vol. 45, pp. 23 – 27, 2013.

[66] K. Werner, K. D. de Vries, and O. Scholten, "A realistic treatment of geomagnetic Cherenkov radiation from cosmic ray air showers," *Astroparticle Physics*, vol. 37, pp. 5 – 16, 2012.

[67] V. Marin and B. Revenu, "Simulation of radio emission from cosmic ray air shower with SELFAS2," *Astroparticle Physics*, vol. 35, pp. 733 – 741, 2012.

[68] S. Buitink *et al.*, "Amplified radio emission from cosmic ray air showers in thunderstorms," *Astronomy & Astrophysics*, vol. 467, pp. 385–394, 2007.

[69] W. Apel *et al.*, "Thunderstorm observations by air-shower radio antenna arrays," *Advances in Space Research*, vol. 48, pp. 1295 – 1303, 2011.

[70] S. Buitink *et al.*, "Simulation of radio emission from air showers in atmospheric electric fields," *Astroparticle Physics*, vol. 33, pp. 296 – 306, 2010.

[71] P. Schellart *et al.*, "Probing Atmospheric Electric Fields in Thunderstorms through Radio Emission from Cosmic-Ray-Induced Air Showers," *Physics Review Letter*, vol. 114, p. 165001, 2015.

[72] V. Venema, H. Russchenberg, A. Apituley, A. van Lammeren, and L. Ligthart, "Cloud boundary height measurements using lidar and radar," *Physics and Chemistry of the Earth, Part B: Hydrology, Oceans and Atmosphere*, vol. 25, pp. 129 – 134, 2000.

[73] M. Stolzenburg *et al.*, "Electric field values observed near lightning flash initiations," *Geophysical Research Letters*, vol. 34, 2007.

[74] S. Buitink *et al.*, "Monte Carlo simulations of air showers in atmospheric electric fields," *Astroparticle Physics*, vol. 33, pp. 1 – 12, 2010.

[75] C. Amsler *et al.*, "Review of Particle Physics," *Physics Letters B*, vol. 667, pp. 1 – 6, 2008.

[76] http://physics.nist.gov/PhysRefData/Star/Text/ESTAR.html.

[77] F. Nerling *et al.*, "Universality of electron distributions in high-energy air showers—Description of Cherenkov light production," *Astroparticle Physics*, vol. 24, pp. 421 – 437, 2006.

[78] S. Acounis *et al.*, "Results of a self-triggered prototype system for radio-detection of extensive air showers at the Pierre Auger Observatory," *Journal of Instrumentation*, vol. 7, p. P11023, 2012.

[79] A. Chilingarian, "Thunderstorm ground enhancements—Model and relation to lightning flashes," *Journal of Atmospheric and Solar-Terrestrial Physics*, vol. 107, pp. 68 – 76, 2014.

[80] A. Dubinova, C. Rutjes, U. Ebert, S. Buitink, O. Scholten, and G. T. N. Trinh, "Prediction of Lightning Inception by Large Ice Particles and Extensive Air Showers," *Physics Review Letter*, vol. 115, p. 015002, 2015.

[81] A. V. Gurevich and A. N. Karashtin, "Runaway Breakdown and Hydrometeors in Lightning Initiation," *Physics Review Letter*, vol. 110, p. 185005, 2013.

[82] S. Ostapchenko, "QGSJET-II: towards reliable description of very high energy hadronic interactions," *Nuclear Physics B Proceedings Supplements*, vol. 151, pp. 143–146, 2006.

[83] G. Battistoni *et al.*, "The FLUKA code: description and benchmarking," in *Hadronic Shower Simulition Workshop* (M. Albrow and R. Raja, eds.), vol. 896 of *American Institute of Physics Conference Series*, pp. 31–49, 2007.

[84] M. Kobal, "A thinning method using weight limitation for air-shower simulations," *Astroparticle Physics*, vol. 15, pp. 259 – 273, 2001.

[85] H. Allan and J. Jones, "Radio Pulses from Extensive Air Showers," *Nature*, vol. 212, pp. 129–131, 1966.

[86] A. Nelles, P. Schellart, *et al.*, "Measuring a Cherenkov ring in the radio emission from air showers at 110-190 MHz with LOFAR," *Astroparticle Physics*, vol. 65, pp. 11–21, 2015.

[87] K. D. de Vries, A. M. van den Berg, O. Scholten, and K. Werner, "The lateral distribution function of coherent radio emission from extensive air showers: Determining the chemical composition of cosmic rays," *Astroparticle Physics*, vol. 34, pp. 267–273, 2010.

[88] S. Thoudam, S. Buitink, A. Corstanje, J. E. Enriquez, H. Falcke, W. Frieswijk, J. R. Hörandel, A. Horneffer, M. Krause, A. Nelles, P. Schellart, O. Scholten, S. ter Veen, and M. van den Akker, "LORA: A scintillator array for LOFAR to measure extensive air showers," *Nuclear Instruments and Methods in Physics Research A*, vol. 767, pp. 339–346, 2014.

[89] A. V. Gurevich, K. P. Zybin, and R. A. Roussel-Dupre, "Lightning initiation by simultaneous effect of runaway breakdown and cosmic ray showers," *Physics Letters A*, vol. 254, pp. 79–87, 1999.

[90] S. Buitink *et al.*, "A large light-mass component of cosmic rays at $10^{17} - 10^{17.5}$ eV from radio observations," *Nature*, vol. 531, pp. 70–73, 2016.

[91] T. N. G. Trinh *et al.*, "Influence of atmospheric electric fields on the radio emission from extensive air showers," *Physical Review D*, vol. 93, p. 023003, 2016.

[92] G. J. Byrne, A. A. Few, and M. E. Weber, "Altitude, thickness and charge concentration of charged regions of four thunderstorms during trip 1981 based upon in situ balloon electric field measurements," *Geophysical Research Letters*, vol. 10, pp. 39–42, 1983.

[93] M. Stolzenburg, T. C. Marshall, and P. R. Krehbiel, "Duration and extent of large electric fields in a thunderstorm anvil cloud after the last lightning," *Journal of Geophysical Research: Atmospheres*, vol. 115, 2010. D19202.

[94] J. J. Jones *et al.*, "Electric field measurements with an airplane: Problems caused by emitted charge," *Journal of Geophysical Research: Atmospheres*, vol. 98, pp. 5235–5244, 1993.

[95] T. N. G. Trinh *et al.*, "Thunderstorm electric fields probed by extensive air showers through their polarized radio emission," *Physical Review D*, vol. 95, p. 083004, 2017.

[96] S. Agostinelli *et al.*, "GEANT4—a simulation toolkit," *Nuclear Instruments and Methods in Physics Research Section A: Accelerators, Spectrometers, Detectors and Associated Equipment*, vol. 506, pp. 250 – 303, 2003.

[97] "Global data assimilation system." https://www.ready.noaa.gov/gdas1.php.

[98] W. D. Rust and D. R. MacGorman, "Possibly inverted-polarity electrical structures in thunderstorms during STEPS," *Geophysical Research Letters*, vol. 29, pp. 12–1–12–3, 2002.

[99] "KNMI lightning discharge data." https://www.knmi.nl/nederland-nu/klimatologie/geografische-overzichten/onweer.

[100] R. Colalillo, "Peculiar lightning-related events observed by the surface detector of the Pierre Auger Observatory," in *The Pierre Auger Observatory: Contributions to the 35th International Cosmic Ray Conference (ICRC 2017)*, pp. 138–145, 2017.

[101] S. Thoudam, *Propagation of cosmic rays in the galaxy and their measurements at very high energies with LORA*. PhD Thesis, Radboud University Nijmegen, The Netherlands, 2012.

[102] "Wikipedia about the Netherlands." https://en.wikipedia.org/wiki/Netherlands.

[103] E. P. Krider, “Thunderstorm.” https://www.britannica.com/science/thunderstorm, 2016.

[104] J. Lapierre. personal communication.